UC San Diego
UC San Diego Electronic Theses and Dissertations

Title
Investigation of the Mechanical Behavior of WE43 Magnesium Alloy Modified via Multi Directional Forging

Permalink
https://escholarship.org/uc/item/04p8962s

Author
De Souza, Camila Rita

Publication Date
2017

Peer reviewed|Thesis/dissertation

eScholarship.org Powered by the California Digital Library
University of California

UNIVERSITY OF CALIFORNIA, SAN DIEGO

Investigation of the Mechanical Behavior of WE43 Magnesium Alloy Modified via Multi Directional Forging

A thesis submitted in partial satisfaction
of the requirements for the degree Master of Science

in

Materials Science and Engineering

by

Camila Rita de Souza

Committee in charge:

Marc André Meyers, Chair
Javier Garay
Vlado Lubarda

2017

The thesis of Camila Rita de Souza is approved, and it is acceptable in quality and form for publication on microfilm and electronically:

Chair

DEDICATION

To Mamãe, Iá, Titia Madalena and Danila, my family

To Alayde, my emotion

To Marc, my brother

To the memory of Didi, my favorite painter

To Luca, my love

To Máfia, the best classmates of the world

To Elvira, my person

To the memory of Saint Rita of Cascia, my lawyer

To everyone in Brazil and US, who has sent me prayers, love, and positive vibes.

EPIGRAPH

So that we may boldly say, The Lord is my helper, and I will not fear what man shall do unto me.

Hebrews, chapter 13

Know all the theories, master all the techniques, but as you touch a human soul be just another human soul.

Carl Gustav Jung

Sometimes we have to do a big mistake to figure out how to make things right. Mistakes are painful but they’re the only way to find out who we really are.

Shonda Rhimes

TABLE OF CONTENTS

LIST OF FIGURES

LIST OF TABLES

LIST OF ABBREVIATIONS AND SYMBOLS

Å	Angstrom
AMS	Aerospace Material Specification
APF	Atomic Packing Factor
ASTM	American Society for Testing Materials
BCC	Body Centered Cubic
c/a	Ideal Axial Ratio
$CaCO_3 \cdot Mg\ (CO)_3$	Dolomite
d	Diameter
ECAP	Equal Channel Angular Pressing
EDM	Electrical Discharge Machine
EDX	Energy Dispersive X-Ray microanalysis
Eq	Equation
FCC	Face Centered Cubic
GPa	Giga Pascal
HCP	Hexagonal Close-Packed
HgO	Mercuric Oxide
HV	Hardness Vickers
m	Meter
MDF	Multi Directional Forging
Mg	Magnesium
$MgCl_2 \cdot KCl \cdot 6H_2O$	Carnalite

MgO	Magnesia
$MgSO_4$	magnesium Sulphate
min	Minute
mm	Millimeter
MPa	Mega Pascal
Nd	Neodymium
nm	Nanometer
OM	Optical Microscope
P63/mmc	magnesium Space Group
Poisson ratio	Poisson Ratio
s	Second
SEM	Scanning Electron Microscope
SPD	Severe Plastic Deformation
Sr	Strontium
UCSD	University of California, San Diego
UNS	Unified Numbering System
XRD	X-Ray Diffraction Pattern
Y	Yttrium
Z	Atomic Number
Zr	Zirconium
ε	Strain
$\dot{\varepsilon}$	Strain Rate
μm	Micrometer

π	Pi
σ_y	Yield Stress
$\Sigma\varepsilon$	Cumulative Strain

ACKNOWLEDGEMENTS

This research was funded by the UC San Diego Materials Science and Engineering Program Scholarship of the 2015/2016 year, Grant 09-LR-06-118456-MEYM. Experiments were performed at Central South University in Hunan Province – China. We acknowledge the use of the School of Materials Science Laboratories and Mechanical Testing Facility, under the supervision of Prof. Bingfeng Wang (Central South University), he went above and beyond the job description to help make this research possible. The material studied was provided by Prof. Dexue Liu (Lanzhou University of Technology), who gave all the assistance regarding the background and manufacturing of the alloy. A warm thank you to Xiao Xia, who gave her best to be an amazing lab mate, providing all the technical support and friendship in China. We also acknowledge the help from Zezhou Li, Tung Nguyen, Lanyi, Senhat, Haocheng, Dr. Yang, and Dr. Graeve, for overall assistance and hard work to make this project happen. I thank Dr. Ebonee Willians (Gordon Engineering Leadership Center – Jacobs School of Engineering, UCSD) for employing me for two quarters (Fall 2016 and Winter 2017), and for providing important funding.

VITA AND PUBLICATIONS

2017	Master of Science, Materials Science and Engineering University of California, San Diego, San Diego, CA – United States
2015	Bachelor of Science, Metallurgical Engineering Minas Gerais State University, Joao Monlevade, Minas Gerais – Brazil
2015-2017	Research Assistant, Mechanical and Aerospace Engineering Department University of California, San Diego, San Diego, CA – United States
2014-2015	Instructor of Mechanics, Technical School CEBRACTEC, Joao Monlevade, Minas Gerais - Brazil
2013-2014	Research Assistant, Metallurgical Engineering Department Minas Gerais State University, Joao Monlevade, Minas Gerais – Brazil
2014	Mechanical Maintenance Trainee ArcelorMittal Steel Company
2013	Mechanical Maintenance Intern ArcelorMittal Steel Company

"Study of the Impact Strength of API 5L X70-Steel Welded Joints Made by the Manual Arc Process using Coated Basic Electrodes." Brazilian Society of Metallurgy (2015) Proceedings for the Conference on ABM week, Rio de Janeiro, RJ, BRA, 16-21 August 2015.

"Determination of the Impact Strength of the Coarse Grain Region of the Heat Affected Zone of API5L X80 Steel Welded in High Energy Condition." Brazilian Society of Welding (2014) Proceedings for the Conference on Consolda, Sao Paulo, SP, BRA, 20-24 October 2014.

ABSTRACT OF THE THESIS

Investigation of the Mechanical Behavior of WE43 Magnesium Alloy
Modified via Multi Directional Forging

by

Camila Rita de Souza

Master of Science in Materials Science and Engineering

University of California, San Diego, 2017

Professor Marc André Meyers, Chair

Mechanical processing improves the mechanical behavior of modern materials, thus increasing their strength, toughness, and other physical properties. The main objective of this research is to characterize structurally the magnesium alloy and analyze the formation of bulk ultrafine grains produced by two main techniques which promote the

change in grain size and consequently the increase of the mechanical strength. Multi Directional Forging is a compression procedure applied to the material in all three directions, maintaining the dimensional ratio and increasing the strain produced until the cumulative strain be greater than 2.0. As magnesium alloy WE43 has good properties at higher temperatures; the cumulative plastic strain obtained was higher than 2.0. To complement the study of the strength increase via plastic deformation, Equal Channel Angular Processing was applied. The required stress to push the material through the die at 550 $^{\circ}$C was 867 MPa. The results show a moderate decrease in grain size from 18 µm to 14 µm in ECAP and 12 µm in Multi Directional Forging. This decrease in grain size results in an increase in the hardness. In view of the brittleness of the magnesium alloy it was not possible to increase the plastic strain as expected in Multi Directional Forging per pass; the samples fractured if the stress was increased beyond 230 MPa. The yield stress at 1.6 x 10^{-2} s^{-1} increased from 87 MPa for the initial condition, to 115 MPa for the specimens subjected to a strained. In dynamic compression test, experiments were conducted at a strain rate of $2.5x10^{3}$ s^{-1} and the yield stress increased to 246 MPa.

CHAPTER 1 Background

1.1 Introduction

Magnesium is a chemical element with atomic number (Z) 12, abbreviated Mg. Joseph Black recognized it as an element in 1755, but Sir Humphry isolated this metal almost 200 years previously. In 1808, when Davy was working on an electrolyzed mixture of magnesium oxide (magnesia, MgO) and mercuric oxide (HgO), he named magnesium first magnium. It was first manipulated in 1618 by a farmer in England named Henry Wicker who wanted to give his cows better water. The cows refused to drink the water because it had a bitter taste, due to the presence of magnesium sulphate, $MgSO_4$. The commercial production of magnesium started in 1852 by Robert Bunsen, who constructed a small place which was called "The Aluminum and magnesium Fabrik" in Germany. Bunsen designed a new site for dehydration and electrolysis of molten carnalite. Magnesium is named after Magnesia, in Thessaly/Greece, where a high amount of magnesium ore is present [2].

Magnesium is the eight most abundant elements in the world and an amount of 2.1% of magnesium is found in the Earth's crust [3]. magnesium is not formed naturally unless combined in large deposits of minerals, most commonly in dolomite ($CaCO_3 \cdot Mg(CO)_3$), carnalite ($MgCl_2 \cdot KCl \cdot 6H_2O$) and magnesium Sulphate ($MgSO_4$) [4].

In 1920, it magnesium manufacturing was practically non-existent, in 2000, it approached 100.000 tons per year, Figure 1.1 [1]. By then, China produces approximately 80% of the world magnesium market, followed by United States, Russia, Israel, Kazakhstan, Brazil, Ukraine, and Serbia [5].

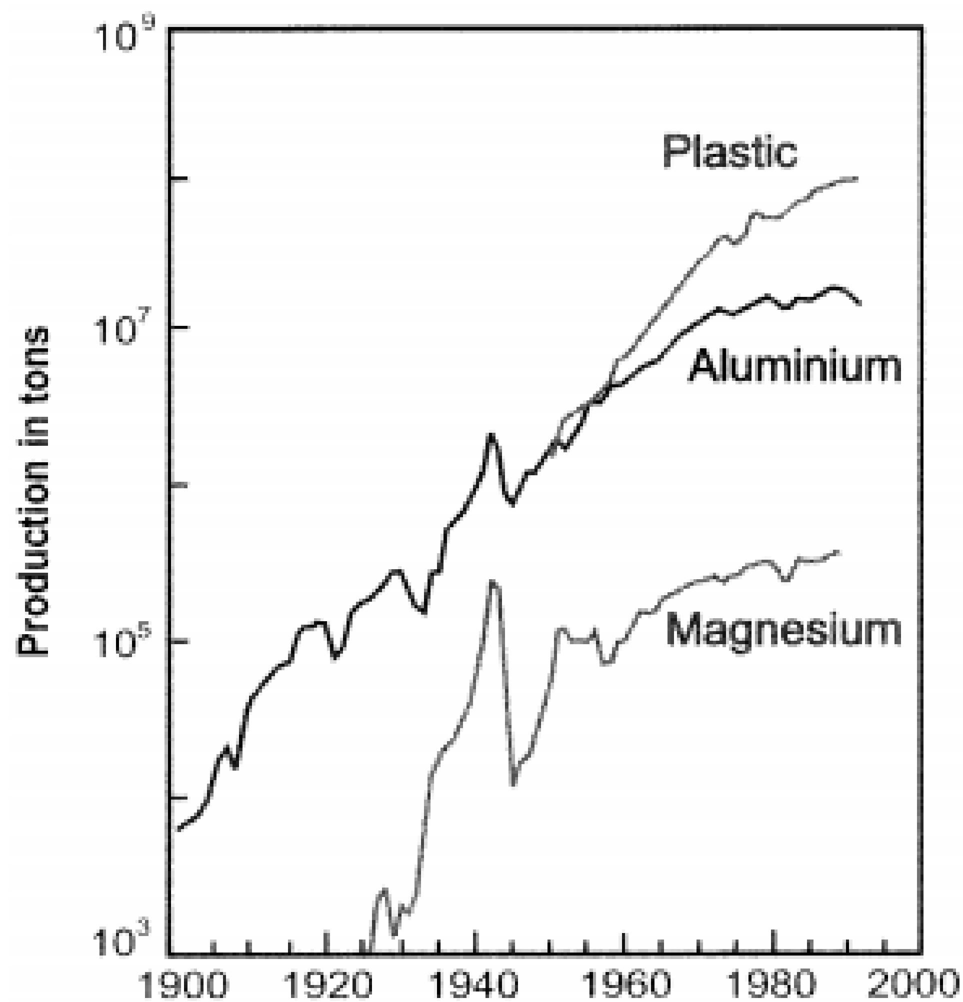

Figure 1.1 Evolution of magnesium production in the 20th century [1]

1.2 Magnesium and Its Alloys

Magnesium, when found in nature combined with other elements, has different colors in a magnesite form, Figure 1.2 (a). Magnesium cannot be found in nature, because it binds with other elements [6], and then it will appear on each mineral with a different color. Magnesium only arises naturally in combination with other chemical elements, where it has a 2^+ oxidation state. [7] The pure element can be obtained artificially, and it shows a characteristic brilliant- white light as illustrated in Figure 1.2(b)

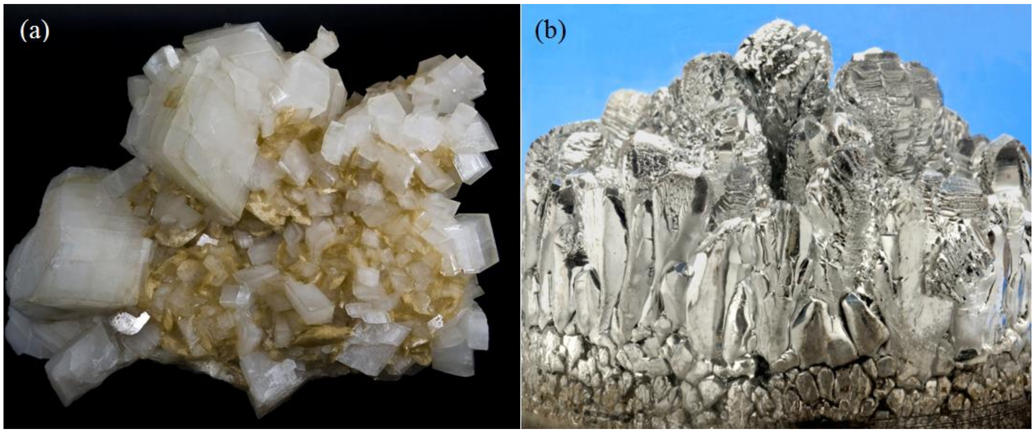

Figure 1.2 (a) Dolomite $CaMg(CO_3)_2$ (white) with magnesite (yellowish) from Spain [8] (b) Pure artificial magnesium [9]

In its polished form, Figure 1.3, magnesium has a gray silvery-white hue, low density, and when exposed to the air forms a thin oxide layer [10]. This material is among the lightest structural metals, has good heat conductivity, good electro-magnetic protection, and it is very strong metal. Magnesium is an alkali earth metal and, when this element burns, creates a white light [11]. By adding water to a magnesium fire, it is possible to produce hydrogen gas [12].

Figure 1.3 Magnesium has a gray silvery-white hue [10].

Currently, the most common magnesium alloys are produced by conventional casting methods where the following elements are strongly present: aluminum, cerium, zinc, silver, thorium, yttrium, zinc, and zirconium [13]. In order to classify magnesium alloys, the American Society for Testing Materials (ASTM) has established a method for defining the alloys. This method dictates that the first two letters indicate the most abundant alloy elements, given in Table 1.1. An example of this correlation is the alloy in study, which is described in Figure 1.4.

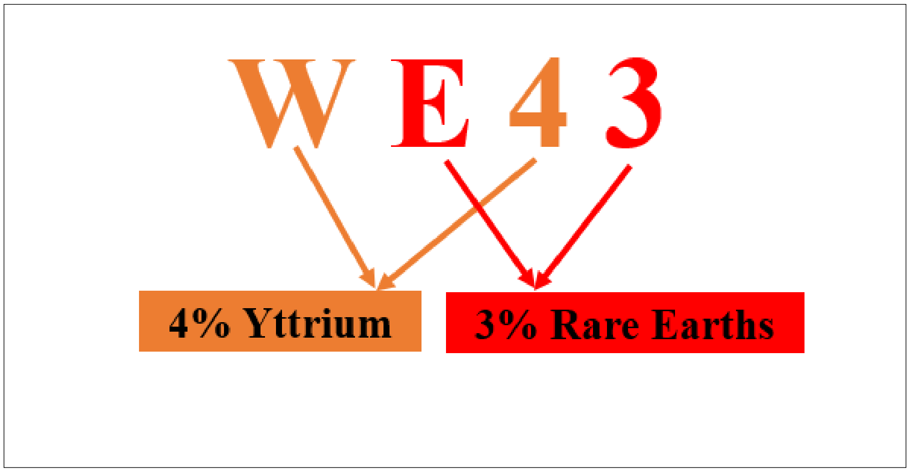

Figure 1.4 Nomenclature designation of magnesium alloy WE43 by ASTM

Table 1.1 ASTM code for designation of magnesium alloys [14]

Code Letter	Alloying Element
A	Aluminum
B	Bismuth
C	Copper
D	Cadmium
E	Rare Earths
F	Iron

Table 1.1 ASTM code for designation of magnesium alloys [14], Continued

Code Letter	**Alloying Element**
G	magnesium
H	Thorium
K	Zirconium
L	Lithium
M	Manganese
N	Nickel
P	Lead
Q	Silver
R	Chromium
S	Silicon
T	Tin
W	Yttrium
Y	Antimony
Z	Zinc

When magnesium alloys are alloyed with rare earth elements, the strength is increased, especially in high temperatures. Also, zirconium can improve exponentially the corrosion resistance [15]. The principal fabrication method of magnesium alloys is conventional casting, Figure 1.5, where the die casting is used repeatedly, but the initial cost can be expensive. Cast magnesium Alloys have manufacturing advantages [16]:

- High productivity;
- High precision;

- High quality surface;
- Fine cast structure;
- Thin wall and complex structure possible;
- Can use steel ingots;
- Lower heat content;
- Good machinability;
- High fluidity of melt.

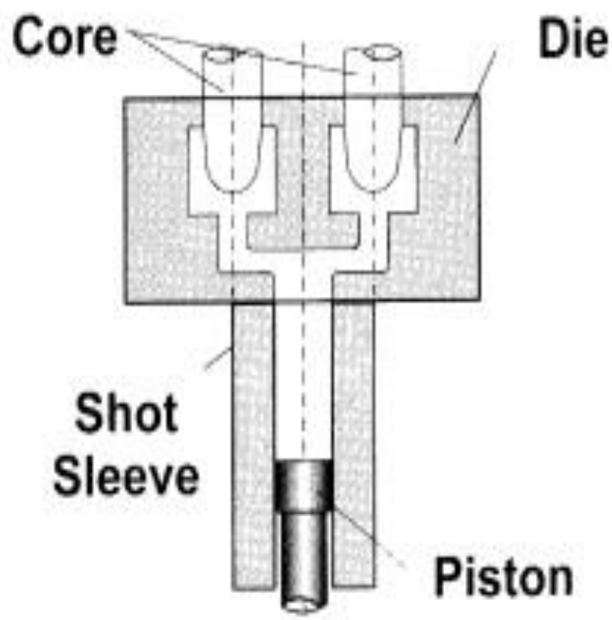

Figure 1.5 Sketch of indirect squeeze casting [1]

A variety of magnesium alloys and their characteristics are described in Table 1.2

Table 1.2 Adapted magnesium alloys and their characteristics [17]

Magnesium Alloy	Characteristics
AE42	Good creep properties to 150ºC
AM20	Good ductility and impact strength

Table 1.2 Adapted magnesium alloys and their characteristics [17], Continued

Magnesium Alloy	**Characteristics**
AM50	High-pressure die castings
AS21	Good creep properties to 150ºC
AS41	Good creep properties to 150ºC
AZ31	Medium-strength alloy, weldable, good formability
AZ61	High-strength alloy, weldable
AZ63	Good room temperature strength and ductility
AZ80	High-strength alloy
AZ81	Tough, leak tight castings with 0.0015 Be, used for pressure die-casting
AZ91	General-purpose alloy used for sand and die castings
EZ33	Good castability, pressure-tight, weldable, creep resistant to 250ºC
HK31	Sand castings, good castability, weldable, creep resistant to 350ºC
HM21	High creep resistance to 350ºC, short time exposure to 425ºC, weldable
HZ32	Sand castings, good castability, weldable, creep resistant to 350ºC
LA141	Ultra-light weight
M1	Low-to medium- strength alloy, weldable, corrosion resistant
QE22	Pressure tight and weldable, high proof stress to 250ºC
QH21	Pressure-tight, weldable, good creep resistance and proof stress to 300ºC
WE43	Good corrosion resistance, weldable
WE54	High strength at room and elevated temperatures
ZC63	Pressure-tight castings, good elevated temperature strength, weldable

Table 1.2 Adapted magnesium alloys and their characteristics [17], Continued

Magnesium Alloy	Characteristics
ZE41	Sand castings, good room temperature strength, improved cast ability
ZK30	High-strength alloys
ZK51	Sand castings, good room temperature strength and ductility
ZK60	Good formability
ZK61	Sand castings, good room temperature strength and ductility
ZM21	Medium-strength alloy, good formability, good damping capacity
ZMC711	High-strength alloy

1.3 Properties of magnesium

Magnesium has [18]:

- Hexagonal Close-Packed (HCP) crystal structure;
- Lattice parameters: a_1=a_2= 0.312 nm and c= 0.512nm;
- c/a = 1.632;
- $\alpha = \beta = 90°$ and $\gamma = 120°$;
- Its space group is P63/mmc (No. 194);
- Coordination number = 12.

Magnesium has a different staking sequence (“ABAB…”) from Face Centered Cubic (FCC) metals (“ABCABC…”) [19]. Figure 1.6 shows a schematic Hexagonal Close-Packed (HPT) structure and how the sequence of layers is distributed.

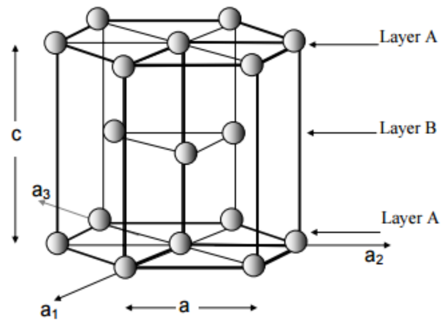

Figure 1.6 Hexagonal Close-Packed crystal structure [18]

The Atomic Packing Factor (APF), the fraction of volume in a crystal structure which is occupied by atoms, for HCP is 0.74. Thus, a single crystal of magnesium has 74% of the lattice completed by atoms. The APF for magnesium is shown below.

APF is the ratio of the total volume of spheres (V_s) to the unit cell volume (V_c). Then:

$$V_s = 6\left(\frac{4\pi R^3}{3}\right) = 8\pi R^3 \tag{1.1}$$

The volume of the unit cell is the base area times the cell height. Figure 1.7 (a) and (b) shows the equilateral triangle to calculate the area:

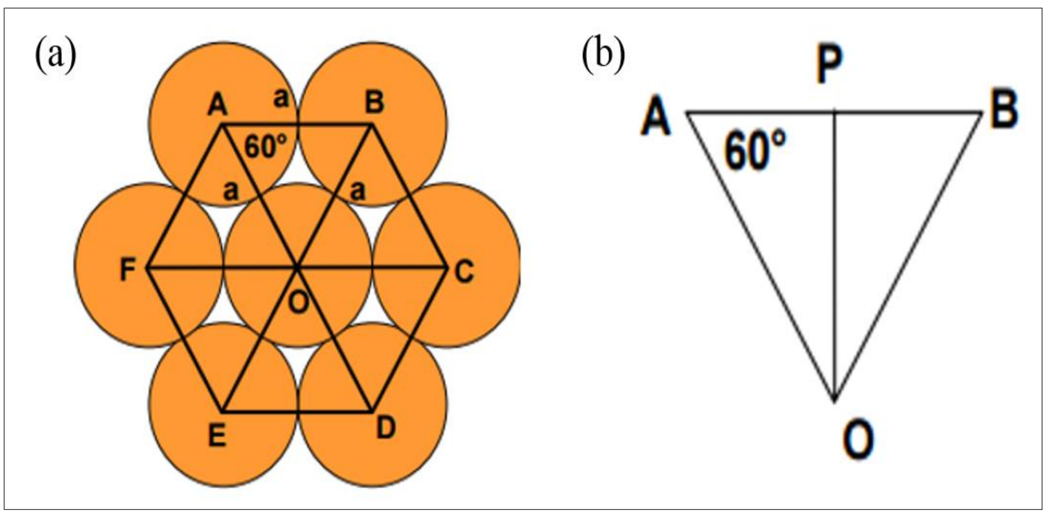

Figure 1.7 (a) The base area of HCP crystal structure (b) Triangle OAB [20]

Area of equilateral triangle is:

$OAB = 0.5 \times AB \times OP$

$A = ½ \times AB \times AO \sin 60°$

$A = ½ \times a \times a \sin 60°$

$A = \frac{\sqrt{3}}{4} a^2$

The area of the base plane is

$$6 \times \frac{\sqrt{3}}{4} a^2 = \frac{3\sqrt{3}}{2} a^2 \quad (1.2)$$

From the basal plane, Figure 1.6 (a):

$$a = 2R \quad (1.3)$$

Then, the base area is:

$$6R^2\sqrt{3} \quad (1.4)$$

The relation between the unit cell height and the basal plane length is:

$c/a = 1.63$

$c = 1.63a$

From Equation (1.3) combined with the c/a ratio:

$c = 3.26\ R$

Then, the unit cell volume is:

$V_c = 3.26\ R \times 10.392\ R^2$

$$V_c = 33.878\ R^3 \quad (1.5)$$

Thus,

$$APF = \frac{V_S}{V_c}$$

(1.6)

$APF = \frac{8\pi R^3}{33.878R^3}$

Finally:

APF = 0.74.

Magnesium is found in over 60 minerals, but dolomite, magnesite, brucite, carnalite, and olivine have commercial significance. Magnesium and its minerals are formed from seawater [21]. Table 1.3 displays the physical properties of magnesium.

Table 1.3 General properties of magnesium [21-24]

General Properties	
Name, Symbol, Number	magnesium, Mg, 12
Element Category	Alkaline Earth Metal
Group, Period, Block	2, 3, s
Standard Atomic Weight	24.304
Electron Configuration	$1s^2\ 2s^2 2p^6$
Physical Properties	
Phase	Solid
Density	1.738g/cm^3
Melting Point	650 °C
Boiling Point	1091°C
Heat of Fusion	8.48 KJ/mol
Heat of Vaporization	128 KJ/mol
Specific Heat Capacity	1.02 J/g °C
Atomic Radius	1.6 Å

Table 1.3 General properties of magnesium [21.22.23.24], Continued

Covalent Radius	1.30 Å
Miscellanea	
Crystal Structure	Hexagonal Close Packed
Electrical Resistivity	43.9 nΩ·m
Thermal Conductivity	156 W(m·K)
Thermal Expansion	24.8 µ/(m·K)
Speed of Sound	4940 m/s
Young's Modulus	42 GPa
Shear Modulus	17 MPa
Bulk Modulus	45 GPa
Poisson Ratio	0.290
Yield Stress	75-200 MPa
Mohs Hardness	1-2.5
Vicker's Hardness	44-260 MPa

Currently, magnesium is used in experiments as an ideal HCP metal, and in this research, the deformation procedures were performed on the material under its favorable conditions of weathering high temperature and pressure. Table 1.4 recaps the basic mechanical properties of common metals used in experiments and research.

Table 1.4 Mechanical Properties of common metals itemized in the periodic table [25,26]

Metal	Crystal Structure	Young's Modulus (GPa)	Shear Modulus (GPa)	Bulk Modulus (GPa)
Aluminum	FCC	70	26	76
Beryllium	HCP	287	132	130
Bismuth	Rhombohedral	32	12	31
Cadmium	HCP	61	23	50
Chromium	BCC	279	115	160
Cobalt	HCP	209	75	180
Copper	FCC	110-128	48	140
Germanium	Diamond Cubic	103	41	75
Gold	FCC	79	27	180
Iron	BCC, FCC	211	82	170
Lead	FCC	16	5.6	46
magnesium	HCP	42	17	45
Molybdenum	BCC	329	126	230
Nickel	FCC	200	76	180
Niobium	BCC	105	38	170
Platinum	FCC	168	61	310
Plutonium	Monoclinic	96	43	-
Silver	FCC	83	30	100
Tantalum	BCC Tetragonal	186	69	200
Tin	DiamondCubic, Te-tragonal	50	18	58

Table 1.4 Mechanical properties of common metals itemized in the periodic table [25,26], Continued

Metal	Crystal Structure	Young's Modulus (GPa)	Shear Modulus (GPa)	Bulk Modulus (GPa)
Titanium	HCP	116	44	110
Tungsten	BCC	411	161	310
Uranium	Orthorhombic	208	111	100
Vanadium	BCC	128	47	160
Zinc	HCP	108	43	70
Zirconium	HCP	88	33	91

The initial microstructure of pure magnesium shows equiaxed coarse grains. The dimension of the initial grain is about 300 μm [27]. Figure 1.8 shows the comparison between the pure magnesium and AZ80 magnesium alloy microstructures.

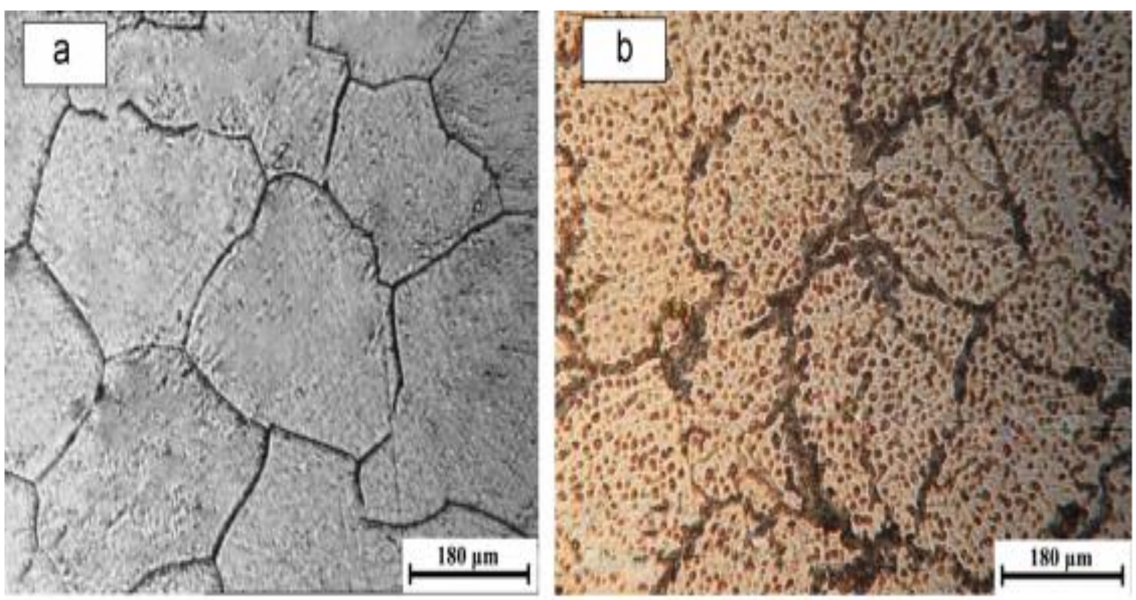

Figure 1.8 (a) Initial Microstructure of pure magnesium and (b) AZ80 magnesium alloy [27]

The coordination number of magnesium depends on the form in which this metal is found [28]:

- Coordination number = 4, Ionic radius Mg^{2+} = 0.71 Å
- Coordination Number = 5, Ionic radius Mg^{2+}= 0.80 Å
- Coordination number = 6, Ionic radius Mg^{2+} = 0.86 Å
- Coordination number = 8, Ionic radius Mg^{2+} = 1.03 Å

The slip systems for magnesium, as in other HCP metals, are limited compared to (BCC) and (FCC) crystal structures. Typically, HCP crystal structures have slip on the tightly packed basal {0001} planes along the $<11\bar{2}0>$ directions [29]. To activate other planes in the crystal structure, various parameters are involved such as c/a ratio. Besides, for plastic deformation to occur, it is necessary that additional twin or slip systems be motivated [30]. Hexagonal closed-packed materials have many types of twinning, though the dominant mechanism that contributes for non-elastic shape deformations on c-direction is on $\{10\bar{1}2\}$. The deformation twining mode of $\{10\bar{1}2\}$ is given by [30]:

$K_1 = \{11\bar{2}0\}$; K_1 is the interface of the twin

$K_2 = \{\bar{1}012\}$; K_2 is the plane rotated by the shear

$\eta_1 = <\bar{1}011>$, direction parallel to the shear

$\eta_2 = <\bar{1}01\bar{1}>$, direction normal to the shear

The angle formed during the rotation is:

$\gamma_0 = 2 \tan \alpha$, where α is the angle that the plane parallel to the direction η_2 makes with the orthogonal plane of the twining shear [31]. Eq 1.7 describes the deformation of the twining mode.

$$S = \{1\bar{2}10\},\ \gamma_0 = \frac{\sqrt{3}}{c/a} - \frac{c/a}{\sqrt{3}} \qquad (1.7)$$

Figure 1.9 shows the tensile twining mode for magnesium. The sketch allows to assume that the shear is specified by:

$\{\gamma_0, m, n\}$

Determined by the pairs:

(K_1, η_2) and (K_2, η_1)

Thus, the amount of shear is:

$$\gamma_0 = 2[(g \cdot n)-1]^{1/2} \qquad (1.8)$$

The direction of the shear is:

$$m = 2\gamma_0^{-1}[n-(g \cdot n)^{-1}g]$$

Where m is the direction of the shear, n is the normal shear direction, and g is the vector in the normal shear direction [32].

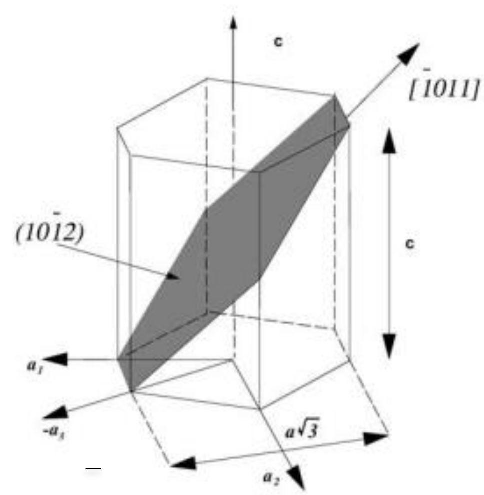

Figure 1.9 The $\{10\bar{1}2\}$ <1011> tensile twinning system for magnesium [32]

Dislocations in materials with hexagonal crystal structure allow the deformation on the basal plane, c = <0001>, where the burgers vector, b = 1/3 <1120>, is responsible for the deformation along the c-axis. Table 1.5 lists some burgers vectors and their properties. The dislocations along the c and a-axes, c + a, have b = <1123> [33]. The basal slip system, (0001) [2-1-10], and the prismatic slip system, (01-10) [2-1-10], do not produce plastic deformation when the Burgers vector is parallel to the c-axis [34]. The deformation and twinning on the non-basal slip, <c + a>, depending on the orientation of the sample, has a stress range of 40 to 450 MPa, Figure 1.10 [35]. The stress produced by the twin dislocations impedes thickening of the previous twins and induces nucleation of recent twins in nearby regions [36]. These slips are different at different sizes and directions, possibly due to the production process.

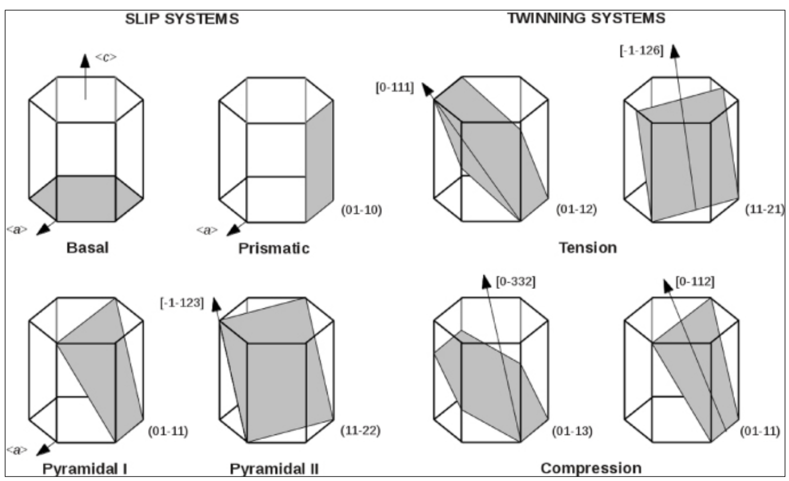

Figure 1.10 Deformations modes in magnesium [36]

The basal and prismatic planes, <a>, as well as the pyramidal plane, <c + a>, constitute the slip system, in which the basal slip is the predominately activated. Schmid law describes the activation of the basal plane, <a>, slip [37,38]:

$$\frac{\sigma_s}{\sigma_n} = \cos\varphi\cos\gamma \qquad (1.9)$$

where σ_s is the shear stress, σ_n is the stress applied to the material, and $cos\varphi cos\gamma$ is the Schmid factor.

Table1.5 Slip systems in HCP materials and their properties [37]

Slip plane	**Slip direction**	**Number of slip system**	
Basal (0001)	a type, <11$\bar{2}$0>	3	2
Prism type I, {10$\bar{1}$0}	a type, <11$\bar{2}$0>	3	2
Prism type II, {10$\bar{1}$0}	a type, <0001>	3	2
Prism type III, {10$\bar{2}$0}	a type, <0001>	3	2
1st order pyramidal type I, {10$\bar{1}$1}	a type, <11$\bar{2}$0>	6	4
2st order pyramidal type I, {10$\bar{2}$2}	c + a, <11$\bar{2}$3>	6	5

1.4 WE43 Magnesium Alloy

The biocompatibility of the metals commonly used in medical applications has increased over the last few years, including magnesium and its alloys [38]. Compared with polymers and modern ceramics, magnesium alloys have shown excellent mechanical compatibility when used for in vivo disease treatment [39]. The mechanical behavior improvement of the alloys has been studied, and procedures that promote fine grain strengthening are recommended. Procedures such as Equal Channel Agular Pressing and High Pressure Torsion are intended to increase the hardness, toughness, strength, and eventually the plastic deformation of the alloys [40].

There are many types of magnesium Alloy that are used in a large number of industrial segments. The WE43 magnesium Alloy is fabricated in accordance with the ASTM standard: ASTM B80 – 15, ASTM B94, ASTM B275, and others denoting mechanical treatment and other parameters [41]. The material is manufactured as well as described on the ASTM documents which designate approximate chemical composition by weight [42]. WE43 magnesium Alloy is the equivalent ASTM B80, with Unified Numbering System (UNS) of M18432, and Aerospace Material Specification (AMS) 4427 standard materials [43]. Table 1.6 shows the nominal composition according to ASTM B80.

Table 1.6 Nominal chemical composition of WE43 magnesium Alloy [44]

ASTM	**UNS**	**Mg**	**Al**	**Cu**	**Fe**	**Y**	**Mn**	**Si**	**Ni**
WE43B	M18432	Remainder	0	0.02	0.010	3.7-4.3	0.03	0	0.005
Rare Earths	**Nd**	**Zr**	**Li**	**Zn**	**Gd**	**Ag**	**Metallic Impurities**		
1.9	2.0-2.5	0.4-1.0	0.2	(a)	0	(a)	0.01		

There are some considerations to make about the production of the alloy:

a) Zinc + Silver does not exceed 0.20% of the nominal weight.

b) Some heavy rare earth materials such as gadolinium, dysprosium, erbium, and ytterbium are sometimes used. If there are other rare earths materials, they are made up of, usually, 80% of yttrium and 20% of the heavy ones [44].

The mechanical characterization of all series of magnesium alloys are also specified as well as the standards. Magnesium alloy properties are very advantageous in terms of lightweight materials [45]. Figure 1.11 compares the weight of some metals that are also used to make industrial alloys.

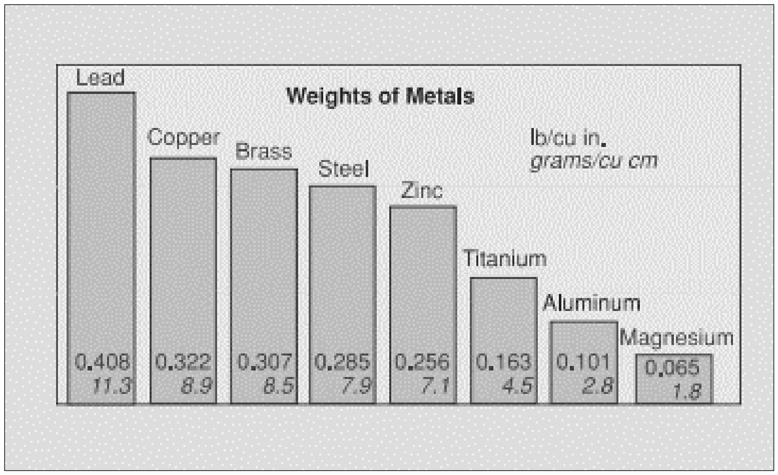

Figure 1.11 Comparison between weight of industrial metals [46]

In terms of casting production, several properties of magnesium alloys such as damping capacity, dimensional stability, and impact and dental resistance provide many advantages over other lightweight metals [46]. Table 1.7 relates typical mechanical properties of main industrial magnesium alloy.

Table 1.7 Mechanical properties of main magnesium alloy [46]

Property	**AZ91**	**AM60**	**AM50**	**AM20**	**AS41**	**AS21**	**AE42**	**WE43**
Ultimate Tensile Strength (MPa)	240	225	210	190	215	175	230	125
Tensile Yield Strength (MPa)	160	130	125	90	140	110	145	90
Compressive Yield Strength (MPa)	160	130	125	90	140	110	145	85
Fracture Elongation (%)	3	8	10	12	6	9	10	2
Elastic Modulus, Tension (GPa)	45	45	45	45	45	45	45	45
Elastic Modulus, Compression (GPa)	17	17	17	17	17	17	17	17

Table 1.7 Mechanical properties of main magnesium alloy [46], Continued

Property	AZ91	AM60	AM50	AM20	AS41	AS21	AE42	WE43
Brineel Hardness	70	65	60	45	60	55	60	60
Impact Strength	6	17	18	18	4	5	5	8

The grain size of WE43 is about 12µm [47] after being extruded. The alloy contains solid solution α-Mg with precipitates of a solid state compound that has metallic bounding phases at the grain boundaries, Figure 1.12.

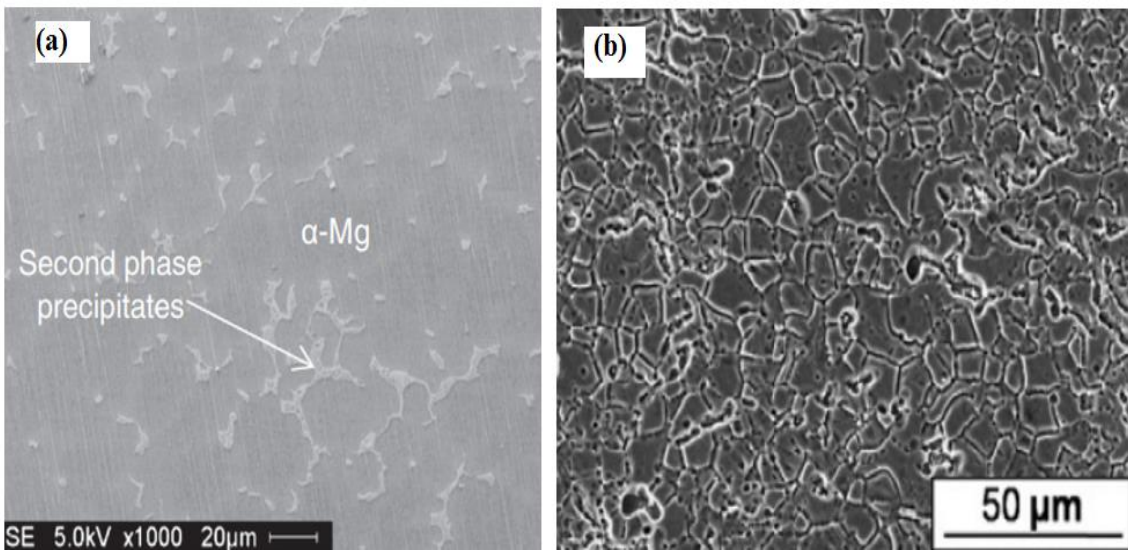

Figure 1.12 (a) SEM image of the WE43 magnesium Alloy showing the presence of second phase [47], (b) SEM image showing the microstructure of the WE43 magnesium alloy after extrusion [48]

The resistance to corrosion of WE43 is much appreciated because it permits the promotion of excellent biocompatibility of the alloy with the human body. The Young's modulus and tensile and compression strength of cortical bone is similar to magnesium and its alloys [49], making orthopedic applications attractive. Usually the corrosion layer in WE43 magnesium alloy starts in regions between the middle and the boundaries of the grain. When zirconium conglomerates with intermetallic constituents, the resistance to corrosion increases [50].

1.5 Applications of WE43 magnesium Alloy

WE43 is one of the high strength casting magnesium alloys that offers excellent mechanical properties both at ambient and elevated and temperature [51]. Figure 1.13 shows how the main mechanical properties of the alloy are developed. This alloy is a great engineering solution where lightweight materials and satisfactory corrosion resistance are required, without compromising performance. Compared with steel, WE43 is 75% lighter, which makes many automobile industry companies choose magnesium alloys over steel [52].

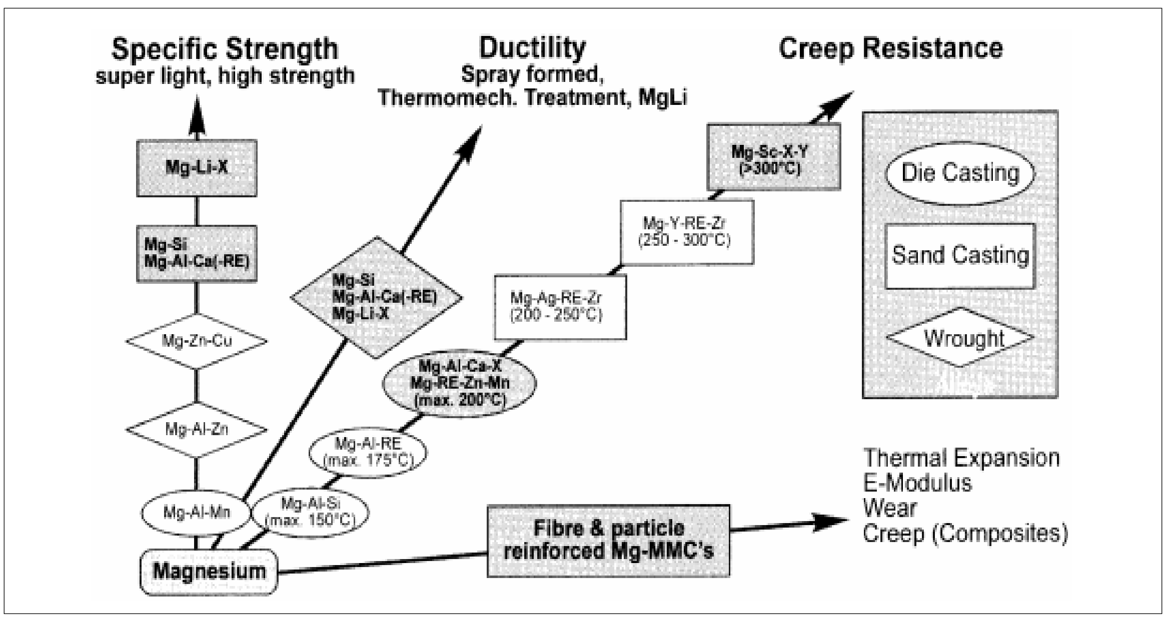

Figure 1.13 Background of alloy development [1]

The aerospace and automotive industry use WE43 magnesium alloy in 8 applications, such as missiles, power transmissions, aircraft engines, helicopter rotor heads, engine casings, racing wheels, gear box casings, among others [53]. In vehicles, the alloy is used for welded constructions, for example doors, dashboard, seat structure, wheels, steering, and oil sump, Figure 1.14.

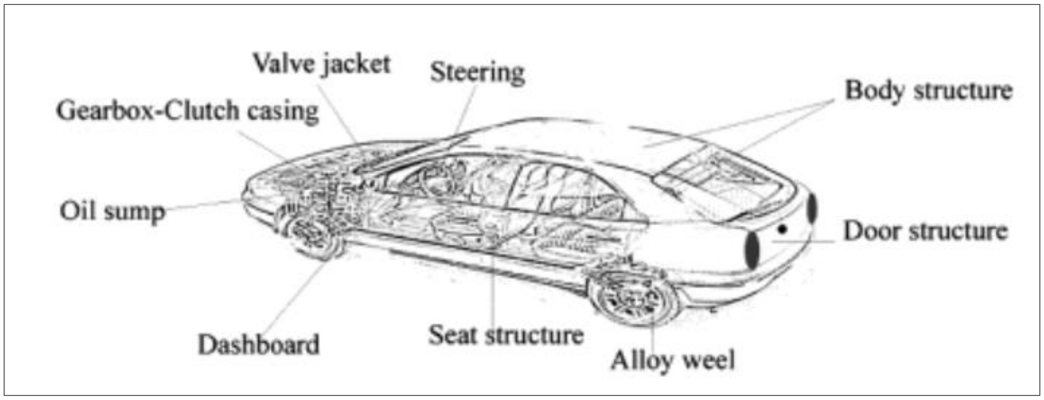

Figure 1.14 Vehicle parts where WE43 magnesium alloy are used [54]

The welding of WE43 magnesium alloys is usually conducted by a laser procedure using helium or argon as inert gas. The penetration of the welding is proportional to the energy of penetration, calculated by the power (P) and the speed of the welding (v). The joint can resist up to 250 MPa of tensile strength, making the structure made by WE43 satisfactory and reliable [54, 55].

Biocompatibility is the key for successful biodegradable implants, making the surgery efficient and reducing to zero the necessity of a new surgery which can lead complications. The dissolution rate of magnesium alloy is an attractive feature for the use of its alloys in humans. The human body has nearly 20g of magnesium. Because of this, the dissolution of the magnesium is not damaging. Once magnesium is dissolved, the hydroxide is simply resorbed, while hydrogen can form bubbles if the rate of generation is greater than the rate at which the second phases can absorb it. The reaction of dissolution of magnesium is given by [56]:

$$Mg + 2H_2O \rightarrow Mg(OH)_2 + H_2$$

Procedures that modifie the mechanical behavior of the alloy can improve the disolution rate, which can be measured in vitro [57]. Figure 1.15 describes the degradation rate of AZ31 magnesium alloy modified by ECAP and Hot Rolling (HR) compared to standard conditions in saline solution [58].

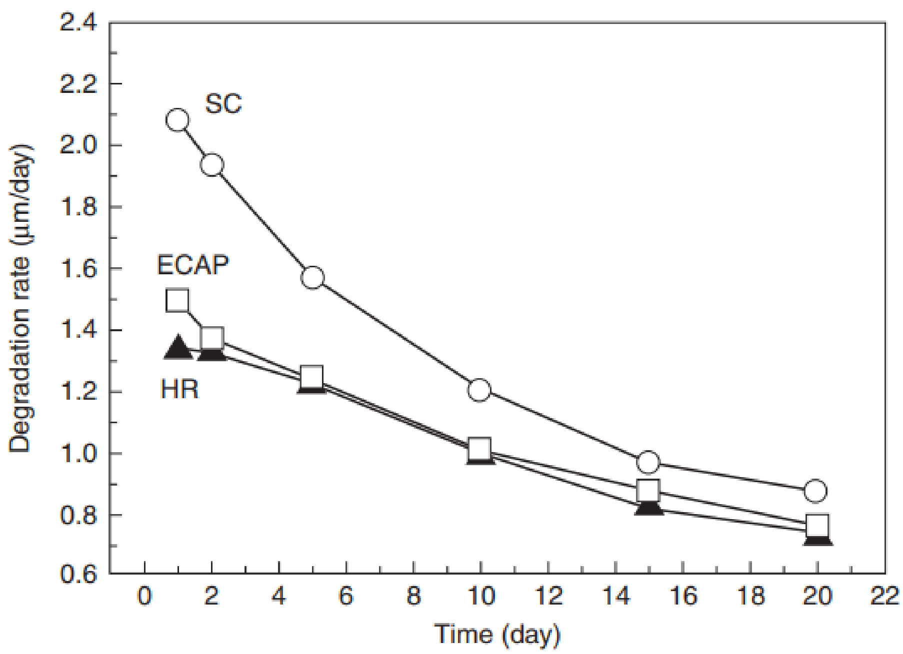

Figure 1.15 Degradation rate and effect of grain size reduction of AZ31 magnesium alloy by ECAP, hot rolling and standard conditions [58]

Ultra-fine grained WE43, obtained by methods of severe plastic deformation, presents better mechanical behavior and elevated corrosion resistance than in its initial state. This condition improves the performance of the material in biological atmosphere [59,60].

Balanced diet is also one of the commons applications of magnesium because it presents itself in many types of food, including grains, vegetables, and fruits [60]. Magnesium helps maintain normal muscle and nerve function, heart rhythm, the immune system, bone structure, normal blood pressure, and sugar levels. Scientists and doctors currently recommend the ingestion of 400 mg of magnesium per day [61-63]. Table 1.8 presents the foods highest in magnesium and its percentage in 100g of food.

Table 1.8 Highest magnesium-containing foods and their quantity of magnesium [64,65]

Food	Quantity (mg)
Raw spinach	79
Kale	72
Pumpkin seeds	534
Mackerel fish	97
Soy beans	86
Brown rice	44
Avocado	29
Yogurt	19
Banana	27
Fig	68
Dark Chocolate	327

1.6 Principal Methods to Produce Severe Plastic Deformation in Mg Alloys

Severe Plastic Deformation (SPD) is a technique involving very large amounts of strain produced by a high stress state and shear [66]. Lately, SPD has been an area of discussion due to its capability of ultrafine-grained materials production [67]. The reorganization of the dislocations given by straining leads to a very substantial grain refinement, to the submicrometer or even nanometer level. Also, SPD methods offer the possibility of refining the grain size to stages expressively smaller than when produced using conventional thermomechanical procedures [67,68]. The most common procedures to use for SPD are Equal Channel Angular Pressing (ECAP) and High-Pressure Torsion (HPT) [69], and Multi Directional Forging (MDF) is also being used to produce fine grains in bulk materials by resources of SPD [70]. Magnesium alloys have many prospective applications because of their low density and excellent machinability. However, as a result of the HCP crystal structure, they generally exhibit only restricted ductility at room temperatures. ECAP is equally effective at decreasing the grain size of pure magnesium and its alloys through recrystallization during pressing. The consequence of the procedure is a significant improvement of strength and ductility [68]. Grain refinement leads to an increase in the strength of the material, which is generally described by the experimental correlation between the yield stress σ_y and the average grain size *d* [71,72], and this is confirmed by the Hall–Petch equation that is derived below [73].

The length of the grain is approximately:

$$L \cong \frac{D}{2} \tag{1.10}$$

Eshelby Equation is used to determine the length of the pileup (*L*) in terms of *n* (number of dislocations in the pileup), *G* (shear modulus), *b* (burgers vector), and τ_A (applied stress).

$$L = \frac{\alpha\, n\, G\, b}{\pi\, \tau_A} \tag{1.11}$$

Combining Equations (1.10) and (1.11):

$$\frac{D}{2} = \frac{\alpha\, n\, G\, b}{\pi\, \tau_A} \tag{1.12}$$

Rearranging Equation (1.12)

$$n = \frac{D\,\pi\,\tau_A}{2\,\alpha\,G\,b}$$

The stress acting on the dislocation is:

$$\tau = n\,\tau_A \tag{1.13}$$

Then, the stress is equal to yield stress, considering the minimal amount of stress to start to move a dislocation:

$$\tau = \sigma_y \tag{1.14}$$

Combining Equation (1.12) after rearrangement and Equation (1.13):

$$\tau = \frac{D\,\pi\alpha\,\tau_A}{2\;G\,b}\,\tau_A$$

$$\left(\frac{D\,\pi\alpha}{2\;G\,b}\right)\sigma_y^2 \geq \tau$$

$$\sigma_y^2\,D\,\pi = 2\,G\,b\,\tau\,\alpha$$

$$\sigma_y^2 = \left(\frac{\pi}{2\,\alpha\,G\,b}\right)^{-1/2}\tau^{-1/2}\;D^{-1/2}\,,$$

which $\left(\frac{\pi}{\alpha\,G\,b}\right)^{-1/2}$ is defined as strengthening coefficient (k).

Finally, the Hall-Petch relation is:

$$\sigma_y = \sigma_0 + \frac{k}{\sqrt{D}} \tag{1.15}$$

The theoretical strengthening coefficient for pure magnesium is k = 0.28 MPa $\sqrt{m}$ [74].

1.6.1 Equal Channel Angular Pressing – ECAP

Equal Channel Angular Pressing (ECAP) is one of the most common processing methods that produces Severe Plastic Deformation (SPD). ECAP was first studied in 1972 and first divulgated by Segal [75]. This technique can be applied in a very large number of materials that may be used in many structural applications. It is performed on a wide range of metals [76]. ECAP may be developed and applied to materials with all types of crystal structure and other materials that are precipitation-hardened and have metal-matrix as a component. A schematic illustration of this procedure is shown in Figure 1.16.

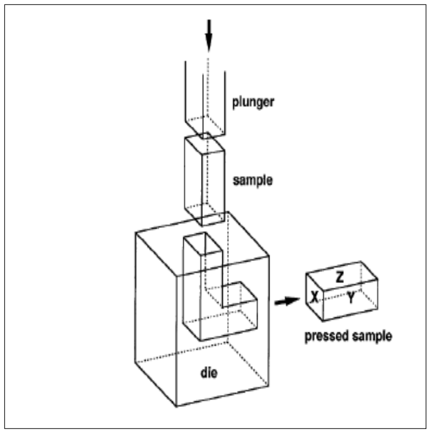

Figure 1.16 Sketch of ECAP procedure showing the typical ECAP die and the sample designated by the transversal planes X, Y and Z [76]

ECAP is performed in a two-piece die, the two pieces having the same cross section from which the specimen will be extruded [77]. The die is schematically shown in Figure 1.17, with the two parts intersecting at an internal angle Φ (60° and 120°) and an out angle Ψ (0°).

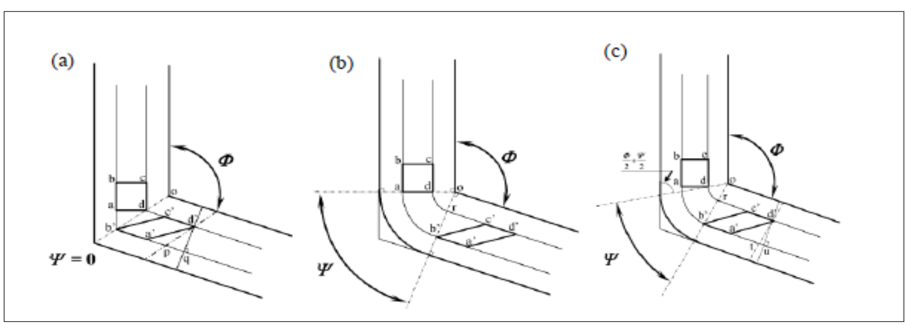

Figure 1.17 Three conditions of Ψ for calculation of the strain after N passes (a) Ψ =

120º, (b) Ψ= π - Φ,and (c) an arbitrary angle Ψ = 120º and Ψ = π - Φ [77]

The strain caused on the sample during this process is proportionally affected by the values of these angles [78]. During ECAP, the cross-section of the samples does not change, but after a determined number of passes, the microstructure is modified depending on the rotation scheme [79].

Usually the schemes are:

a) Route A – the billet does not move between passes,

b) Route B_A – the billet routes in 90° in different directions between passes;

c) Route B_C – the billet routes in 90° in the same direction between passes;

d) Route C – the billet routes in 180° between consecutive passes. [80,81]

Route B_C is the most efficient route because the samples produce grains with approximate size 300 nm [82-84], and thus the microstructure produced is equiaxed. Figure 1.18 shows the different types of routes. Figure 1.19 gives the sketch of slip system.

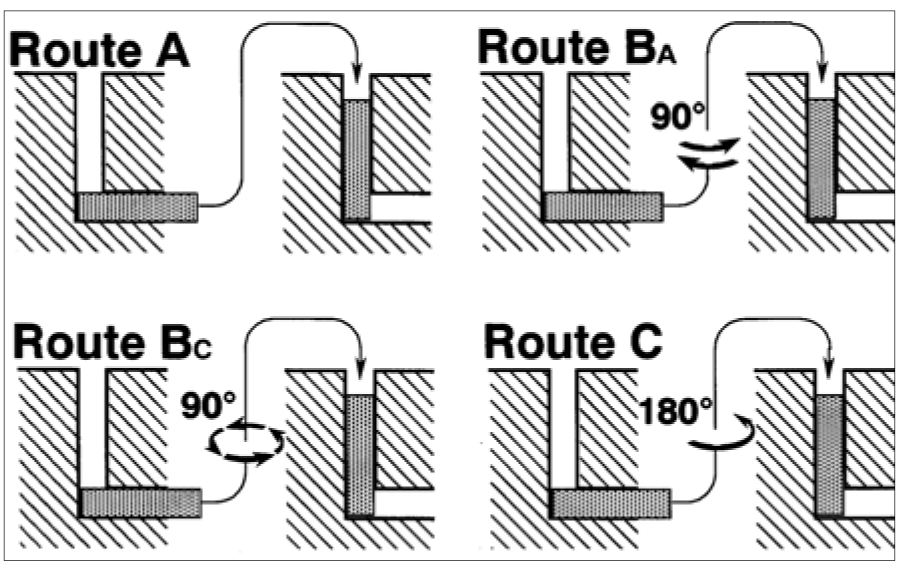

Figure 1.18 Sketch of fundamental processing routes in ECAP [80]

The strain is predictable when considering a well-lubricated specimen for which frictional contribution is neglected. Assuming a square sample labelled a, b, c and d in the entrance of the channel, as Figure 1.17 shows, the shearing strain (γ) is given by the following equations [84,85]:

$$\gamma = 2\cot(\Phi/2) \qquad (1.16)$$

Assuming that Ψ=π-Φ from Figure 1.17 (b):

$$\gamma = \Phi \qquad (1.17)$$

$$\gamma = 2 \cot \left(\frac{\Phi}{2} + \frac{\Psi}{2}\right) + \Psi \operatorname{cosec} \left(\frac{\Phi}{2} + \frac{\Psi}{2}\right) \qquad (1.18)$$

Thus, the equivalent strain after N passes (ε_N) is:

$$\varepsilon_N = \frac{N}{\sqrt{3}}\left[2\cot\left(\frac{\Phi}{2} + \frac{\Psi}{2}\right) + \Psi \operatorname{cosec}\left(\frac{\Phi}{2} + \frac{\Psi}{2}\right)\right] \qquad (1.19)$$

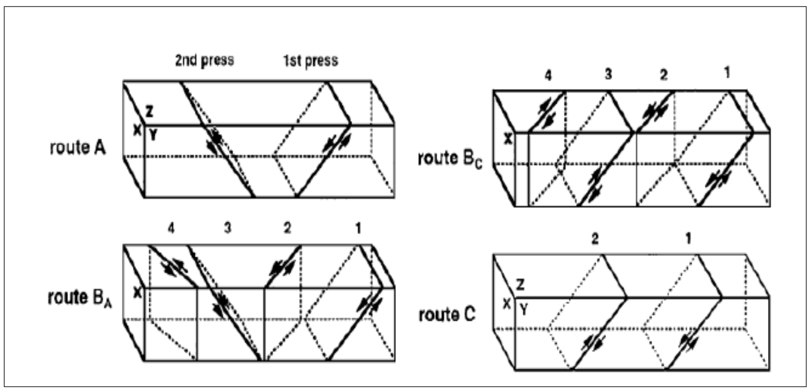

Figure 1.19 Sketch of the slip system of four processing routes for consecutive passes [80]

1.6.2 Multi Directional Forging

Multi Directional Forging (MDF) is one of the various SPD procedures that allows the deformation of the material to modify its mechanical properties [86]. When submitted to MDF procedures, the material is exposed to very high strain without any related changes in the cross sectional dimensions of the specimens. In other words, the deformation occurs in constant ratio [87]. High strain can be transmitted to the sample by persistently pressing the material several times using the same amount of loading [88].

During the MDF procedure, the sample is inserted in the system and pressed downwards to an equivalent strain of 0.2 in each axis, constantly. The equivalent strain is given by Equation 1.20 [89].

$$\epsilon_e = \ln \frac{h_0}{h_f} \qquad (1.20)$$

where h_0 is the initial height of the sample and h_f is the final height.

Figure 1.20 shows, schematically, how the specimens are deformed by Multi Directional Forging.

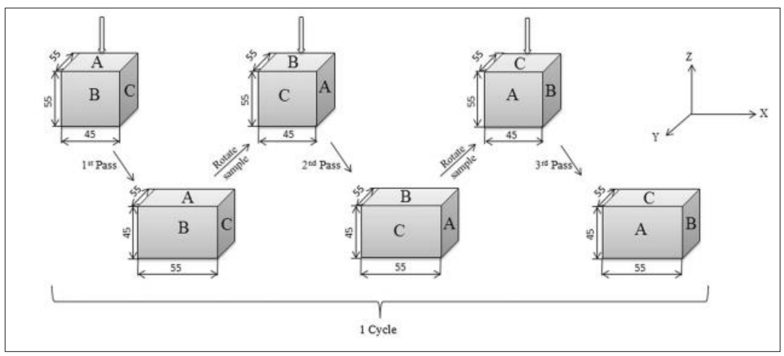

Figure 1.20 Schematic diagram of MDF process along x, y, and z axes [89]

Magnesium and its alloys have been considered as hard plastic materials due to their formability and ductility, which themselves are due to the HCP crystal structure at room temperature. Structural magnesium alloys, lately, have been manufactured by casting route with more frequency than plastic working, such as rolling [90,91]. It is known that:

a) Many slip systems can be operated in addition to the basal slip system during hot deformation, promoting an increase in the plastic workability [92];

b) Fine grains are developed in magnesium and its alloys at low strain during hot working, and the consequence is good improvement of the plastic workability [93].

The cumulative strain ($\Sigma\varepsilon$) is the sum of each strain calculated on each pass. When $\Sigma\varepsilon \geq 2$, MDF processing successfully deforms the magnesium alloy at 423 K, which is below 0.5 T_m [94]. Figure 1.21 shows the true stress-strain curves during MDF with decreasing temperature.

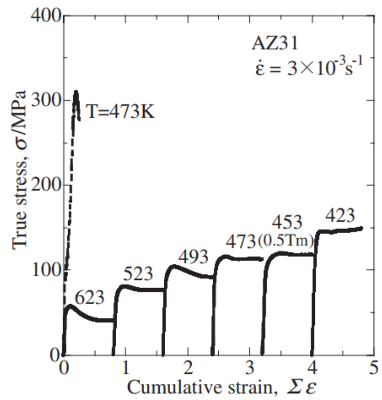

Figure 1.21 True stress-strain curves of AZ31 magnesium alloy [94]

In order to provide data to compare with the literature review presented, Chapter 2 discusses the experimental procedures performed in this study. Figure 1.22 summarizes the scope of the research.

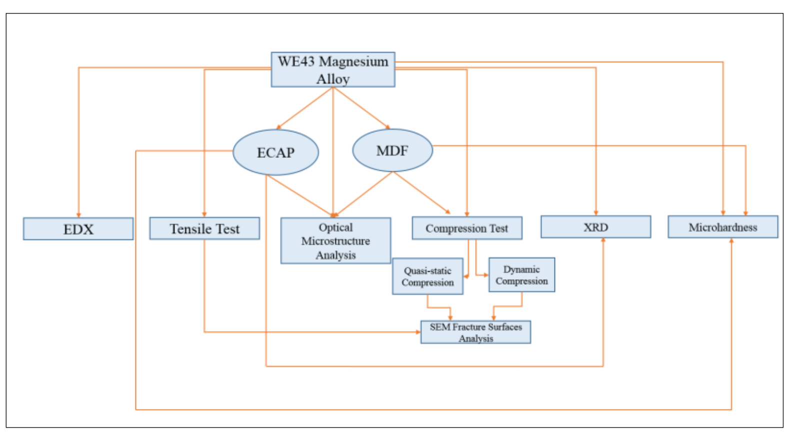

Figure 1.22 Research Scope

Chapter 2 Experimental Procedures

2.1 Fabrication of magnesium Alloy WE43

The material used is an alloy fabricated by Dr. Dexue Liu at the Lanzhou University of Technology, China. The We43 Magnesium Alloy was prepared by vacuum melting and normal casting methods. The chemical compositions are listed in Table 2.1 and 2.2, which were first melted at a temperature of 800 °C and followed by the annealing treatment at 400 °C for 4 hours. Then, the alloy was cast into a die to obtain the cylindrical shape. Two alloys were fabricated with a tiny difference between them. The two can both be called WE43 Magnesium Alloy. However, in one of them, Niobium (Nb) was replaced by Strontium (Sr) because Sr has much better compatibility [48] with biological devices. Table 2.3 shows the commercial alloys used to fabricate the material of this study.

Table 2.1 Chemical composition of the magnesium Alloy WE43 – Mg-Y-Nd [48]

Y	**Nd**	**La(Ce)**	**Zr**	**Mg**
4.2	2.4	0.6	0.5	Balance

Table 2.2 Chemical Composition of the magnesium Alloy WE43 – Mg-Y-Sr [48]

Y	**Sr**	**La(Ce)**	**Zr**	**Mg**
4.2	1.5	0.6	0.5	Balance

Table 2.3 Commercial alloys [48]

Mg-Y	**Mg-Sr**	**Mg-La(Ce)**	**Mg-Zr**	**Mg**
30	20	30	30	99.9

The Meyers group at the University of California has received two pieces of the

X. Liu, one piece of Mg-Y-Nd and one piece of Mg-Y-Sr. Figure 2.1 shows how the piece of magnesium alloy WE43 appeared right after casting and the initial shape of the alloy in this study.

Figure 2.1 Piece of WE43 magnesium alloy produced by melting and casting process.

2.2 Preparation for Equal Channel Angular Pressing and Multi Directional Forging

Multi Directional Forging (MDF) and Equal Channel Angular Pressing (ECAP) were carried out on this magnesium Alloy. The samples for ECAP were cut by EDM, which machines magnesium alloys well and with good surfaces integrity, in dimensions of diameter measured at 6.4 mm and length of 43 mm. Figure 2.2 shows dimensions of the specimen for ECAP and Figure 2.3(b) shows schematically how the specimen cut was made. Before starting the cutting process, a conductivity check was made on the surface of the samples. It was detected that not all the samples exhibited conductivity due to internal fractures and rearrangement of the atoms after SPD.

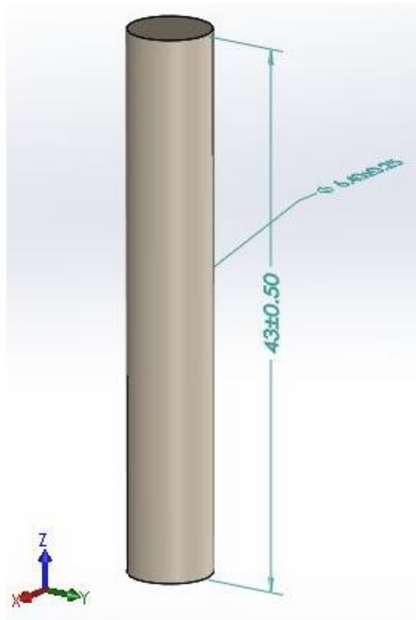

Figure 2.2 Sketch of the ECAP sample

For the Multi Directional Forging (MDF) procedure, the samples were also machined by wire cutting. The shape and dimensions were 20x16x13 mm and are shown in Figure 2.3.

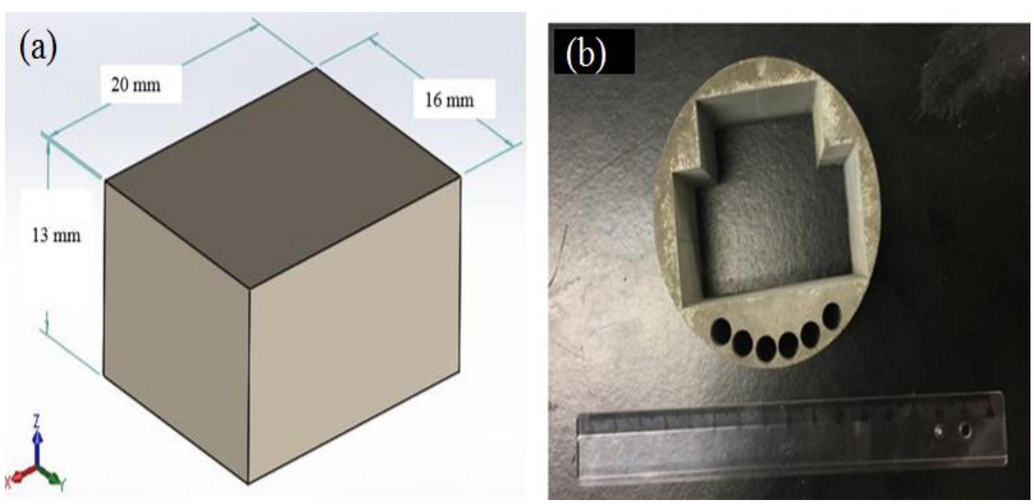

Figure 2.3 (a) Sketch of the MDF sample (b) Withdrawal of the samples

2.3 Equal Channel Angular Pressing Procedure

In order to perform Equal Channel Angular Pressing (ECAP), it is necessary to fabricate grips to fix the mobile part of the die shown in Figure 2.4 (c), while the pressing loading was applied on the die system. ECAP processing was carried out through a die made of nonferrous material. The ECAP die is made of two parts with a 6.7 mm channel and an outer curvature angle φ of 120°. To pressurize the specimen inside the channel and make it go through the die, the bars were fabricated with High Strength Low Alloy (HSLA). Figure 2.4 (a) shows the bars, which were conventional, machined, and received annealing after heat treatment to make it harder. The bars were maintained at a temperature of 450 °C (bellow the transformation range) for 2 hours, followed by cooling in oil at an appropriate rate, in order to produce a desired combination of mechanical properties. The dimensions of the bars are shown in Figure 2.4 (b).

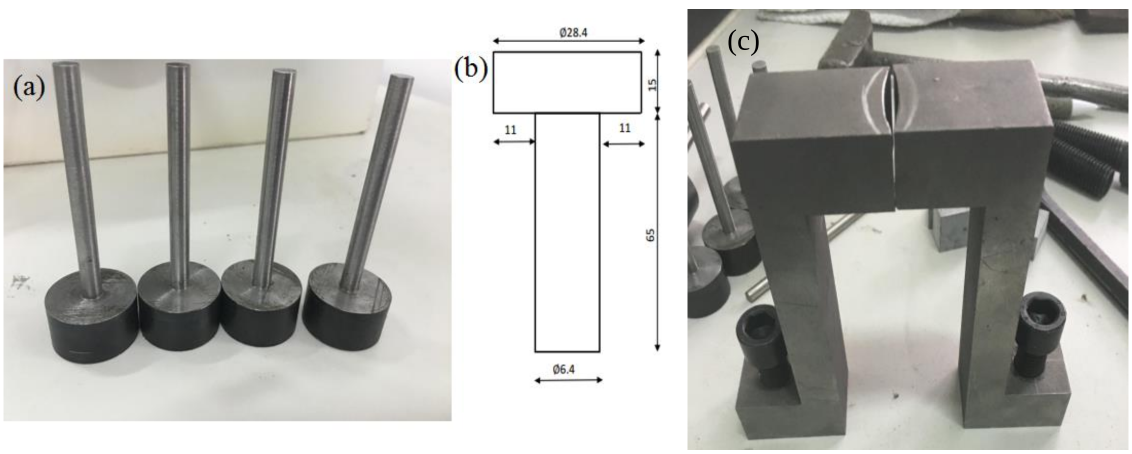

Figure 2.4 (a) Pressure bar (b) Pressure bar with dimensions in mm, and (c) Grips

The Equal Channel Angular Pressing procedure was performed in the ISTRON, machine under compression loading transmitted to the samples in the die by the pressure bars. The samples were heated to 550 °C and maintained for 2 hours before the procedure. During the procedure, the temperature was sustained by a conduction system of heat transfer. Figure 2.5 shows the ECAP processing system.

During the procedure, the maximum value for stress while pressing the sample was 891 MPa where the strain was about 2%. Figure 2.6 shows the behavior of the sample during the procedure. The total time of the compression was about 25 min with speed of 2 mm/min.

Figure 2.5 (a) ECAP system (b) transversal view of the die (c) view from the top of the die

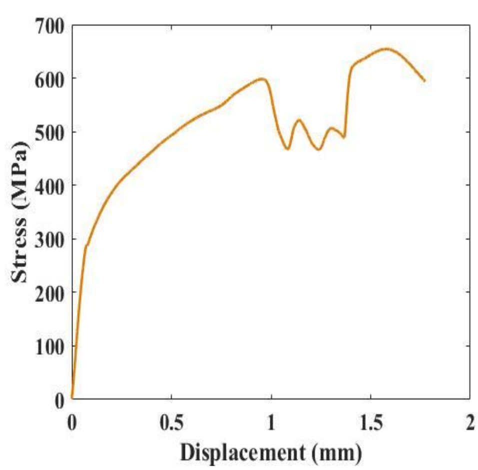

Figure 2.6 Stress-displacement curve for 1st pass during ECAP procedure

2.4 Multi Directional Forging Pocedure

Multi Directional Forging (MDF) was also performed in the same INTRON –type mechanical testing machine with the compression accessories as shown in Figure 2.7. First, one of the MDF samples was compressed until failure was achieved to set the applied strength parameters during the process. The speed of the forging process was 2 mm/min, and the forging temperature decreased from 550 °C to room temperature during the test. The samples were submitted to heat treatment (550 °C) and held in a furnace for 10 min before each forging pass. The initial strain rate was 3 x 10^{-3} s^{-1}, and the load was applied until the stress was equal to 230 MPa.

Figure 2.7 The equipment of Multi Directional Forging

The samples were rotated after each axis pressing, then measured, and pressed in the following axis and so on. The total strain undergone by each specimen was obtained by Equation 2.1, where the strain (ε) in one pass is the sum of the strain on the x (ε_x), y (ε_y), and z (ε_z) axes. Figure 2.8 describes how one forging sequence is done.

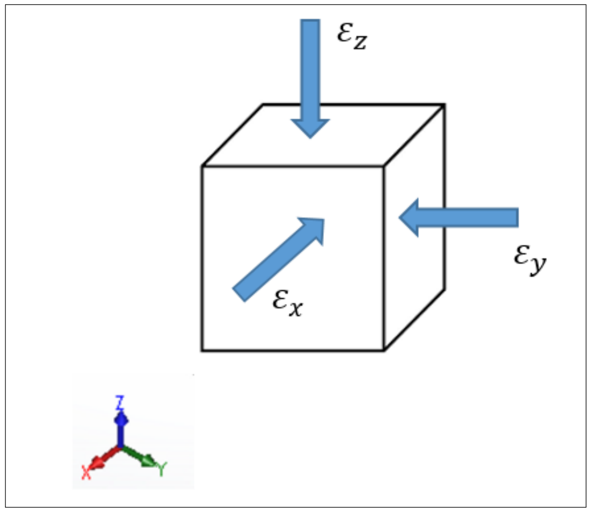

Figure 2.8 Sketch of one forging sequence

The total strain after several passes is:

$$\sum\varepsilon = \sum\varepsilon_x + \sum\varepsilon_y + \sum\varepsilon_z \quad (2.1)$$

where $\sum\varepsilon$ is the cumulative strain reached by the sum of the strains of the total number of passes. The principal specimens obtained by MDF procedure are shown in table 2.4. Appendix A details the calculation of $\sum\varepsilon$.

Table 2.4 Cumulative strain obtained by MDF

Specimen	Number of Passes	$\sum\varepsilon$
01	18	1.82
02	20	2.14
03	10	1.22
04	20	2.77

To evaluate how much strength the sample used in the MDF procedure could support prior to failure, a specimen with the same shape of the ones used in the procedure was compressed. It was observed that the sample maximum stress was about 280 MPa and that yield stress was about 110 MPa, having final strain of approximately 0.2 mm/mm, Figure 2.9.

From this value of stress, it was possible to define how much load could be applied during the MDF procedure with a uniform deformation between each pass.

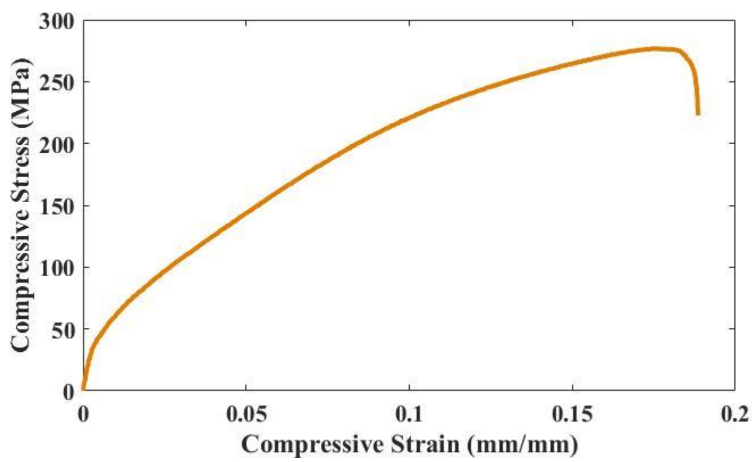

Figure 2.9 Stress-strain curve for the compression test in the initial state sample

Appendix B describes the stress-strain curves during the process. The curves show the approximately the same amount of deformation while the samples are pressed because of the constant stress produced (about 230 MPa) through the test. It occurred due to the same amount of load applied in every pass.

The sample in which the cumulative strain is equal to 1.22 stopped being pressed because it had a crack during the 10^{th} pass on the X axis. The last compression that this sample had was on y axis direction, making the crack, initially visible, to reclose. However, the flaw persisted.

Sample with $\sum\varepsilon$ = 1.82 also stopped being pressed before it reached $\sum\varepsilon$ = 2.0, because it presented a crack while compressed on x direction.

Samples with $\sum\varepsilon$ = 2.14 and $\sum\varepsilon$ = 2.77 reached the cumulative strain established in 18 and 20 passes respectively.

2.5 Tensile Testing of Initial State WE43 Magnesium Alloy

The tensile test was performed on an INSTRON machine, and the sample was conventional machined as shown in Figure 2.10. Figure 2.11 shows how the specimen was gripped to run the test. The diameter of the reduced section was 5 mm, the distance between shoulders was 30 mm, and gage length was 25 mm.

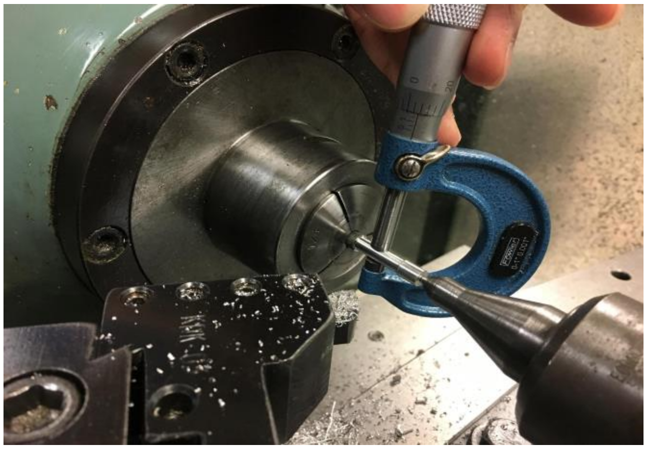

Figure 2.10 Sample preparation for tensile testing

Figure 2.11 Tensile testing procedure

2.6 Quasi-Static Compression Test

Quasi-static compression tests were carried out in an INSTRON – type machine with an extensometer. The samples were taken from the parallelepipeds, using Electrical Discharge Machining. Nine samples were compressed so that the mechanical behavior of each axis (x, y, and z) in three different conditions of cumulative strain could be seen, Figure 2.12.

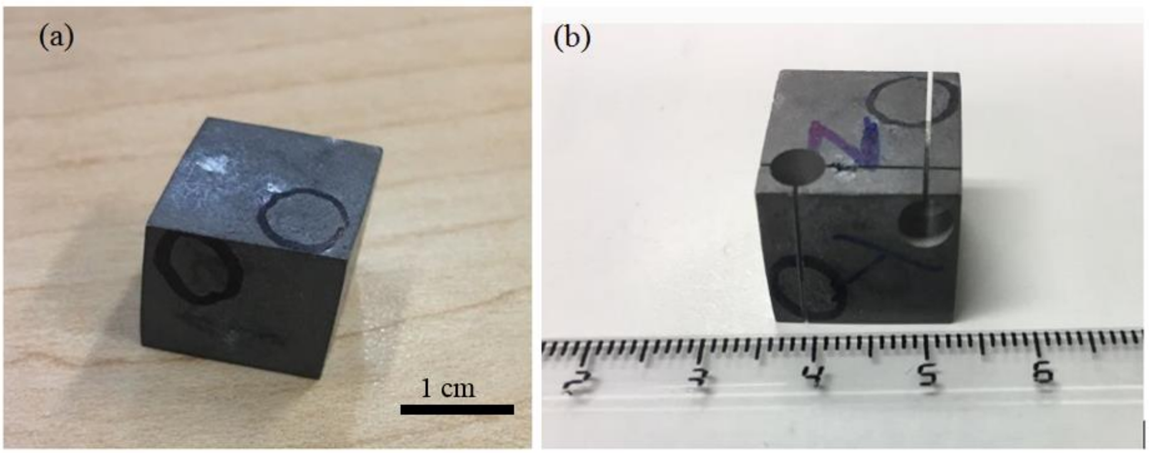

Figure 2.12 (a) Marks for cutting (b) Withdraw of the samples

The dimensions of the cylindrical specimens for quasi-static compression had length equal to 6mm and diameter equal to 4mm. Figure 2.13 indicates the samples from the three axes.

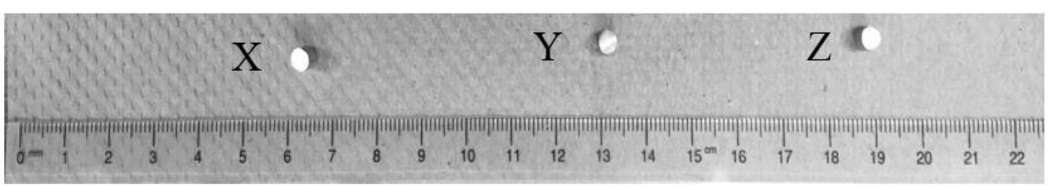

Figure 2.13 Cylindrical specimens for quasi–static compression

Figure 2.14 shows the disposition of the samples on the compression system. To make the results more accurate, an extensometer was plugged into the machine, and the results were analyzed by the Stress versus Strain curve.

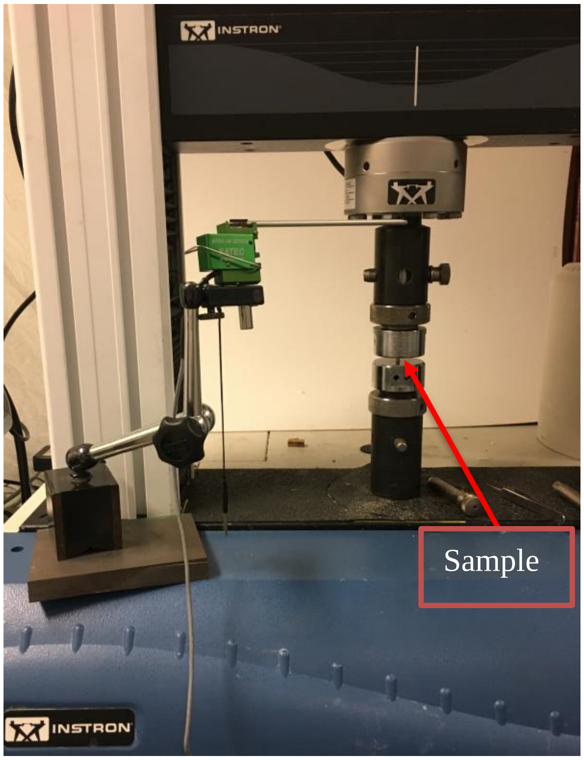

Figure 2.14 Quasi-static compression system

The strain rate for the quasi-static compression test is described by the derivation below [95].

The strain is defined by:

$$\varepsilon(t) = \frac{L(t) - L_0}{L_0} \tag{2.2}$$

where L_0 is the initial length, L(t) is the length at the time t, and ε is the strain.

Thus:

$$\dot{\varepsilon} = \frac{d\varepsilon}{dt} \tag{2.3}$$

It is known that:

$$\frac{d\varepsilon}{dt}=\frac{d}{dt}\left(\frac{L(t)-L_0}{L_0}\right) \quad (2.4)$$

Simplifying the Equation 2.4:

$$\dot{\varepsilon} = \frac{1}{L_0}\frac{dL}{dt}(t)$$

Combining Equation 2.3 with Equation 2.4, the strain rate is:

$$\dot{\varepsilon} = \frac{v(t)}{L_0} \quad (2.5)$$

where v(t) is the compression speed, which is equal to 1 μm/s.

The calculation for this value is shown by putting the measurement units on Equation 2.5.

$$\dot{\varepsilon} = \frac{v(t)}{L_0} = \frac{1\ \mu m/s}{6\ mm} = 1.6\text{x}10^{-2}\ \frac{1}{s}$$

The strain rate during the quasi-static compression for the nine samples was around $1.6\text{x}10^{-2}$ s^{-1} because specimens had different lengths, between 5.8 and 6.2 mm.

2.7 Dynamic Compression Test

The Hopkinson bar test was the experimental method to produce dynamic deformation, in which the intermediate strain rate testing is (10^2 -10^4 s^{-1}). This test, also known as the Kolsky bar test, is used to measure stress pulse propagation in a metal bar [96].

For compression testing, two symmetrical bars are positioned in sequence, with the sample in between the bars, Figure 2.15. The incident bar collides into the sample, which transmits this force into the transmitted bar [97]. The incident bar is started from a gas gun and collides with the sample. Thus, the strain scales are attached on both the incident and transmitted bars [98]. Figure 2.16 describes the Hopkinson bar system located in Dr. Meyer's lab at UCSD.

Figure 2.15 Hopkinson bar in Dr. Meyers lab at UCSD

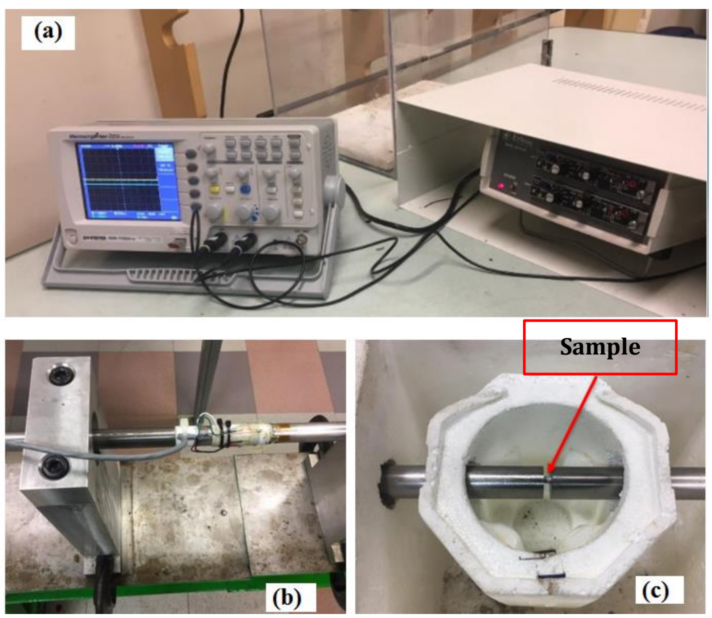

Figure 2.16 (a) Electronic system that reads the information generated by the two bars of operation, (b) the electronic system located at the bars to collect the data in both bars and (c) the sample placed between the incident and transmitted bars.

At the end of the incident bar, a stress wave is created which propagates through the bar in the direction of the specimen, and it splits into two smaller waves. Then, the transmitted wave goes through the specimen and finally to the transmitted bar. This performance causes plastic deformation [99] in the sample. The reflected wave is reflected back from the sample and travels back down the incident bar. The stress and the strain produced by this dynamic compression method can be calculated from the amplitudes of incident, transmitted, and reflected waves [100]. To plot a stress-strain curve, several derivations to convert the digital data received from the Hopkinson system are needed. Thus, the folowing equations define the derivation made [101], the derivations results can bee seen in Appendix C.

From the strain rate equation, already cited by Equation 2.5, is expressed the velocities as a function of strains in the strain gages:

$$\sigma = \rho U_\rho C \tag{2.6}$$

$$\frac{\sigma}{E} = \varepsilon \tag{2.7}$$

$$C\varepsilon = U_p$$

where Equation 2.7 indicates that the deformation is elastic and Hook's Law is assumed [101]. Also, C is the wave velocity and U_p is the particle velocity.

Therefore, the interfaces are:

$$V_1 = C_0\varepsilon_I \quad \text{at } t = 0 \tag{2.8}$$

$$V_2 = C_0\varepsilon_T$$

When t>0, V_1 is decreased because of the reflected wave, then:

$$V_I = C_0(\varepsilon_I - \varepsilon_R) \tag{2.9}$$

Putting together Equations 2.5, 2.6, and 2.7, the derived strain rate is found:

$$\mathring{\varepsilon}(t) = \frac{C_0}{L} = (\varepsilon_I - \varepsilon_R - \varepsilon_T) \tag{2.10}$$

Integrating the Equation 2.9 from 0 to t:

$$\varepsilon(t) = \frac{C_0}{L} \int_0^t [\varepsilon_I(t) - \varepsilon_R(t) - \varepsilon_T(t)] \tag{2.11}$$

To plot the curve, the stress can be found by the equilibrium of the interfaces:

$$\sigma = \frac{P_1(t) + P_2(t)}{2A} \tag{2.12}$$

where P_1 and P_2 are the forces acting on the interfaces 1 and 2.

$$P_1(t) = A_0\, E_0\, (\varepsilon_I - \varepsilon_R) \tag{2.13}$$

$$P_2(t) = A_0\, E_0\, (\varepsilon_T) \tag{2.14}$$

Combining the interfaces given by Equations 2.12 and 2.13:

$$\sigma = \frac{A_0 E_0}{2A} [(\varepsilon_I(t) + \varepsilon_R(t) + \varepsilon_T\,(t)] \tag{2.15}$$

E_0 is the Young's modulus of the bars, A_0 is the cross-sectional area of the bars, then during the equilibrium of forces (P_1 (t) = P_2 (t)), the equilibrium of strain is $\varepsilon_I + \varepsilon_R = \varepsilon_T$.

The stress is:

$$\sigma(t) = E_0 \frac{A_0}{A} \varepsilon_T(t) \tag{2.16}$$

Thus, the strain rate is:

$$\mathring{\varepsilon}(t) = -\frac{2C_0}{L}\, \varepsilon_R \tag{2.17}$$

Finally, the strain is:

$$\mathring{\varepsilon}(t) = -\frac{2C_0}{L} \int_0^t \varepsilon_R\, dt \tag{2.18}$$

The specimens tested had dimensions of length of 6mm and diameter of 4 mm. Also it is important to mention that, using the derivations described above, wave propagation is not being considered in a sample. This is because when the wave firstly reaches the sample, there are impacts, and after three of them, the specimen ranges the equilibrium.

2.8 Microstructure Analysis

The microstructure, fracture analysis, and phase's characterization of the samples after the SPD procedures performed and the initial state alloy was analyzed by Optical Microscope (OM), Scanning Electron Microscope (SEM), Energy Dispersive X-Ray Microanalysis (EDX), and X-Ray Diffraction Pattern (XRD).

a) Optical Microscope

The samples were grinded, polished, and etched with a solution made by [102]:

- 1 mL HNO_3
- 75 mL ethylene glycol
- 25 mL water

The difficulty in polishing magnesium alloy is the brittleness of the material. Once the sample is being grinded, the particles go away, and the sample does not keep its flatness. With silicon grind paper, this issue is minimized, and a successful sample preparation is possible. To polish the sample, diamond paste of 3µm, 2 µm, and 0.5µm was used in a metallographic polisher. Then, it was cleaned with ethanol and dried with compressed air.

b) Scanning Electrical Microscope

The characterization of the fracture surfaces of the specimens from the tensile test, quasi-static compression test, and dynamic compression test was performed through the SEM. The model of the SEM is FEI XL30, Figure 2.17, and enables high resolution at low KV. At 10 KV, a resolution of 1nm is possible and also a resolution of 1.7 nm at

1KV [103].

Figure 2.17 Scanning Electron Microscope at Nano3 Cleanroom [103]

c) Energy Dispersive X-Ray Microanalysis

In order to determine the phase's constituents of the material after SPD and to confirm the initial composition of WE43, EDX was carried out. This analytical technique is used for elemental analysis or chemical characterization because it is capable of separating peaks on the electromagnetic emission spectrum for each present atomic element [104].

d) X-Ray Diffraction Pattern

The initial state, MDF with the cumulative strain equal to 2.77, and ECAP samples were analyzed by X-Ray Diffraction Pattern in order to provide information about the phases and elements present in the material. This analytical procedure was performed by an X-Ray Diffraction Pattern System located in Dr. Olivia Graeve‘s laboratory at UCSD.

The specimens were ground and polished, allowing the X-rays generated by short wavelength and high energy waves of electromagnetic radiation to be characterized by wavelength or photon energy. The X-rays are produced by high speed electrons accelerated by a high voltage filled colliding with a metal target, and the rapid deceleration of electrons on target enables the kinetic energy of electrons to be converted to energy of X-ray radiation.

e) Microhardness Testing

A measurement of the Microhardness can quantify the amount of strength of a material after plastic deformation [105]. The Hardness Vickers (HV) equation shows that the HV value is determined by the ratio F/A as the derivation below shows [106]. The diamond indenter touches the material, making a 22-degree-angle indentation relative to the horizontal surface on each side, Figure 2.18 [107].

The area of indentation is given by:

$$A = \frac{d^2}{2\sin(136°/2)} \tag{2.19}$$

A is approximately:

$$A \approx \frac{d^2}{1.8544}$$

The diameter d is in millimeters, and the force applied is in kgf.

$$HV = \frac{1.8544F}{d^2}\ [kgf/mm^2] \tag{2.20}$$

To convert the HV value from kgf/mm^2 to MPa is necessary to multiply the number by the standard gravity (9.8).

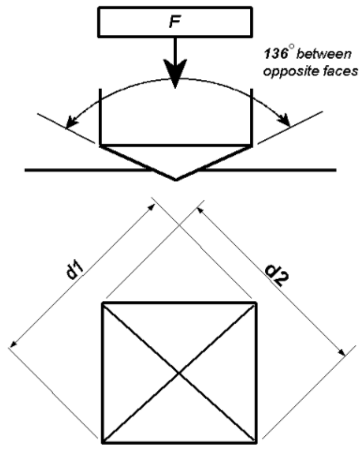

Figure 2.18 Sketch of the indentation procedure [107]

Microhardness evaluation was completed on an LM-810AT (LECO corp., Michigan, USA) instrument equipped with a Vickers indenter, Figure 2.19. Samples were embedded in epoxy and polished. A load of 25 gf was utilized to indent the samples.

Figure 2.19 Microindenter at Graeve's group laboratory

Chapter 3 Results and Discussion

3.1 Microstructure Evaluation

The microstructure of the WE43 before any mechanical processing showed equi-axed grains with an average grain size of 18 µm and secondary phases along the grain boundaries. The average grain size after the ECAP procedure was 14 µm, and the average grain size after 20 passes of MDF was 12 µm. By increasing the number of passes and consequently increasing the cumulative strain, the grain size was decreased as early studies showed [108]. Some details of the measurement procedure by SEM are shown in Appendix D. The initial microstructure of WE43 magnesium alloy, the microstructure of the ECAP sample after one pass, and the microstructure of the MDF sample after 20 passes are illustrated in Figure 3.1.

The α-Mg matrix phase and the secondary phases $Mg_{24}Y_5$, $Mg_{41}Nd_5$, and $Mg_{12}Nd$ were found in the WE43 magnesium alloy both before and after the mechanical procedures. Also, a Zr-LA phase was found because of the presence of zirconium in the grain boundaries, as seen in Figure 3.2.

Figure 3.3 shows the Hall-Petch relation, in which can be observed the lower yield point related to the grain size. The strengthening coefficient used is the theoretical. σ_y is the minor stress required to move the dislocations. The plot indicates that the yield stress to move dislocations after MDF was greater than the non-processed sample.

Comparing the results shown in Figure 3.3 with other metals, it is reasonable say that while the grain size of WE43 after mechanical processing decreased, the slope of yield stress increased. The Hall-Petch equation is very useful for characterizing materials [73].

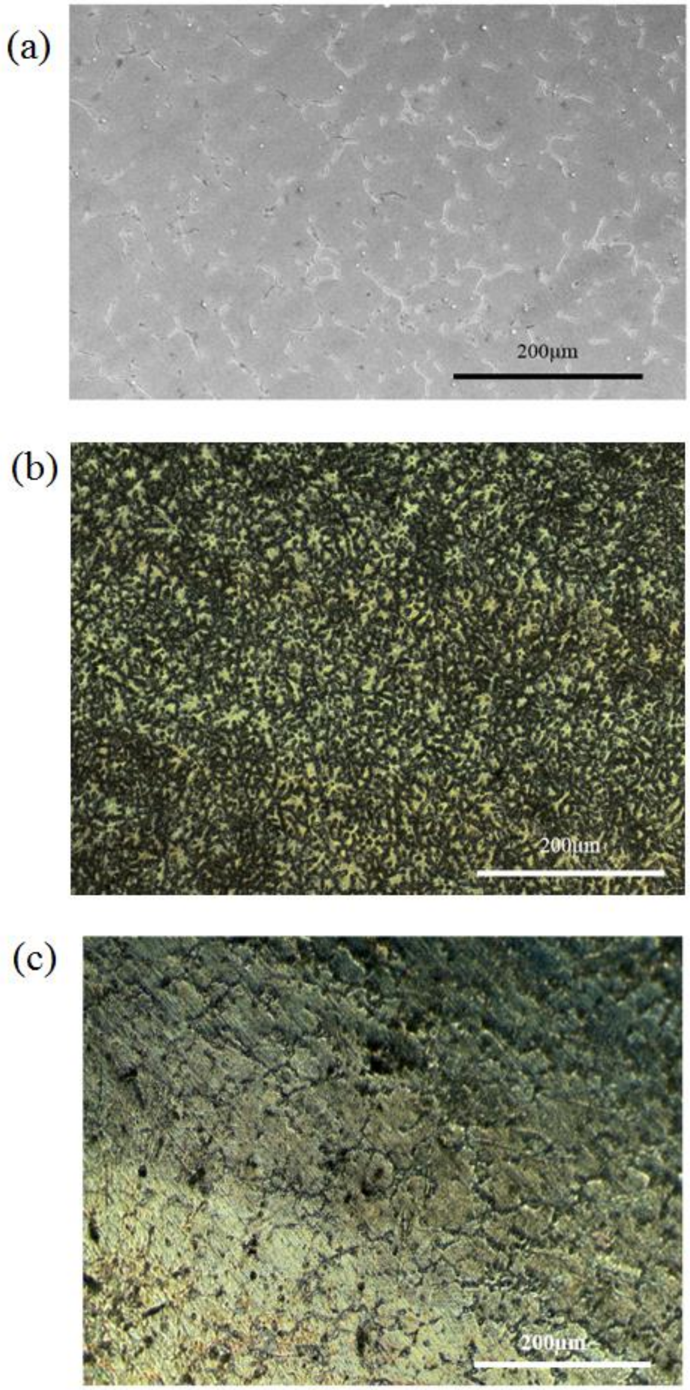

Figure 3.1 Microstructure of (a) as received material, (b) ECAP sample, and (c) MDF sample

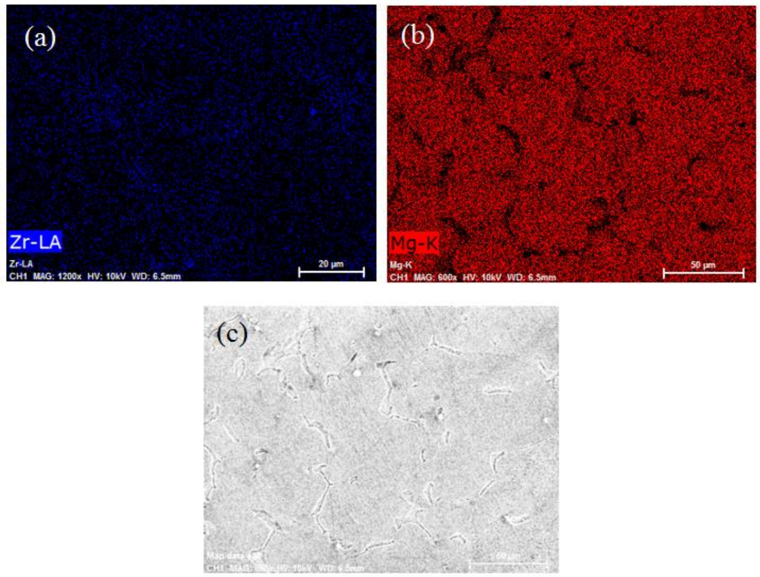

Figure 3.2 EDX reveals the phases present in WE43 magnesium alloy **(a)** Zr-LA phase, (b) α-Mg phase, and (c) region analyzed

In transverse sections of WE43, there were sections constituted of recrystallized grains with $Mg_{12}Nd$, phases with Zr, Nd along the grain boundaries, Y particles, and the equilibrium β-phase $Mg_{14}Nd_2Y$ with the matrix Mg-K.

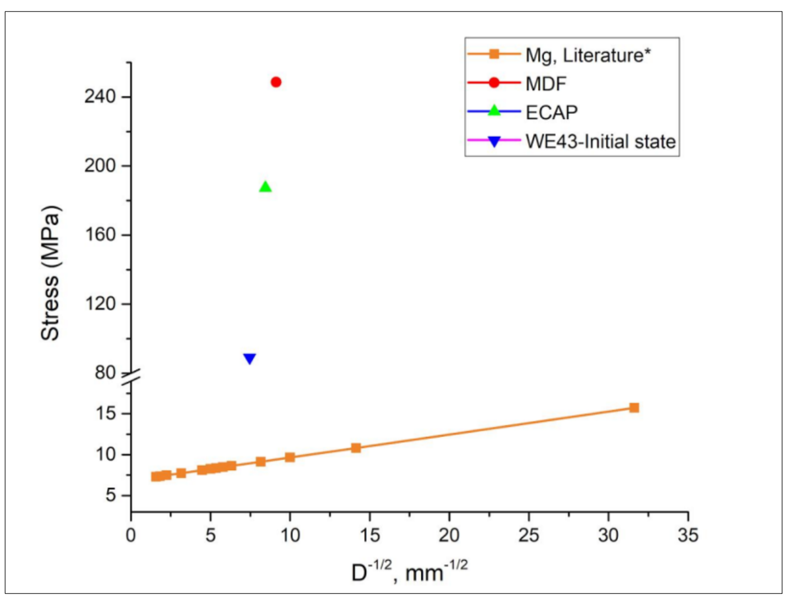

Figure 3.3 Hall-Petch relation

The XRD analysis, shown in Figure 3.4, confirms that the amount of the secondary phases did not change significantly after the mechanical processing, and the grain boundaries remained practically constant. This was attributed to the formation of non-equilibrium grain boundaries containing an excess of uniform dislocations [109]. The spectrogram in Figure 3.5 relates the exact amount of each chemical element present in the alloy in its initial state.

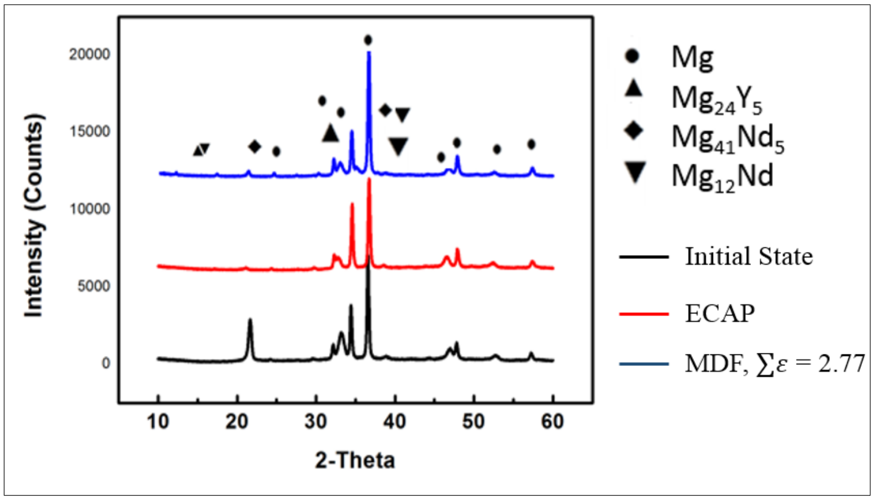

Figure 3.4 XRD analysis WE43 magnesium Alloy

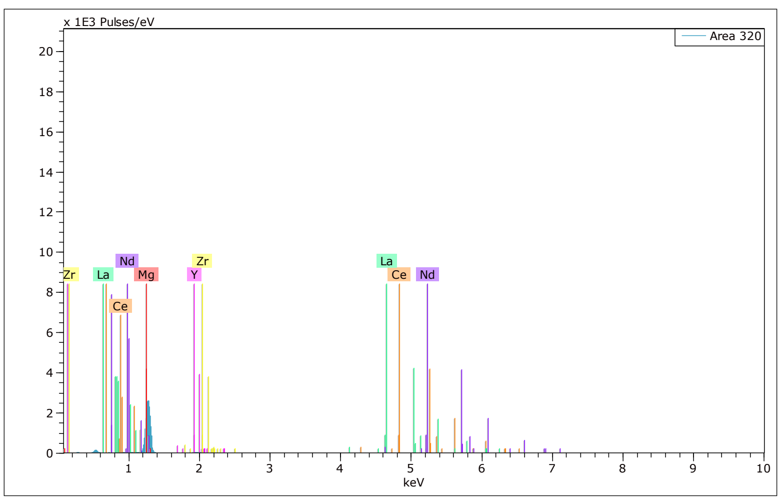

Figure 3.5 EDX spectrum analysis WE43 magnesium alloys

3.2 Quasi-Static Evaluation

An increase in yield stress was observed during the quasi-static compression compared to the compression of the material in its initial form. Table 3.1 and Figure 3.6 show the summary of the results of the quasi-static compression test.

Table 3.1 Summary of quasi-static compression test results

Specimen		Yield Stress (MPa)	Maximum Stress (MPa)	Strain (mm/mm)
$\sum\varepsilon = 1.82$	x	108	424	0.23
	y	103	421	0.18
	z	98	395	0.16
$\sum\varepsilon = 2.15$	x	112	426	0.24
	y	92	328	0.18
	z	90	312	0.16
$\sum\varepsilon = 1.22$	x	95	383	0.23
	y	96	385	0.18
	z	115	430	0.28
Initial State		87	293	0.18

The $\sum\varepsilon = 1.82$ sample supported 18 completed passes, the $\sum\varepsilon = 2.15$ sample supported 20 passes, and the $\sum\varepsilon = 1.22$ sample presented a crack during the 13^{th} pass on the y-axis. Considering this information and the strain rate compressive properties (about $6x10^{-3}$ s^{-1}), the results shown in Table 3.1 and the curves 3.6 to 3.7 are reasonable in terms of improvement of plasticity and strength after MDF. It was observed that during the x-axis passes, the strain was a bit higher than during the other passes, because when the specimen was compressed in the x-axis, the temperature was higher than in the other axes.

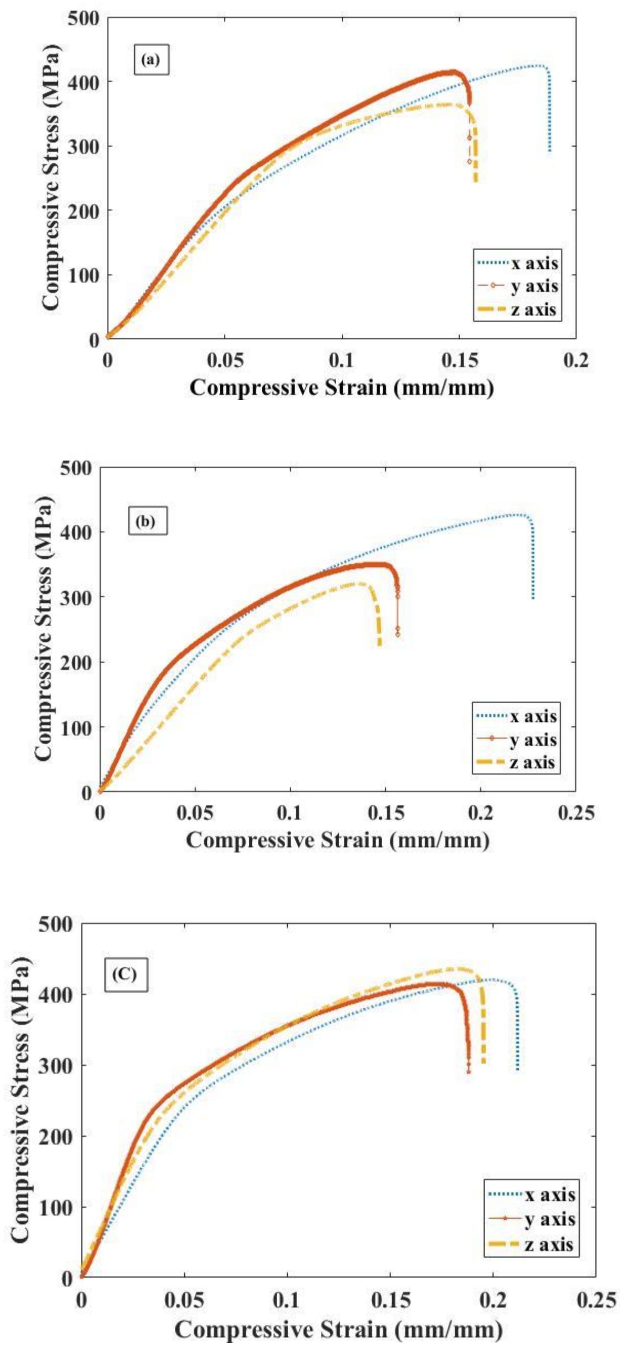

Figure 3.6 Compressive stress-strain curves of the MDF specimen with (a) $\sum\varepsilon = 1.82$,

(b)$\varepsilon = 2.15$ and (c) $\sum\varepsilon = 1.22$

The comparison between the mechanical behaviors of the axes during quasi-static compression can be seen in Figure 3.7. It is noted that during y and z axes, the sample with $\sum\varepsilon = 1.22$ showed a different behavior during the compression test due to the crack that originated during the 13th pass.

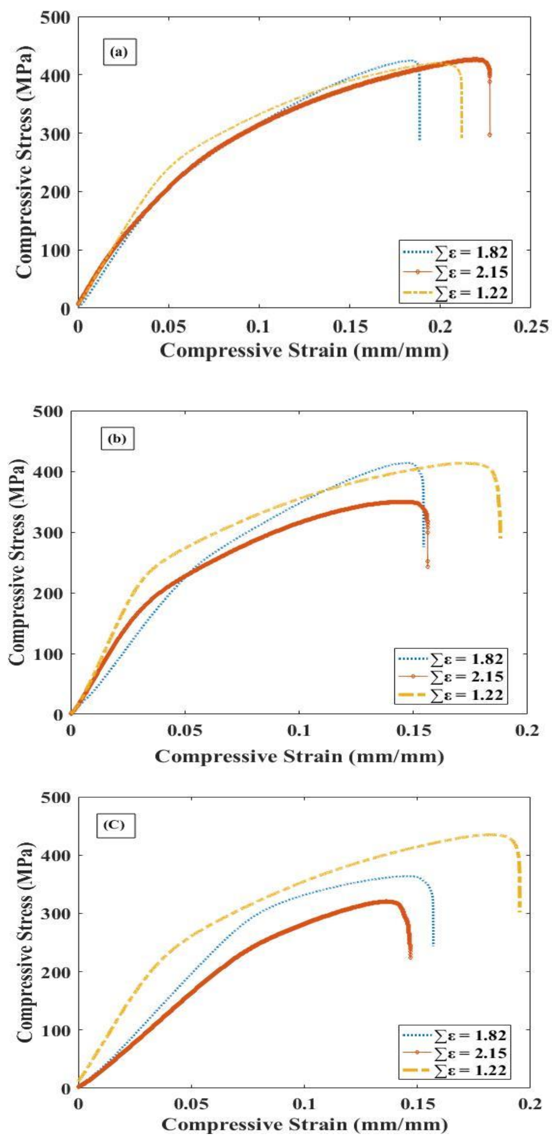

Figure 3.7 Compressive stress-strain curve of the MDF on (a) X axis, (b) Y axis, and (c) Z axis

Even though pressure stress was not uniform throughout the specimen, satisfactory plastic deformation was still achieved. The minimal variation of the strain exhibited a perfectly plastic behavior with maximum stress about 400MP and strain of approximately 3% in the X axis.

3.3 Dynamic Compression Evaluation

The dynamic compression test showed smaller strain because the test is conducted very quickly. Sometimes the sample did not even broke. However, the yield stress was greater when compressed in quasi-static mode. Table 3.2 shows the values of stress-strain.

Table 3.2 Summary of dynamic compression test results

Specimen		**Yield Stress (MPa)**	**Maximum Stress (MPa)**	**Strain (mm/mm)**
$\sum\varepsilon = 1.82$	x	205	447	0.06
	y	246	515	0.063
	z	240	508	0.08
$\sum\varepsilon = 2.15$	x	121	413	0.042
	y	183	445	0.048
	z	103	283	0.022

The stress found in dynamic compression test is higher than the one found in quasi static-compression test, what can be explained by non-local failure, Figures 3.8 and 3.9. The main difference between the tests is how the fracture starts and its angle. Also, the surface presents the slip systems in a different disposition because of the dynamic shear.

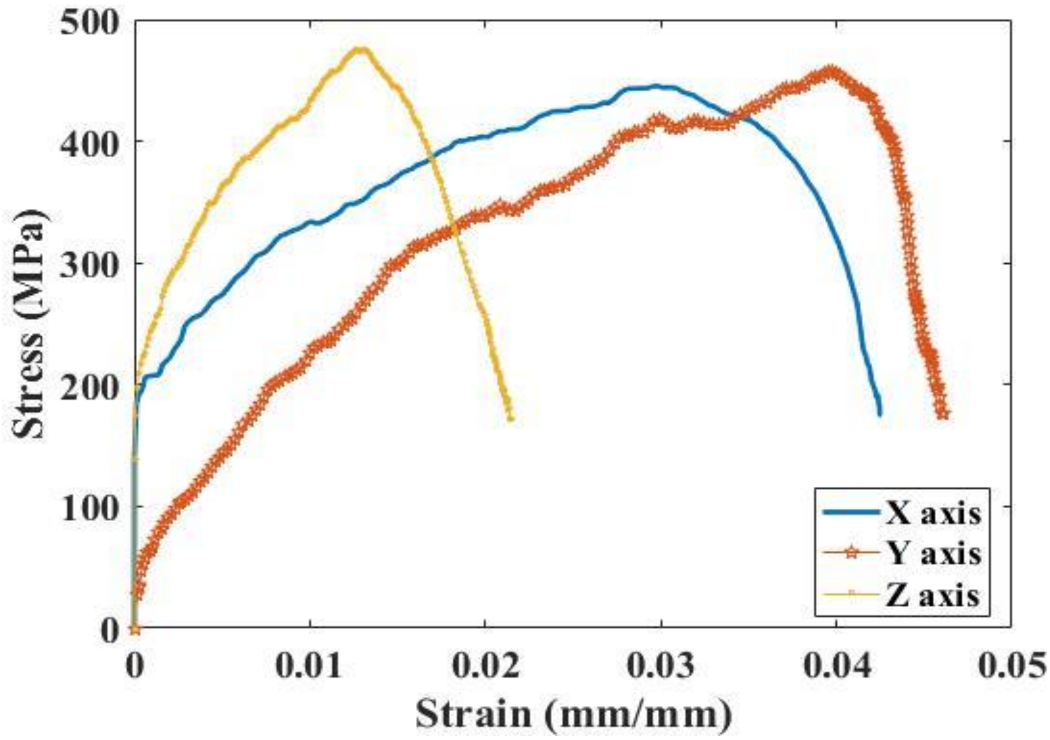

Figure 3.8 Stress-strain curve of the MDF specimen with ∑ε = 1.82

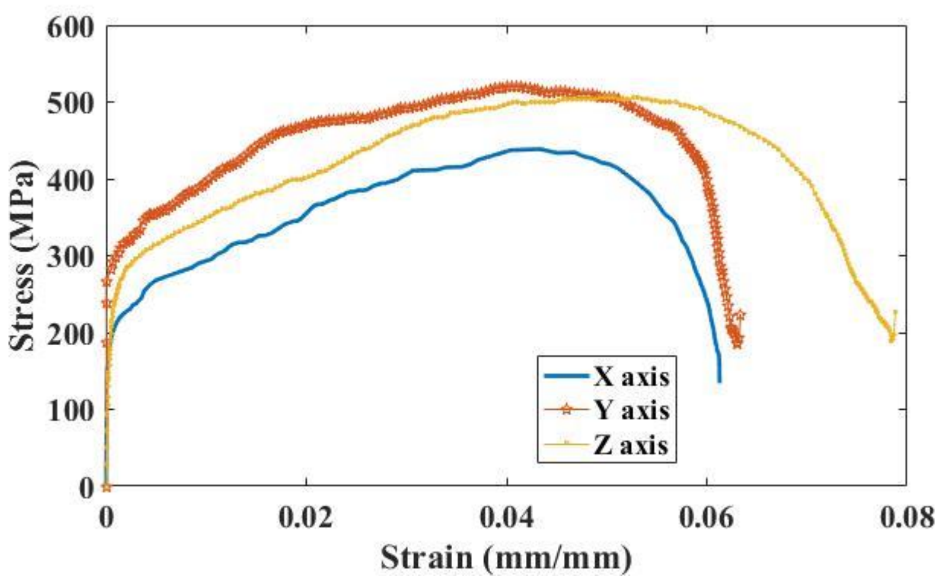

Figure 3.9 Stress-strain curve of the MDF specimen with ∑ε = 2.15

3.4 Fracture Surface Analysis

The evolution of the fracture morphology of the samples after tensile testing, compression quasi-static testing, and dynamic compression testing showed mostly brittle structure that could be seen by the presence of a minimum number of dimples and tearing ridges of different sizes. Figure 3.10 shows the tensile response of the initial state. The specimen fractures at a strain of 0.19. The fracture mode surface resulting from tensile testing of the initial state was a mix of some ductile and predominantly brittle fractures. The facture surfaces of the specimen during the tensile test are shown in Figure 3.11.

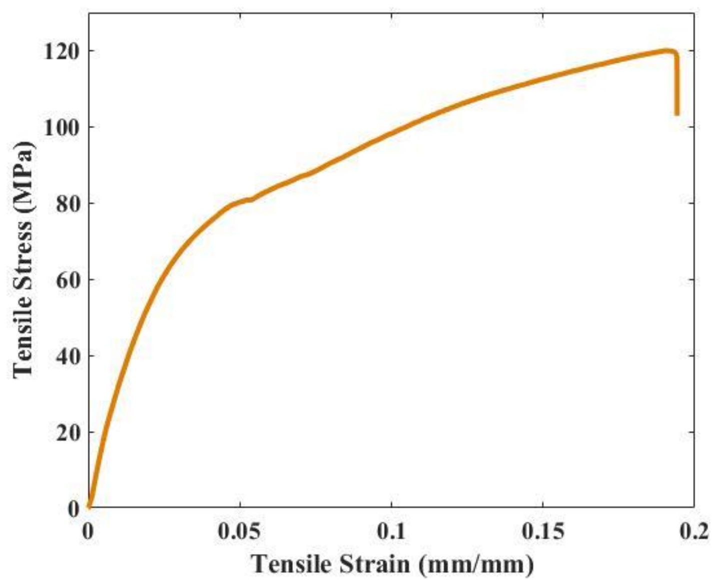

Figure 3.10 Tensile Stress-strain curve of the initial state WE43 magnesium alloy

In accordance with the fracture surfaces of the compression tests, Figures 3.13, a lack of dimples in the fracture surface indicates decreased ductility. In contrast, the compression surfaces of the material processed by both MDF and ECAP presented predominantly brittle surfaces, which explains why the failure occurred by cleavage. Thus, the drop in the number of active slip systems indicates that ductility and strength were reduced after MDF and ECAP.

In figure 3.11 are shown the three stages of the crack: the crack initiation zone, the crack propagation zone, and the final stage of the crack.

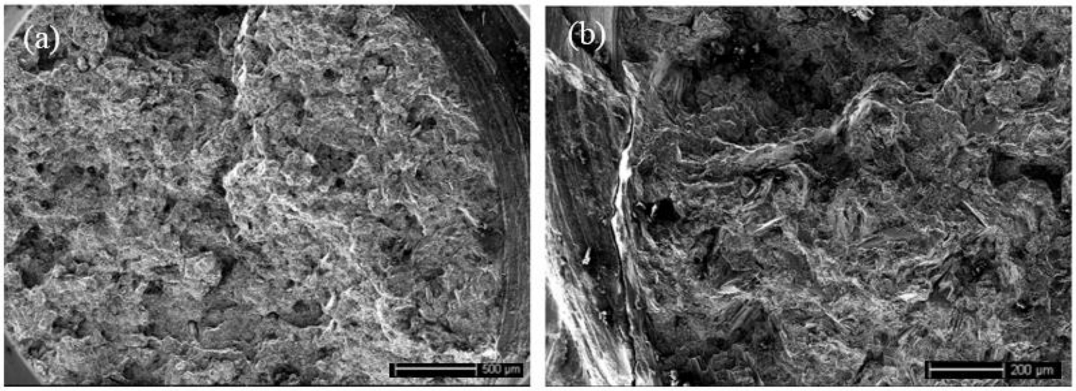

Figure 3.11 (a) Crack initiation zone, (b) propagation and final stage of the crack

The red marks show non-deformed areas, Figure 3.12(a), probably due to the presence of yttrium in the grain boundaries. Figure 3.12(b) shows how the fracture happens in these regions.

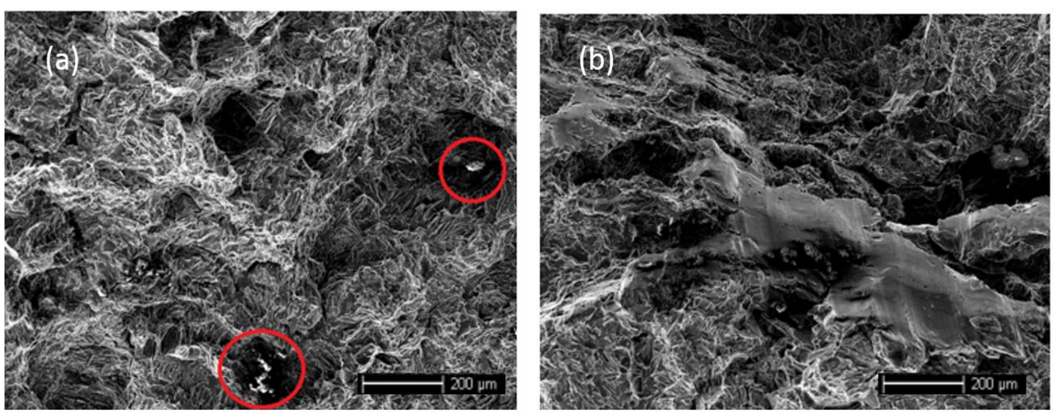

Figure 3.12 (a) Non-deformed areas (b) second phase region with presence of yttrium

Figure 3.13 (a) displays the fracture surface after quasi-static compression test showing the beginning of the fracture. The crack did not start from the very edge of the sample, then it is possible to visualize a portion of the sample surface. Figure 3.13 (b) shows the fracture surface after quasi-static compression showing some ductile regions with predomint brittle regions of the same sample. As the dynamic compression test did not show very large strain, and the strain ratio is significantly greater than in quasi-static compression test, the surface does not show brittleness as in quasi-static compression, Figure 3.14.

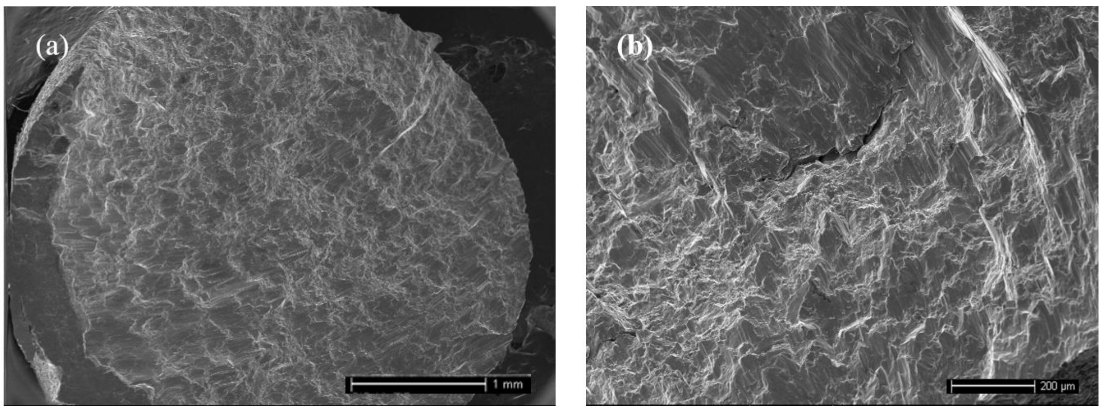

Figure 3.13 (a) Fracture surface after quasi-static compression of $\sum\varepsilon = 2.15$ sample along y-axis, (b) internal crack region

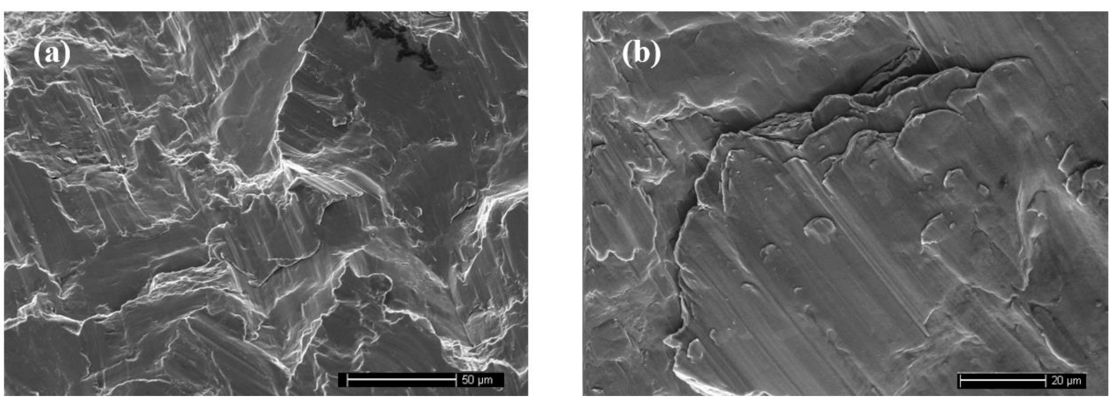

Figure 3.14 Fracture surface after dynamic compression test of $\sum\varepsilon = 2.15$ sample along y-axis

Details of the fracture surfaces of tensile, quasi-static compression test can be seen in Appendix E.

3.5 Microhardness Testing Evaluation

The Microhardness value in the center of the specimens after ECAP and MDF increased compared to the edges or even the initial material, Figure 3.15. It is due to the non-uniform compression applied during the procedures. The evolution of hardness is attributed to shear strain accumulation at different positions during the deformation process.

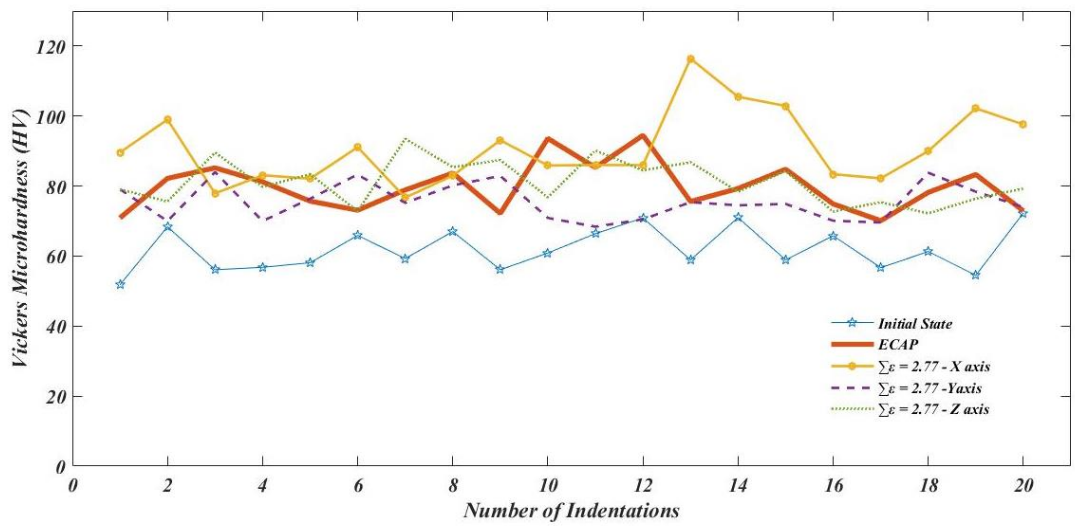

Figure 3.15 Microhardness evolution

Chapter 4 Conclusions

The following are the main conclusions form this investigation:

1. A moderate decrease in grain size occurred after several passes of Multi Direction Forging and one pass of ECAP. The MDF procedure consists of straining a sample sequentially in compression along x, y, and z directions. It showed consistent results, but the strain at each pass was small (0.02-0.09) because otherwise cracking of the sample would occur. This limited the reduction in grain size.
2. The decrease in grain size in our investigation was less than expected because although the sample was being heated between passes, it still was able to undergo cooling and recrystallization during compression passes.
3. The ductility decreased with MDF, and the fractures exhibited many cleavage planes.
4. Moderate decreases in grain size from 18 μm to 14 μm in ECAP and to 12 μm in Multi Directional Forging were obtained. This decrease in grain size resulted in an increase in the hardness. In view of the brittleness of the magnesium alloy, it was not possible to increase the plastic strain per pass; the samples fractured if the stress was increased beyond 230 MPa.
5. In MDF, high strain rate experiments were conducted at a strain rate of $3x10^{-3}$ s^{-1}, and the yield stress increased to 246 MPa. This shows that magnesium has high strain-rate sensitivity.
6. The presence of second phases did not change significantly after mechanical processing.

7. New methods of processing which subject the alloy to higher strains per pass without fracture need to be developed.

Appendix A

Multi Directional Forging Calculations

Pass	Axis	Dimension x	Dimension y	Dimension z	Engineering Strain x	Engineering Strain y	Engineering Strain z	Cumulative Strain $\varepsilon_x+\varepsilon_y+\varepsilon_z$	True Strain			Cumulative Strain $\varepsilon_x+\varepsilon_y+\varepsilon_z$	Speed	Temperature /Time	Applied Stress	Cumulative Strain	
1	x	19.45	16.36	13.32	0.02828	0.022	0.02402		0.02789	0.02177	0.02374					Engineering	True
	y	19.84	15.96	13.4	0.01966	0.02506	0.00597	0.06849181	0.01947	0.02475	0.00595	0.06767682				1.828861667	1.79064295
	z	20.02	16.2	13.2	0.00899	0.01481	0.01515		0.00895	0.01471	0.01504						
2	x	19.62	16.16	13.28	0.02039	0.00248	0.00602		0.02018	0.00247	0.00601						
	y	19.82	15.96	13.34	0.01009	0.01253	0.0045	0.0512393	0.01004	0.01245	0.00449	0.05079059	2 mm/min	300°C/10 min between passes	220-230 MPa		
	z	19.9	16.08	13.1	0.00402	0.00746	0.01832		0.00401	0.00743	0.01815						
3	x	19.7	16.12	13.2	0.01015	0.00248	0.00758		0.0101	0.00248	0.00755						
	y	19.9	15.98	13.26	0.01005	0.00876	0.00452	0.02958397	0.01	0.00872	0.00451	0.02943809				After 8 passes, sample 01 has been heated in 550°C for 30 min.	
	z	19.94	16.08	13.12	0.00201	0.00622	0.01067		0.002	0.0062	0.01061						
4	x	19.7	16.18	13.18	0.01218	0.00618	0.00455		0.01211	0.00616	0.00454						
	y	19.9	15.96	13.26	0.01005	0.01378	0.00603	0.03663793	0.01	0.01369	0.00602	0.03641365					
	z	19.94	16.2	13.12	0.00201	0.01481	0.01067		0.002	0.01471	0.01061						
5	x	19	16.4	13.64	0.04947	0.0122	0.03812		0.04829	0.01212	0.03741						
	y	19.42	16.98	12.9	0.02163	0.03416	0.05736	0.10635879	0.0214	0.03359	0.05578	0.10434905					
	z	19.8	16.24	13.2	0.01919	0.04557	0.02273		0.01901	0.04456	0.02247						
6	x	18.64	15.9	13.52	0.06223	0.02138	0.02367		0.06037	0.02116	0.02339						
	y	19.2	16.08	13.74	0.02917	0.01119	0.01601	0.10806434	0.02875	0.01113	0.01588	0.10555611		550°C/10 min between passes			
	z	19.5	16.38	13.28	0.01538	0.01832	0.03464		0.01527	0.01815	0.03405				250-260 MPa		
7	x	19.4	17	13.58	0.00515	0.03647	0.02209		0.00514	0.03582	0.02185						
	y	18.94	16.1	13.88	0.02429	0.0559	0.02161	0.09687616	0.024	0.05439	0.02138	0.09472972					
	z	19.26	16.36	13.4	0.01661	0.01589	0.03582		0.01648	0.01577	0.03519						
8	x	18.2	16.98	12.86	0.05824	0.03651	0.04199		0.05661	0.03586	0.04113						
	y	18.7	16.3	14.06	0.02674	0.04172	0.08535	0.13836428	0.02639	0.04087	0.0819	0.1351655					
	z	18.96	16.7	13.54	0.01371	0.02395	0.0384		0.01362	0.02367	0.03769						
9	x	18.2	17.08	13.78	0.04176	0.02225	0.01742		0.04091	0.022	0.01727						
	y	18.62	16.5	13.98	0.02256	0.03515	0.01431	0.11246531	0.02231	0.03455	0.0142	0.11039576					
	z	18.1	16.6	13.5	0.02873	0.00602	0.03556		0.02832	0.00601	0.03494						
10	x	17.92	17	13.06	0.01004	0.02353	0.03369		0.00999	0.02326	0.03314						
	y	18.4	16.48	13.06	0.02609	0.03155	0	0.07704856	0.02575	0.03107	0	0.07589696					
	z	18.54	16.86	13.54	0.00755	0.02254	0.03545		0.00752	0.02229	0.03484						

Figure A1 Strain calculation in sample 01, $\sum\varepsilon = 1.82$ during MDF

33	11	x	17.88	17.2	12.98	0.03691	0.01977	0.04314	0.10598261	0.03625	0.01957	0.04224	0.10414755	3 mm/min	550°C/20 min between passes	210-220 Mpa
34		y	18.26	16.66	14.14	0.02081	0.03241	0.08204		0.0206	0.0319	0.07885				
35		z	18.48	17.7	13.64	0.0119	0.05876	0.03666		0.01183	0.0571	0.036				
36	12	x	17.66	17.26	13.98	0.04643	0.02549	0.02432	0.10886128	0.04539	0.02517	0.02403	0.10684911			
37		y	17.1	16.68	14.12	0.03275	0.03477	0.00992		0.03222	0.03418	0.00987				
38		z	18.3	17	13.74	0.06557	0.01882	0.02766		0.06351	0.01865	0.02728				
39	13	x	18.76	17.62	14.06	0.03859	0.03519	0.02276	0.13632276	0.03787	0.03458	0.0225	0.13314006			
40		y	18.06	16.6	14.28	0.13012	0.06145	0.01541		0.12232	0.05963	0.01529				
41		z	18.3	16.96	13.78	0.06486	0.02123	0.03628		0.06284	0.021	0.03564				
42	14	x	17.6	17.3	14.12	0.0578	0.01965	0.02408	0.13601189	0.05619	0.01946	0.02379	0.13289527			
43		y	17.98	16.58	14.28	0.06152	0.04343	0.0112		0.0597	0.04251	0.01114				
44		z	18.14	17.98	13.8	0	0.07786	0.03478		0	0.07498	0.03419				
45	15	x	17.26	17.46	14.24	0.03895	0.02978	0.0309	0.10680331	0.03821	0.02935	0.03043	0.10491144			
46		y	17.44	16.8	14.4	0.02738	0.03929	0.01111		0.02701	0.03853	0.01105				
47		z	17.88	17.08	14	0.02108	0.01639	0.02857		0.02086	0.01626	0.02817				
48	16	x	17.38	17.34	14.12	0.03114	0.01499	0.0085	0.17920247	0.03067	0.01488	0.00846	0.17239732			
49		y	17.86	16.7	14.36	0.04072	0.03832	0.01671		0.03991	0.03761	0.01657				
50		z	18.06	17.06	12.94	0.04689	0.0211	0.10974		0.04583	0.02088	0.10412				
51	17	x	17.36	17.38	14.2	0.03913	0.01841	0.08873	0.11080183	0.03838	0.01824	0.08501	0.10880132			
52		y	17.98	16.78	14.42	0.03456	0.03576	0.01526		0.03398	0.03513	0.01514				
53		z	17.98	17.1	13.92	0.05146	0.01871	0.03592		0.05018	0.01854	0.03529				
54	18	x	17.5	17.45	14.3	0.03037	0.02006	0.02657	0.11974509	0.02992	0.01986	0.02623	0.11708862			
55		y	17.2	16.98	14.8	0.03062	0.02768	0.03378		0.03016	0.0273	0.03323				
56		z	17.76	17.3	13.94	0.00578	0.0185	0.06169		0.00576	0.01833	0.05986				
57	19	x	Failure during x compression													
58		y														
59		z														

Figure A.1 Strain calculation in sample 01, $\sum\varepsilon = 1.82$ during MDF, Continued

Pass	Axis	Dimension x	Dimension y	Dimension z	Engineering Strain x	Engineering Strain y	Engineering Strain z	Cumulative Strain $\varepsilon_x+\varepsilon_y+\varepsilon_z$	True Strain x	True Strain y	True Strain z	Cumulative Strain $\varepsilon_x+\varepsilon_y+\varepsilon_z$	Speed	Temperature/Tim	Applied Stress	
	x	19.62	16.34	13.3	0.01937	0.02081	0.02256		0.01918	0.02059	0.02231					
1	y	19.92	15.9	13.34	0.01506	0.02767	0.003	0.06226165	0.01495	0.0273	0.00299	0.06158583				
	z	20.02	16.22	13.14	0.005	0.01973	0.01522		0.00498	0.01954	0.01511					
	x	19.72	16.26	13.24	0.01521	0.00246	0.00755		0.0151	0.00246	0.00752					
2	y	19.84	15.9	13.3	0.00605	0.02264	0.00451	0.051574	0.00603	0.02239	0.0045	0.05111367	2 mm/min	300°C/10 min between passes	220-230 MPa	
	z	19.98	16.1	13.12	0.00701	0.01242	0.01372		0.00698	0.01235	0.01363					
	x	19.76	16.08	13.2	0.01113	0.00124	0.00606		0.01107	0.00124	0.00604					
3	y	19.92	15.98	13.24	0.00803	0.00626	0.00302	0.02653777	0.008	0.00624	0.00302	0.02641517				
	z	19.98	16.04	13.12	0.003	0.00374	0.00915		0.003	0.00373	0.0091					
	x	19.8	16.08	13.18	0.00909	0.00249	0.00455		0.00905	0.00248	0.00454					
4	y	19.92	15.98	13.22	0.00602	0.00626	0.00303	0.01838363	0.00601	0.00624	0.00302	0.01831846				
	z	19.96	16.18	13.18	0.002	0.01236	0.00303		0.002	0.01229	0.00303					
	x	19.02	16.62	13.62	0.04942	0.02647	0.03231		0.04824	0.02613	0.03179					
5	y	19.6	16	13.58	0.02959	0.03875	0.00295	0.11076202	0.02916	0.03802	0.00294	0.10859626				
	z	19.72	16.28	13.28	0.00609	0.0172	0.02259		0.00607	0.01705	0.02234					
	x	18.64	16.58	13.6	0.05794	0.01809	0.02353		0.05632	0.01793	0.02326					
6	y	19.22	16.08	13.7	0.03018	0.03109	0.0073	0.11295073	0.02973	0.03062	0.00727	0.1105792		550°C/10 min between passes		
	z	19.42	16.3	13.38	0.0103	0.0135	0.02392		0.01025	0.01341	0.02363					
	x	18.4	16.7	13.4	0.05543	0.02395	0.00149		0.05395	0.02367	0.00149					
7	y	18.84	16.2	13.9	0.02335	0.03086	0.03597	0.11898843	0.02309	0.0304	0.03534	0.11651679				
	z	19.22	16.4	13.46	0.01977	0.0122	0.03269		0.01958	0.01212	0.03217				250-260 MPa	
	x	18.04	16.92	13.88	0.06541	0.03073	0.03026		0.06336	0.03027	0.02981					
8	y	18.64	16.28	13.2	0.03219	0.03931	0.05152	0.12839088	0.03168	0.03856	0.05023	0.12531176				
	z	18.9	16.54	13.52	0.01376	0.01572	0.02367		0.01366	0.0156	0.02339					
	x	17.9	16.9	13.96	0.05587	0.0213	0.03152		0.05436	0.02108	0.03103					
9	y	18.3	16.34	14.16	0.02186	0.03427	0.01412	0.13438544	0.02162	0.0337	0.01403	0.13135555				55 min before test
	z	18.6	16.68	13.56	0.01613	0.02038	0.04425		0.016	0.02018	0.0433					
	x	17.74	16.08	14.06	0.04848	0.03731	0.03556		0.04734	0.03663	0.03494					
10	y	18.2	16.48	14.14	0.02527	0.02427	0.00566	0.10186194	0.02496	0.02398	0.00564	0.10001794				
	z	18.36	16.8	13.74	0.00871	0.01905	0.02911		0.00868	0.01887	0.0287					Crack

Cumulative Strain	
Engineering	True
2.149457716	1.725172

Figure A.2 Strain calculation in sample 01, $\sum\varepsilon = 2.15$ during MDF

33		x	17.6	17.36	14.12	0.04318	0.03226	0.02691		0.04228	0.03175	0.02656				
34	11	y	17.08	16.46	14.32	0.03044	0.05468	0.01397	0.19770622	0.02999	0.05324	0.01387	0.19068152			
35		z	18.3	16.9	13.02	0.06667	0.02604	0.09985		0.06454	0.0257	0.09517				
36		x	17.44	17.36	14.22	0.04931	0.0265	0.08439		0.04813	0.02615	0.08102				
37	12	y	18	16.66	14.14	0.03111	0.04202	0.00566	0.10859492	0.03064	0.04116	0.00564	0.10641153			
38		z	18.1	16.98	13.9	0.00552	0.01885	0.01727		0.00551	0.01867	0.01712		3 mm/min		
39		x	17.42	17.26	14.22	0.03904	0.01622	0.0225		0.03829	0.01609	0.02225				
40	13	y	17.82	17.86	14.4	0.02245	0.03359	0.0125	0.11159126	0.0222	0.03304	0.01242	0.10955683			
41		z	18.08	17.06	13.86	0.01438	0.04689	0.03896		0.01428	0.04583	0.03822				
42		x	17.3	17.4	14.26	0.04509	0.01954	0.02805		0.0441	0.01935	0.02766				
43	14	y	17.7	16.72	14.38	0.0226	0.04067	0.00834	0.11880254	0.02235	0.03986	0.00831	0.11647615		550°C/20 min between passes	
44		z	17.92	17.08	13.92	0.01228	0.02108	0.03305		0.0122	0.02086	0.03251				
45		x	17.14	17.5	14.36	0.04551	0.024	0.03064		0.0445	0.02372	0.03018				
46	15	y	17.58	17.8	14.52	0.02503	0.01685	0.01102	0.10696583	0.02472	0.01671	0.01096	0.10485414			
47		z	17.12	17.16	13.9	0.02687	0.0373	0.0446		0.02651	0.03662	0.04364				220-230 MPa
48		x	17.06	17.48	14.42	0.00352	0.01831	0.03606		0.00351	0.01814	0.03543				
49	16	y	17.66	16.8	14.4	0.03398	0.04048	0.00139	0.07109733	0.03341	0.03968	0.00139				
50		z	17.62	17.18	14.02	0.00227	0.02212	0.0271		0.00227	0.02188	0.02674				
51		x	16.88	17.56	14.44	0.04384	0.02164	0.02909		0.04291	0.02141	0.02867				
52	17	y	17.3	16.88	14.7	0.02428	0.04028	0.01769	0.12667641	0.02399	0.03949	0.01753	0.12407193			
53		z	17.66	17.2	14.1	0.02039	0.0186	0.04255		0.02018	0.01843	0.04167				
54		x	16.76	17.66	14.52	0.0537	0.02605	0.02893		0.05231	0.02571	0.02852				
55	18	y	17.1	16.96	14.62	0.01988	0.04127	0.00684	0.12600249	0.01969	0.04044	0.00682	0.1233096			
56		z	17.38	17.3	14.18	0.01611	0.01965	0.03103		0.01598	0.01946	0.03056				
57		x	16.68	17.6	14.52	0.04197	0.01705	0.02342		0.04111	0.0169	0.02315				
58	19	y	16.98	17.08	14.84	0.01767	0.03044	0.02156	0.18820087	0.01751	0.02999	0.02133	0.18066264			
59		z	17.5	17.2	13.3	0.02971	0.00698	0.11579		0.02928	0.00695	0.10956				
60		x	16.45	17.66	14.6	0.06383	0.02605	0.08904		0.06188	0.02571	0.0853				
61	20	y	16.88	17.4	15	0.02547	0.01494	0.02667	0.12772336	0.02515	0.01483	0.02632	0.12449806			
62		z	17.16	17.36	14.3	0.01632	0.0023	0.04895		0.01619	0.0023	0.04779				

Figure A.2 Strain calculation in sample 01, $\sum\varepsilon = 2.15$ during MDF, Continued

Pass	Axis	Dimension			Engineering Strain			Cumulative Strain	True Strain			Cumulative Strain	Speed	Temperature	Applied Stress		
		x	y	z	x	y	z	$\varepsilon_x+\varepsilon_y+\varepsilon_z$				$\varepsilon_x+\varepsilon_y+\varepsilon_z$				Cumulative Strain	
1	x	19.56	16.24	13.3	0.01709	0.01478	0.02256		0.01694	0.01467	0.02231					Engineering	True
	y	19.9	15.9	13.4	0.00503	0.02138	0.00746	0.05825599	0.00501	0.02116	0.00743	0.05769303				1.222614936	1.176839
	z	22.24	16.08	13.14	0.10072	0.01119	0.01979		0.09596	0.01113	0.01959						
2	x	19.72	16.14	13.24	0.0142	0.00372	0.00755		0.0141	0.00371	0.00752						
	y	19.94	15.96	13.26	0.00301	0.01128	0.00151	0.03769072	0.003	0.01122	0.00151	0.03745375		300°C/10 min between passes	220-230 MPa		
	z	19.98	16.04	13.1	0.001	0.00499	0.01221		0.001	0.00498	0.01214		2 mm/min				
3	x	19.78	16.12	13.14	0.01112	0.00496	0.00304		0.01106	0.00495	0.00304						
	y	19.94	15.98	13.2	0.00301	0.00876	0.00455	0.02444951	0.003	0.00872	0.00454	0.02433956					
	z	20.02	16.08	13.14	0.001	0.00622	0.00457		0.001	0.0062	0.00456						
4	x	19.82	16.16	13.18	0.00908	0.00495	0.00303		0.00904	0.00494	0.00303						
	y	19.94	15.96	13.22	0.00301	0.01253	0.00303	0.03077337	0.003	0.01245	0.00302	0.03061281					
	z	19.94	16.08	13.1	0.00301	0.00746	0.00916		0.003	0.00743	0.00912						
5	x	19	16.64	13.5	0.05263	0.03365	0.02963		0.05129	0.0331	0.0292						
	y	19.4	15.96	12.9	0.03093	0.04261	0.04651	0.12676963	0.03046	0.04172	0.04546	0.12406176					
	z	19.62	16.28	13.32	0.01937	0.01966	0.03153		0.01918	0.01947	0.03104						
6	x	18.4	16.78	13.68	0.08696	0.0298	0.02632		0.08338	0.02936	0.02598			550°C/10 min between passes			
	y	19.24	16.2	12.98	0.0395	0.0358	0.05393	0.15410227	0.03874	0.03518	0.05253	0.14942018					
	z	19.22	16.5	13.4	0.04058	0.01818	0.03134		0.03978	0.01802	0.03086						
7	x	18.14	16.78	13.92	0.10254	0.01669	0.03736		0.09761	0.01655	0.03668						
	y	18.76	16.26	14	0.0661	0.03198	0.00571	0.17155319	0.06401	0.03148	0.0057	0.16546007					
	z	19.02	16.6	13.5	0.05152	0.02048	0.03704		0.05024	0.02027	0.03637				250-260 MPa		
8	x	17.94	16.8	13.92	0.11483	0.0119	0.03017		0.1087	0.01183	0.02973		3 mm/min				
	y	18.44	16.4	14	0.0846	0.02439	0.00571	0.16561041	0.08121	0.0241	0.0057	0.15884765					
	z	18.7	17.68	13.64	0.06952	0.0724	0.02639		0.06721	0.0699	0.02605						
9	x	17.44	17.46	14.18	0.14679	0.0126	0.03808		0.13697	0.01252	0.03737						
	y	17.92	16.42	14.44	0.11607	0.06334	0.01801	0.26722741	0.10981	0.06141	0.01785	0.25390858		550°C/20 min between passes			
	z	18.4	16.88	13.66	0.08696	0.02725	0.0571		0.08338	0.02689	0.05553						
10	x	17.34	16.4	14.24	0.1534	0.02927	0.04073		0.14272	0.02885	0.03992						
	y	18.2	16.44	14.26	0.0989	0.00243	0.0014	0.18618245	0.09431	0.00243	0.0014	0.1750419				Crack	
	z	17.9	17	13.84	0.11732	0.03294	0.03035		0.11093	0.03241	0.0299						

Figure A.3 Strain calculation in sample 01, $\sum\varepsilon = 1.22$ during MDF

Pass	Axis	Dimension			Engineering Strain			Cumulative Strain	True Strain			Cumulative Strain	Speed	Temperature	Applied Stress	Cumulative Strain	
		x	y	z	x	y	z	εx+εy+εz	x	y	z	εx+εy+εz				Engineering	True
	x	19.52	16.34	13.28	0.02459	0.02081	0.02108		0.02429	0.02059	0.02087					2.774099006	2.645401
1	y	19.88	15.92	13.34	0.018109	0.02638	0.0045	0.06619277	0.01795	0.02604	0.00449	0.06543863					
	z	20.06	16.08	13.14	0.008973	0.00995	0.01522		0.00893	0.0099	0.01511						
	x	19.72	16.08	13.24	0.017241	0	0.00755		0.01709	0	0.00752						
2	y	19.82	15.92	13.3	0.005045	0.01005	0.00451	0.03946819	0.00503	0.01	0.0045	0.03919754	2 mm/min	300°C/10 min between passes	220-230 MPa		
	z	19.98	16.02	13.14	0.008008	0.00624	0.01218		0.00798	0.00622	0.0121						
	x	19.72	16.14	13.18	0.013185	0.00743	0.00303		0.0131	0.00741	0.00303						
3	y	19.88	15.94	13.26	0.008048	0.01255	0.00603	0.03486406	0.00802	0.01247	0.00602	0.03465839					
	z	19.92	16.06	13.14	0.002008	0.00747	0.00913		0.00201	0.00744	0.00909						
	x	19.82	16.12	13.2	0.005045	0.00372	0.00455		0.00503	0.00372	0.00454						
4	y	19.92	15.96	13.22	0.00502	0.01003	0.00151	0.02115875	0.00501	0.00998	0.00151	0.02107769					
	z	19.92	16.06	13.14	0	0.00623	0.00609		0	0.00621	0.00607						
	x	18.88	16.6	13.74	0.055085	0.03253	0.04367		0.05362	0.03201	0.04274						
5	y	19.42	16	13.6	0.027806	0.0375	0.01029	0.12132907	0.02743	0.03681	0.01024	0.11877402					
	z	19.62	16.3	13.22	0.010194	0.0184	0.02874		0.01014	0.01824	0.02834						
	x	18.48	16.8	13.7	0.061688	0.02976	0.03504		0.05986	0.02933	0.03444						
6	y	19.12	16.1	13.82	0.033473	0.04348	0.00868	0.13344038	0.03292	0.04256	0.00865	0.13030149		550°C/10 min between passes			
	z	19.36	16.38	13.44	0.012397	0.01709	0.02827		0.01232	0.01695	0.02788						
	x	18.2	16.74	13.8	0.063736	0.02151	0.02609		0.06179	0.02128	0.02575						
7	y	18.74	16.22	14	0.028815	0.03206	0.01429	0.12672328	0.02841	0.03156	0.01418	0.12380271					
	z	18.86	16.7	13.58	0.006363	0.02874	0.03093		0.00634	0.02834	0.03046				250-260		
	x	17.8	16.9	14.12	0.059551	0.01183	0.03824		0.05784	0.01176	0.03753						
8	y	18.4	16.36	14.1	0.032609	0.03301	0.00142	0.12175498	0.03209	0.03247	0.00142	0.11909808					
	z	18.54	16.78	13.7	0.007551	0.02503	0.0292		0.00752	0.02472	0.02878						
	x	17.66	17	14	0.04983	0.01294	0.02143		0.04863	0.01286	0.0212						
9	y	18.08	16.4	14.24	0.02323	0.03659	0.01685	0.12431637	0.02296	0.03593	0.01671	0.12176066					
	z	18.38	17.86	13.72	0.016322	0.08175	0.0379		0.01619	0.07858	0.0372						
	x	17.28	17.3	14.36	0.063657	0.03237	0.04457		0.06171	0.03186	0.0436						
10	y	17.78	17.58	14.52	0.028121	0.01593	0.01102	0.10791321	0.02773	0.0158	0.01096	0.10544981					
	z	17.76	16.66	14.12	0.001126	0.05522	0.02833		0.00113	0.05375	0.02793						
	x	18.24	16.28	13.28	0.026316	0.02334	0.06325		0.02598	0.02307	0.06133						
11	y	18.22	16.3	14.38	0.001098	0.00123	0.0765	0.05468564	0.0011	0.00123	0.07371	0.05398275					
	z	18.1	16.54	14	0.00663	0.01451	0.02714		0.00661	0.01441	0.02678						

Figure A.4 Strain calculation in sample 01, ∑ε = 2.77 during MDF

36		x	17.56	16.88	14.34	0.030752	0.02014	0.02371		0.03029	0.01994	0.02343				
37	12	y	17.86	16.5	14.58	0.016797	0.02303	0.01646	0.0762224	0.01666	0.02277	0.01633	0.07524977			
38		z	18.1	16.86	14.26	0.01326	0.02135	0.02244		0.01317	0.02113	0.02219		3 mm/min		
39		x	17.28	17.3	14.42	0.047454	0.02543	0.0111		0.04636	0.02512	0.01103				
40	13	y	17.7	16.68	14.64	0.023729	0.03717	0.01503	0.20218122	0.02345	0.0365	0.01492	0.19400356			
41		z	17.9	16.88	13.1	0.011173	0.01185	0.11756		0.01111	0.01178	0.11115				
42		x	17.42	17.12	14.32	0.027555	0.01402	0.0852		0.02718	0.01392	0.08176				
43	14	y	17.7	16.58	14.5	0.015819	0.18069	0.01241	0.23953864	0.0157	0.1661	0.01234	0.22409523		550°C/20 min between passes	
44		z	17.9	16.9	14.06	0.011173	0.17923	0.03129		0.01111	0.16486	0.03081				
45		x	17.16	17.3	14.42	0.043124	0.17198	0.02497		0.04222	0.1587	0.02466				
46	15	y	17.46	16.7	14.66	0.017182	0.18008	0.01637	0.25414773	0.01704	0.16558	0.01624	0.2382767			
47		z	17.8	16.98	14.22	0.019101	0.1744	0.03094		0.01892	0.16076	0.03047				210-220 MPa
48		x	16.98	17.36	14.56	0.048292	0.16621	0.02335		0.04716	0.15376	0.02308				
49	16	y	17.56	16.78	14.52	0.03303	0.19559	0.00275	0.26641961	0.0325	0.17864	0.00275	0.24808902			
50		z	17.7	17	14.2	0.00791	0.18169	0.02254		0.00788	0.16695	0.02229				
51		x	16.88	17.46	14.82	0.048578	0.1471	0.04184		0.04744	0.13724	0.04098				
52	17	y	17.22	16.82	14.8	0.019744	0.17973	0.00135	0.26472249	0.01955	0.16529	0.00135	0.24848774			
53		z	17.52	17.08	14.28	0.017123	0.17787	0.03641		0.01698	0.16371	0.03577				
54		x	17.1	17.62	14.72	0.024561	0.16033	0.02989		0.02426	0.1487	0.02945				
55	18	y	17.26	16.82	14.76	0.00927	0.19377	0.00271	0.2490546	0.00923	0.17711	0.00271	0.23164208			
56		z	17.08	17.06	14.32	0.010539	0.17458	0.03073		0.01048	0.16091	0.03026				
57		x	16.58	17.86	14.72	0.030157	0.15897	0.02717		0.02971	0.14753	0.02681				
58	19	y	17	16.88	14.98	0.024706	0.19226	0.01736	0.2699656	0.02441	0.17585	0.01721	0.25201508			
59		z	17.2	17.2	14.4	0.009324	0.18042	0.04755		0.00928	0.16587	0.04646				
60		x								0	0	0				
61	20	y							0	0	0	0	0			
62		z								0	0	0				

Figure A.4 Strain calculation in sample 01, $\sum\varepsilon = 2.77$ during MDF, Continued

Appendix B

Stress-Strain curves of Multi Directional Forging

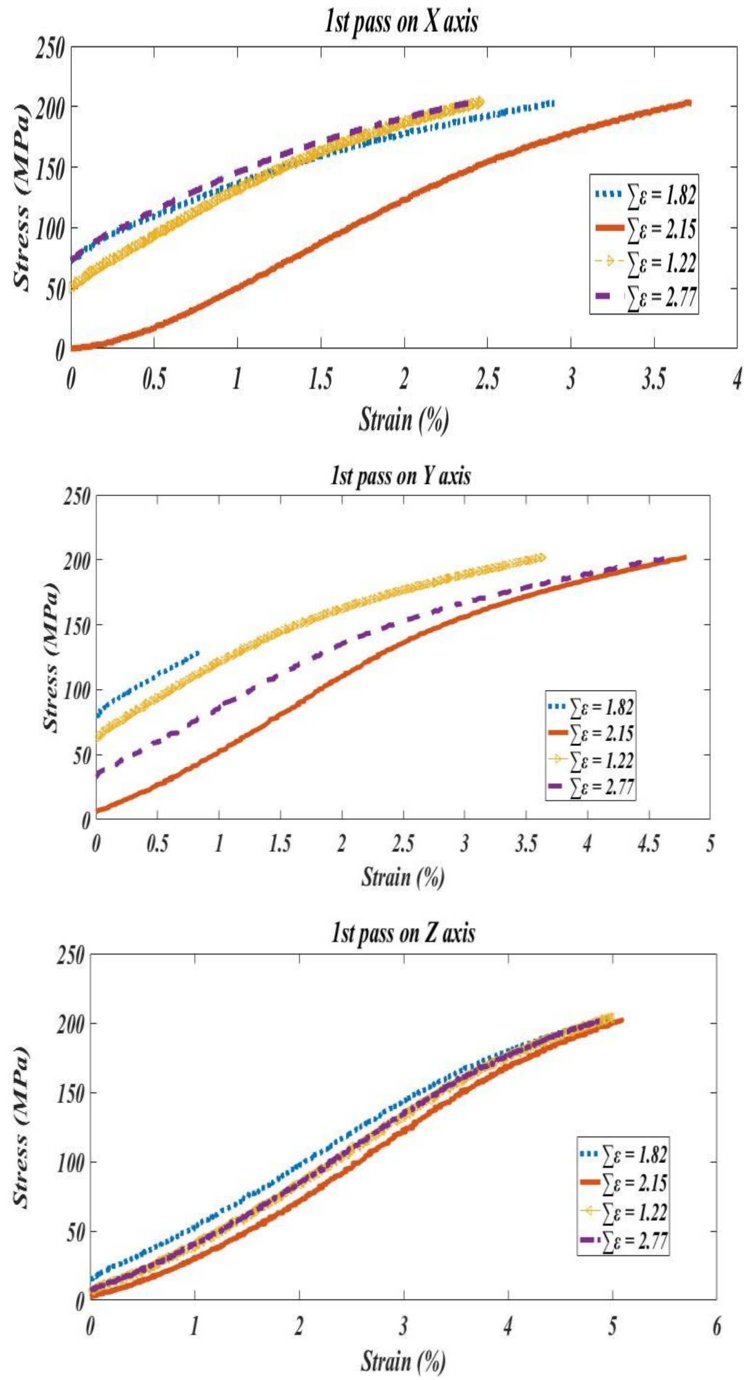

Figure B.1 Stress-strain curves in three dimensions during 1st pass: (a) stress-strain curve on X axis; (b) stress-strain curve on Y axis; (c) stress-strain curve on Y axis

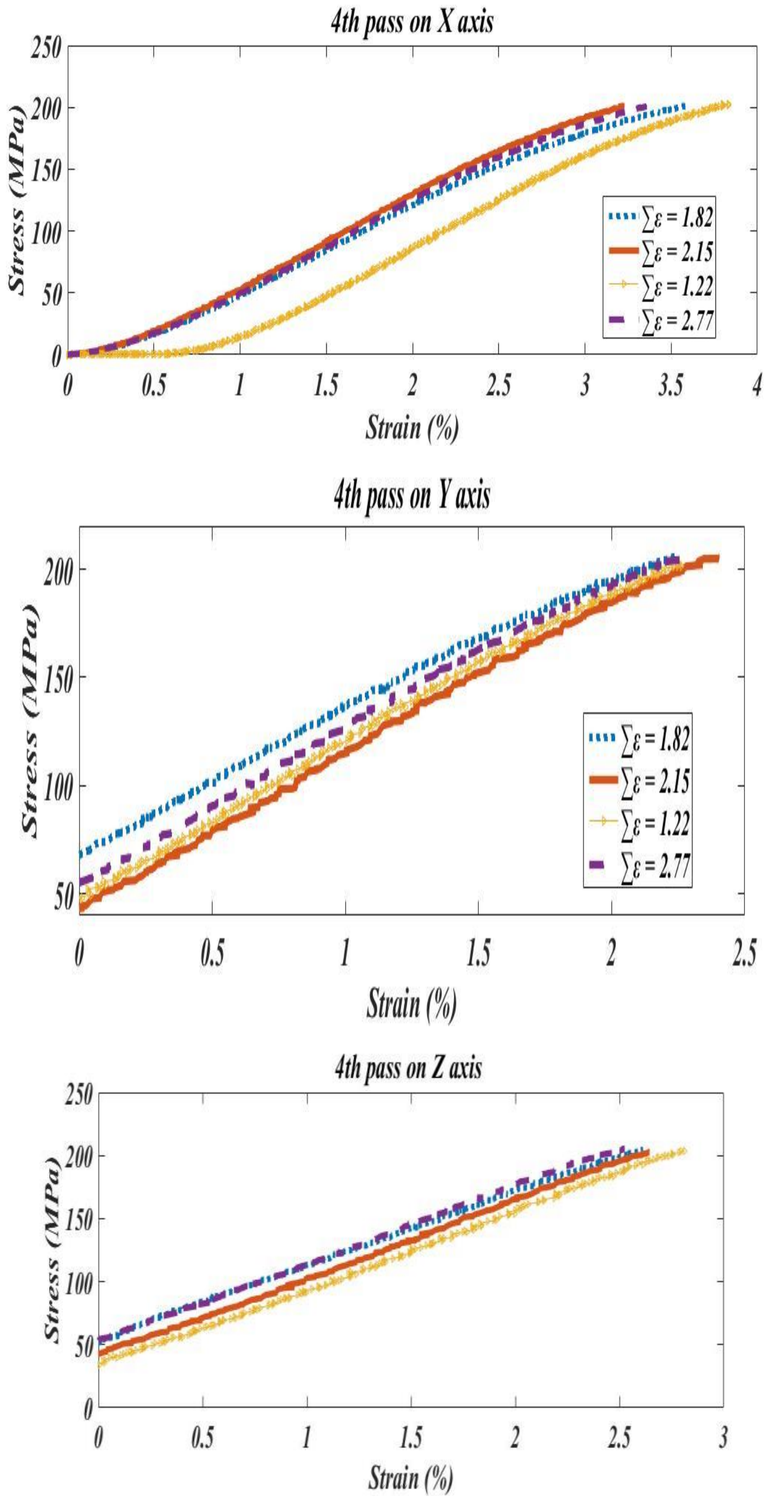

Figure B.2 Stress-strain curves in three dimensions during 4st pass: (a) stress-strain curve on X axis; (b) stress-strain curve on Y axis; (c) stress-strain curve on Y axis.

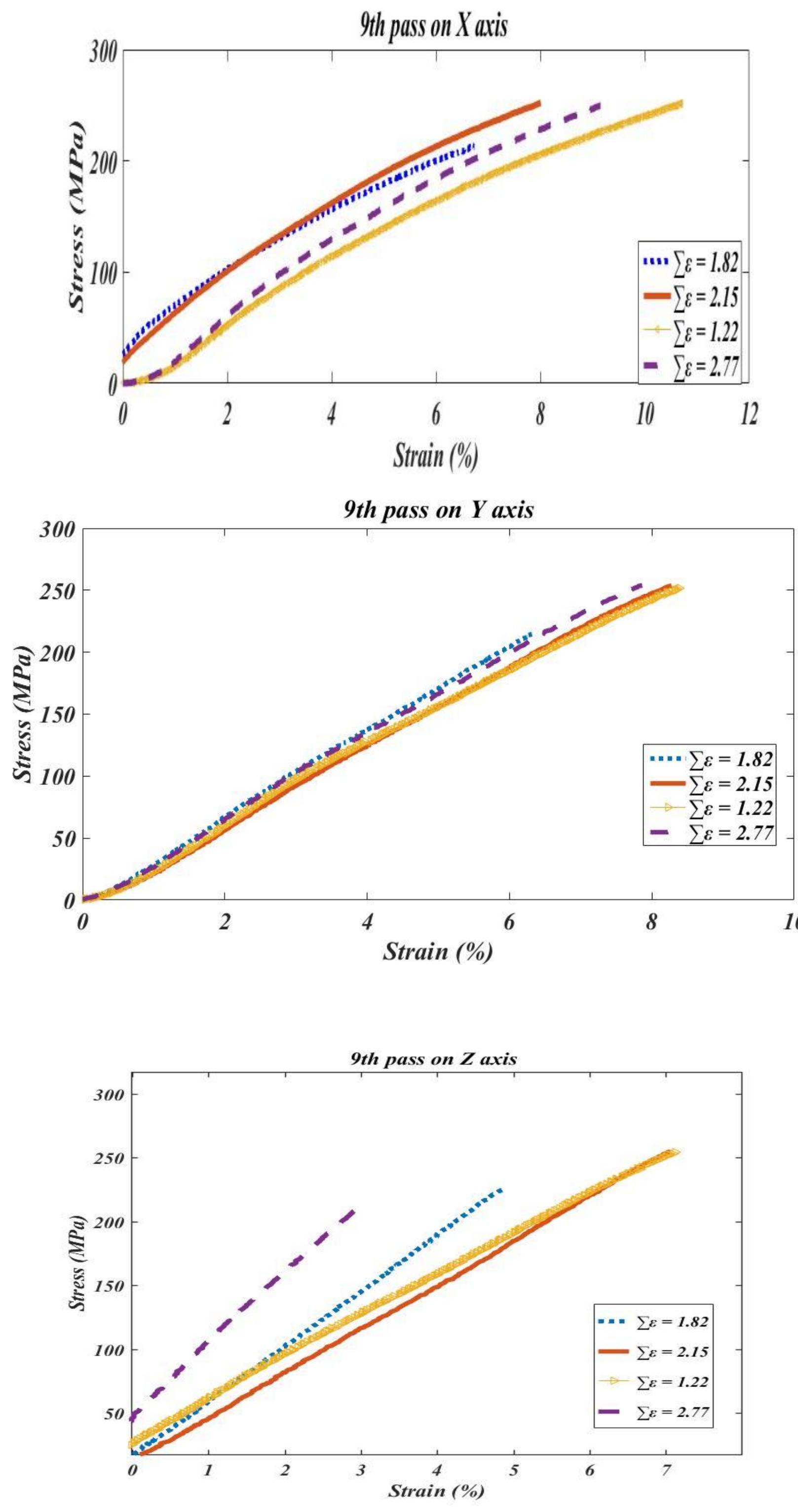

Figure B.3 Stress-strain curves in three dimensions during 9st pass: (a) stress-strain curve on X axis; (b) stress-strain curve on Y axis; (c) stress-strain curve on Y axis.

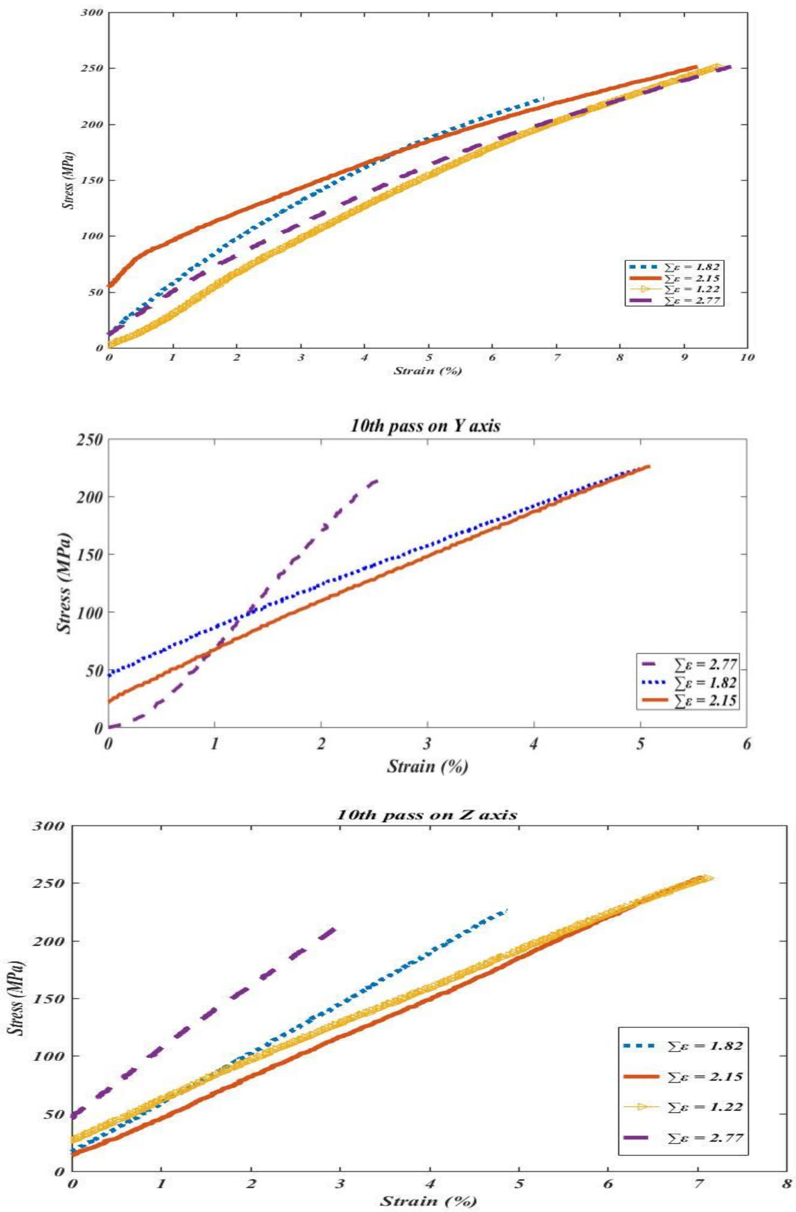

Figure B.4 Stress-strain curves in three dimensions during 10st pass: (a) stress-strain curve on X axis; (b) stress-strain curve on Y axis; (c) stress-strain curve on Y axis.

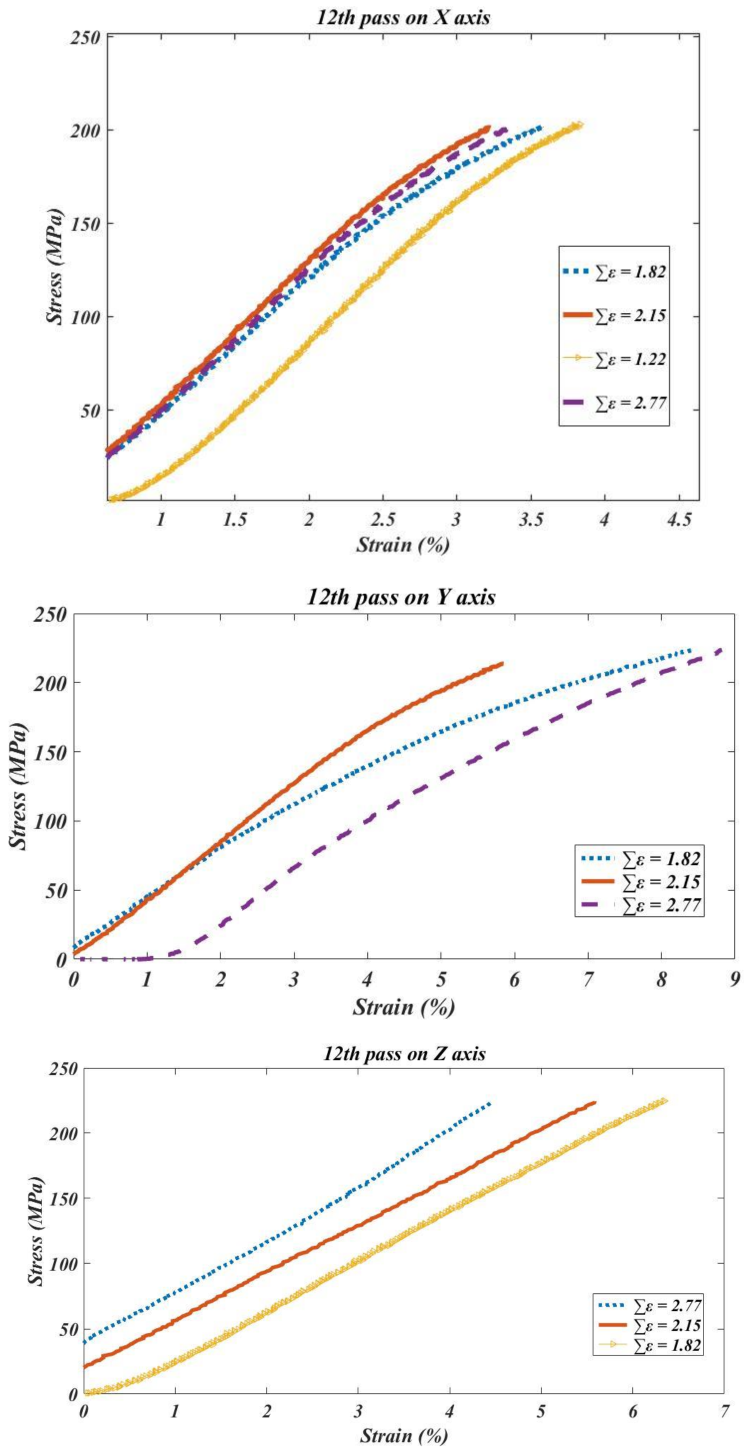

Figure B.5 Stress-strain curves in three dimensions during 12th pass: (a) stress-strain curve on X axis; (b) stress-strain curve on Y axis; (c) stress-strain curve on Y axis.

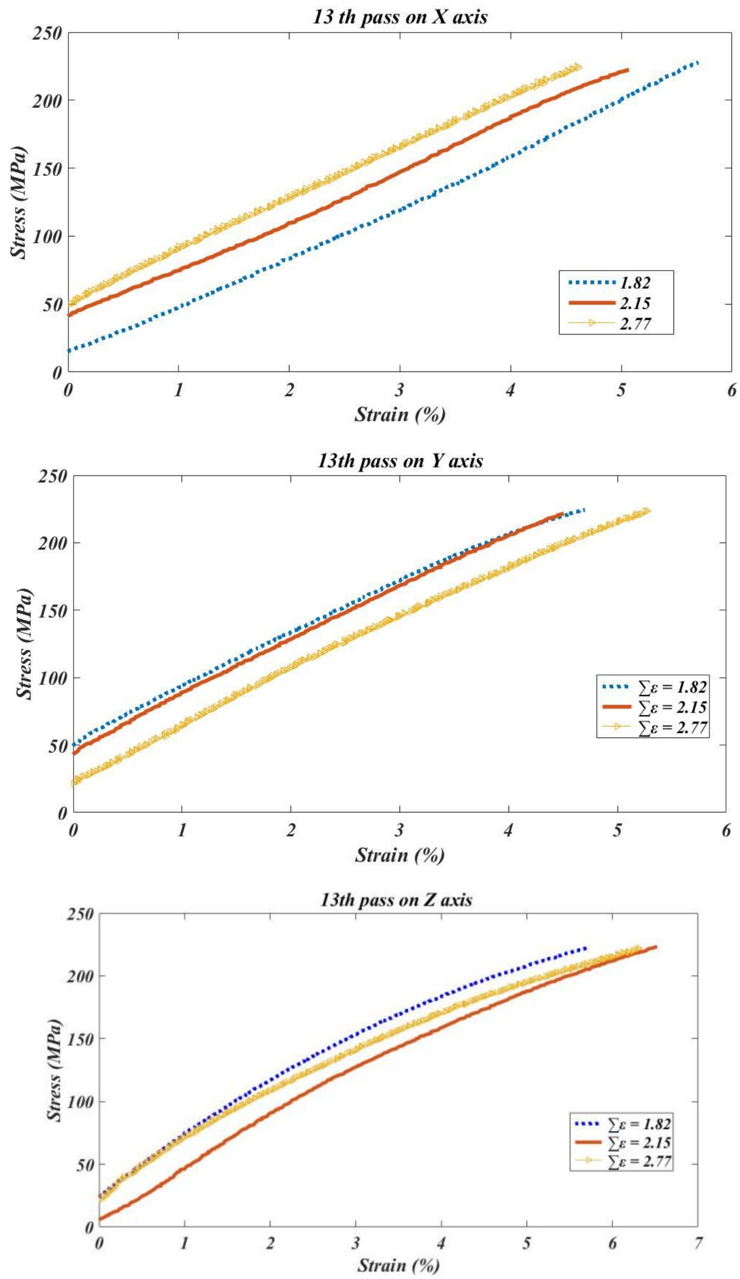

Figure B.6 Stress-strain curves in three dimensions during 13th pass: (a) stress-strain curve on X axis; (b) stress-strain curve on Y axis; (c) stress-strain curve on Y axis

Appendix C

Dynamic Compression Test Calculations

	A	B	C	D	E	F	G	H	I	J	K	L	M	N	O	P
1	Time	Inst	Trans	Inst	Tr	Refe	Trans	Transimitted S	Stress	Reflected s	Strain Rate	Integration	Strain	Stress	T strain	T stress
2	0	0.0480	-0.0480	0.0000	0.0000	-0.0720	0.0000	0	0	-9.2E-05	-149.386	0	0	0	0	0
3	0.4	0.0480	-0.0480	0.0000	0.0000	-0.0720	0.0000	0	0	-9.2E-05	-149.386	-3.6746E-05	-6E-05	0	-6E-05	0
4	0.8	0.0480	-0.0480	0.0000	0.0000	-0.0640	-0.0080	1.02073E-05	41.9985	-8.2E-05	-132.788	-7.1451E-05	-0.00012	41.9985	-0.00012	41.99362
5	1.2	0.0480	-0.0400	0.0000	0.0080	-0.0640	-0.0080	1.02073E-05	41.9985	-8.2E-05	-132.788	-0.00010411	-0.00017	41.9985	-0.00017	41.99139
6	1.6	0.0480	-0.0400	0.0000	0.0080	-0.0640	-0.0080	1.02073E-05	41.9985	-8.2E-05	-132.788	-0.00013678	-0.00022	41.9985	-0.00022	41.98916
7	2	0.0480	-0.0480	0.0000	0.0000	-0.0640	-0.0080	1.02073E-05	41.9985	-8.2E-05	-132.788	-0.00016944	-0.00028	41.9985	-0.00028	41.98693
8	2.4	0.0480	-0.0480	0.0000	0.0000	-0.0640	-0.0080	1.02073E-05	41.9985	-8.2E-05	-132.788	-0.00020211	-0.00033	41.9985	-0.00033	41.9847
9	2.8	0.0480	-0.0480	0.0000	0.0000	-0.0640	-0.0080	1.02073E-05	41.9985	-8.2E-05	-132.788	-0.00023477	-0.00038	41.9985	-0.00038	41.98247
10	3.2	0.0480	-0.0480	0.0000	0.0000	-0.0560	-0.0160	2.04147E-05	83.99701	-7.1E-05	-116.189	-0.00026539	-0.00043	83.99701	-0.00043	83.96076
11	3.6	0.0480	-0.0400	0.0000	0.0080	-0.0560	-0.0160	2.04147E-05	83.99701	-7.1E-05	-116.189	-0.00029397	-0.00048	83.99701	-0.00048	83.95685
12	4	0.0480	-0.0400	0.0000	0.0080	-0.0480	-0.0160	2.04147E-05	83.99701	-6.1E-05	-99.5907	-0.00032051	-0.00052	83.99701	-0.00052	83.95323
13	4.4	0.0480	-0.0480	0.0000	0.0000	-0.0480	-0.0160	2.04147E-05	83.99701	-6.1E-05	-99.5907	-0.00034501	-0.00056	83.99701	-0.00056	83.94988
14	4.8	0.0480	-0.0480	0.0000	0.0000	-0.0640	-0.0240	3.0622E-05	125.9955	-8.2E-05	-132.788	-0.00037359	-0.00061	125.9955	-0.00061	125.919
15	5.2	0.0480	-0.0400	0.0000	0.0080	-0.0640	-0.0240	3.0622E-05	125.9955	-8.2E-05	-132.788	-0.00040625	-0.00066	125.9955	-0.00066	125.9123
16	5.6	0.0480	-0.0400	0.0000	0.0080	-0.0640	-0.0240	3.0622E-05	125.9955	-8.2E-05	-132.788	-0.00043892	-0.00071	125.9955	-0.00071	125.9056
17	6	0.0480	-0.0400	0.0000	0.0080	-0.0640	-0.0240	3.0622E-05	125.9955	-8.2E-05	-132.788	-0.00047158	-0.00077	125.9955	-0.00077	125.8989
18	6.4	0.0480	-0.0400	0.0000	0.0080	-0.0640	-0.0240	3.0622E-05	125.9955	-8.2E-05	-132.788	-0.00050424	-0.00082	125.9955	-0.00082	125.8922
19	6.8	0.0480	-0.0480	0.0000	0.0000	-0.0640	-0.0240	3.0622E-05	125.9955	-8.2E-05	-132.788	-0.00053691	-0.00087	125.9955	-0.00087	125.8855
20	7.2	0.0480	-0.0480	0.0000	0.0000	-0.0640	-0.0240	3.0622E-05	125.9955	-8.2E-05	-132.788	-0.00056957	-0.00093	125.9955	-0.00093	125.8788
21	7.6	0.0480	-0.0400	0.0000	0.0080	-0.0640	-0.0240	3.0622E-05	125.9955	-8.2E-05	-132.788	-0.00060223	-0.00098	125.9955	-0.00098	125.8721
22	8	0.0480	-0.0400	0.0000	0.0080	-0.0560	-0.0320	4.08293E-05	167.994	-7.1E-05	-116.189	-0.00063285	-0.00103	167.994	-0.00103	167.8211
23	8.4	0.0480	-0.0480	0.0000	0.0000	-0.0560	-0.0320	4.08293E-05	167.994	-7.1E-05	-116.189	-0.00066144	-0.00108	167.994	-0.00108	167.8133
24	8.8	0.0480	-0.0480	0.0000	0.0000	-0.0480	-0.0320	4.08293E-05	167.994	-6.1E-05	-99.5907	-0.00068797	-0.00112	167.994	-0.00112	167.8061
25	9.2	0.0480	-0.0480	0.0000	0.0000	-0.0480	-0.0320	4.08293E-05	167.994	-6.1E-05	-99.5907	-0.00071247	-0.00116	167.994	-0.00116	167.7994
26	9.6	0.0480	-0.0480	0.0000	0.0000	-0.0240	-0.0320	4.08293E-05	167.994	-3.1E-05	-49.7953	-0.00073085	-0.00119	167.994	-0.00119	167.7944
27	10	0.0480	-0.0400	0.0000	0.0080	-0.0240	-0.0320	4.08293E-05	167.994	-3.1E-05	-49.7953	-0.00074309	-0.00121	167.994	-0.00121	167.791
28	10.4	0.0480	-0.0400	0.0000	0.0080	0.0080	-0.0320	4.08293E-05	167.994	1.02E-05	16.59845	-0.00074718	-0.00122	167.994	-0.00122	167.7899
29	10.8	0.0480	-0.0400	0.0000	0.0080	0.0080	-0.0320	4.08293E-05	167.994	1.02E-05	16.59845	-0.00074309	-0.00121	167.994	-0.00121	167.791
30	11.2	0.0480	-0.0400	0.0000	0.0080	0.0800	-0.0400	5.10367E-05	209.9925	0.000102	165.9845	-0.00072064	-0.00117	209.9925	-0.00117	209.7464
31	11.6	0.0400	-0.0480	-0.0080	0.0000	0.0800	-0.0400	5.10367E-05	209.9925	0.000102	165.9845	-0.00067981	-0.00111	209.9925	-0.00111	209.7604
32	12	0.0400	-0.0480	-0.0080	0.0000	0.1200	-0.0400	5.10367E-05	209.9925	0.000153	248.9767	-0.00062877	-0.00102	209.9925	-0.00102	209.7778
33	12.4	0.0480	-0.0400	0.0000	0.0080	0.1200	-0.0400	5.10367E-05	209.9925	0.000153	248.9767	-0.00056753	-0.00092	209.9925	-0.00092	209.7987
34	12.8	0.0480	-0.0400	0.0000	0.0080	0.1760	-0.0480	6.1244E-05	251.991	0.000225	365.1658	-0.00049199	-0.0008	251.991	-0.0008	251.7894
35	13.2	0.0480	-0.0480	0.0000	0.0000	0.1760	-0.0480	6.1244E-05	251.991	0.000225	365.1658	-0.00040217	-0.00065	251.991	-0.00065	251.8262
36	13.6	0.0480	-0.0480	0.0000	0.0000	0.2160	-0.0400	5.10367E-05	209.9925	0.000276	448.158	-0.00030214	-0.00049	209.9925	-0.00049	209.8893
37	14	0.0480	-0.0480	0.0000	0.0000	0.2160	-0.0400	5.10367E-05	209.9925	0.000276	448.158	-0.0001919	-0.00031	209.9925	-0.00031	209.927
38	14.4	0.0480	-0.0480	0.0000	0.0000	0.2640	-0.0320	4.08293E-05	167.994	0.000337	547.7487	-6.941E-05	-0.00011	167.994	-0.00011	167.975
39	14.8	0.0480	-0.0480	0.0000	0.0000	0.2640	-0.0320	4.08293E-05	167.994	0.000337	547.7487	6.5327E-05	0.000106	167.994	0.000106	168.0119
40	15.2	0.0480	-0.0480	0.0000	0.0000	0.2960	-0.0400	5.10367E-05	209.9925	0.000378	614.1425	0.00020823	0.000339	209.9925	0.000339	210.0636
41	15.6	0.0480	-0.0400	0.0000	0.0080	0.2960	-0.0400	5.10367E-05	209.9925	0.000378	614.1425	0.000359298	0.000584	209.9925	0.000584	210.1152
42	16	0.0480	-0.0400	0.0000	0.0080	0.3040	-0.0480	6.1244E-05	251.991	0.000388	630.741	0.000512408	0.000833	251.991	0.000833	252.201
43	16.4	0.0480	-0.0400	0.0000	0.0080	0.3040	-0.0480	6.1244E-05	251.991	0.000388	630.741	0.00066756	0.001086	251.991	0.001085	252.2646
44	16.8	0.0480	-0.0400	0.0000	0.0080	0.3200	-0.0480	6.1244E-05	251.991	0.000408	663.9379	0.000826794	0.001344	251.991	0.001344	252.3298
45	17.2	0.0480	-0.0400	0.0000	0.0080	0.3200	-0.0480	6.1244E-05	251.991	0.000408	663.9379	0.000990112	0.00161	251.991	0.001609	252.3967
46	17.6	0.0480	-0.0400	0.0000	0.0080	0.3280	-0.0480	6.1244E-05	251.991	0.000419	680.5363	0.00115547	0.001879	251.991	0.001877	252.4645
47	18	0.0480	-0.0480	0.0000	0.0000	0.3280	-0.0480	6.1244E-05	251.991	0.000419	680.5363	0.001322871	0.002151	251.991	0.002149	252.5331

Figure C.1 Derivations of equations (2.6) to (2.18) to obtain strain rate, true stress and true strain, $\sum\varepsilon = 1.82$ on x-axis

49	18.8	0.0480	-0.0480	0.0000	0.0000	0.3360	-0.0480	6.1244E-05	251.991	0.000429	697.1347	0.001663796	0.002706	251.991	0.002702	252.6728
50	19.2	0.0480	-0.0480	0.0000	0.0000	0.3360	-0.0480	6.1244E-05	251.991	0.000429	697.1347	0.001835279	0.002984	251.991	0.00298	252.7431
51	19.6	0.0480	-0.0480	0.0000	0.0000	0.3360	-0.0480	6.1244E-05	251.991	0.000429	697.1347	0.002006762	0.003263	251.991	0.003258	252.8133
52	20	0.0480	-0.0480	0.0000	0.0000	0.3520	-0.0480	6.1244E-05	251.991	0.000449	730.3316	0.002182329	0.003549	251.991	0.003542	252.8853
53	20.4	0.0480	-0.0480	0.0000	0.0000	0.3520	-0.0480	6.1244E-05	251.991	0.000449	730.3316	0.002361978	0.003841	251.991	0.003834	252.9589
54	20.8	0.0480	-0.0480	0.0000	0.0000	0.3600	-0.0480	6.1244E-05	251.991	0.000459	746.9301	0.002543668	0.004136	251.991	0.004128	253.0333
55	21.2	0.0480	-0.0400	0.0000	0.0080	0.3600	-0.0480	6.1244E-05	251.991	0.000459	746.9301	0.0027274	0.004435	251.991	0.004425	253.1086
56	21.6	0.0480	-0.0400	0.0000	0.0080	0.3680	-0.0480	6.1244E-05	251.991	0.00047	763.5285	0.002913174	0.004737	251.991	0.004726	253.1847
57	22	0.0480	-0.0400	0.0000	0.0080	0.3680	-0.0480	6.1244E-05	251.991	0.00047	763.5285	0.003100989	0.005043	251.991	0.00503	253.2617
58	22.4	0.0480	-0.0400	0.0000	0.0080	0.3840	-0.0480	6.1244E-05	251.991	0.00049	796.7254	0.003292887	0.005355	251.991	0.00534	253.3403
59	22.8	0.0480	-0.0480	0.0000	0.0000	0.3840	-0.0480	6.1244E-05	251.991	0.00049	796.7254	0.003488868	0.005673	251.991	0.005657	253.4206
60	23.2	0.0480	-0.0480	0.0000	0.0000	0.3840	-0.0560	7.14514E-05	293.9895	0.00049	796.7254	0.003684848	0.005992	293.9895	0.005974	295.7511
61	23.6	0.0480	-0.0400	0.0000	0.0080	0.3840	-0.0560	7.14514E-05	293.9895	0.00049	796.7254	0.003880829	0.006311	293.9895	0.006291	295.8448
62	24	0.0480	-0.0400	0.0000	0.0080	0.3840	-0.0480	6.1244E-05	251.991	0.00049	796.7254	0.00407681	0.006629	251.991	0.006608	253.6616
63	24.4	0.0480	-0.0400	0.0000	0.0080	0.3840	-0.0480	6.1244E-05	251.991	0.00049	796.7254	0.004272791	0.006948	251.991	0.006924	253.7419
64	24.8	0.0480	-0.0400	0.0000	0.0080	0.3840	-0.0560	7.14514E-05	293.9895	0.00049	796.7254	0.004468772	0.007267	293.9895	0.007241	296.1259
65	25.2	0.0480	-0.0480	0.0000	0.0000	0.3840	-0.0560	7.14514E-05	293.9895	0.00049	796.7254	0.004664753	0.007585	293.9895	0.007557	296.2196
66	25.6	0.0480	-0.0480	0.0000	0.0000	0.4000	-0.0560	7.14514E-05	293.9895	0.00051	829.9223	0.004864817	0.007911	293.9895	0.00788	296.3152
67	26	0.0480	-0.0400	0.0000	0.0080	0.4000	-0.0560	7.14514E-05	293.9895	0.00051	829.9223	0.005068963	0.008243	293.9895	0.008209	296.4128
68	26.4	0.0480	-0.0400	0.0000	0.0080	0.4080	-0.0560	7.14514E-05	293.9895	0.000521	846.5208	0.005275152	0.008578	293.9895	0.008541	296.5114
69	26.8	0.0480	-0.0480	0.0000	0.0000	0.4080	-0.0560	7.14514E-05	293.9895	0.000521	846.5208	0.005483381	0.008917	293.9895	0.008877	296.6109
70	27.2	0.0480	-0.0480	0.0000	0.0000	0.4160	-0.0560	7.14514E-05	293.9895	0.000531	863.1192	0.005693652	0.009259	293.9895	0.009216	296.7115
71	27.6	0.0480	-0.0400	0.0000	0.0080	0.4160	-0.0560	7.14514E-05	293.9895	0.000531	863.1192	0.005905965	0.009604	293.9895	0.009558	296.813
72	28	0.0480	-0.0400	0.0000	0.0080	0.4080	-0.0560	7.14514E-05	293.9895	0.000521	846.5208	0.006116236	0.009946	293.9895	0.009897	296.9135
73	28.4	0.0480	-0.0400	0.0000	0.0080	0.4080	-0.0560	7.14514E-05	293.9895	0.000521	846.5208	0.006324466	0.010284	293.9895	0.010232	297.013
74	28.8	0.0480	-0.0400	0.0000	0.0080	0.4160	-0.0560	7.14514E-05	293.9895	0.000531	863.1192	0.006534737	0.010626	293.9895	0.01057	297.1135
75	29.2	0.0480	-0.0480	0.0000	0.0000	0.4160	-0.0560	7.14514E-05	293.9895	0.000531	863.1192	0.006747049	0.010972	293.9895	0.010912	297.215
76	29.6	0.0480	-0.0480	0.0000	0.0000	0.4080	-0.0560	7.14514E-05	293.9895	0.000521	846.5208	0.006957321	0.011314	293.9895	0.01125	297.3156
77	30	0.0480	-0.0400	0.0000	0.0080	0.4080	-0.0560	7.14514E-05	293.9895	0.000521	846.5208	0.00716555	0.011652	293.9895	0.011585	297.4151
78	30.4	0.0480	-0.0400	0.0000	0.0080	0.4080	-0.0560	7.14514E-05	293.9895	0.000521	846.5208	0.00737378	0.011991	293.9895	0.011919	297.5147
79	30.8	0.0560	-0.0400	0.0080	0.0080	0.4080	-0.0560	7.14514E-05	293.9895	0.000521	846.5208	0.00758201	0.012329	293.9895	0.012254	297.6142
80	31.2	0.0560	-0.0400	0.0080	0.0080	0.4000	-0.0560	7.14514E-05	293.9895	0.00051	829.9223	0.007788198	0.012665	293.9895	0.012585	297.7128
81	31.6	0.0480	-0.0400	0.0000	0.0080	0.4000	-0.0560	7.14514E-05	293.9895	0.00051	829.9223	0.007992344	0.012997	293.9895	0.012913	297.8104
82	32	0.0480	-0.0400	0.0000	0.0080	0.4000	-0.0560	7.14514E-05	293.9895	0.00051	829.9223	0.008196491	0.013329	293.9895	0.013241	297.908
83	32.4	0.0480	-0.0480	0.0000	0.0000	0.4000	-0.0560	7.14514E-05	293.9895	0.00051	829.9223	0.008400638	0.013661	293.9895	0.013568	298.0056
84	32.8	0.0480	-0.0480	0.0000	0.0000	0.4080	-0.0640	8.16587E-05	335.988	0.000521	846.5208	0.008606826	0.013996	335.988	0.013899	340.6904
85	33.2	0.0480	-0.0400	0.0000	0.0080	0.4080	-0.0640	8.16587E-05	335.988	0.000521	846.5208	0.008815056	0.014334	335.988	0.014233	340.8042
86	33.6	0.0480	-0.0400	0.0000	0.0080	0.4080	-0.0560	7.14514E-05	293.9895	0.000521	846.5208	0.009023285	0.014673	293.9895	0.014566	298.3032
87	34	0.0480	-0.0480	0.0000	0.0000	0.4080	-0.0560	7.14514E-05	293.9895	0.000521	846.5208	0.009231515	0.015012	293.9895	0.0149	298.4028
88	34.4	0.0480	-0.0480	0.0000	0.0000	0.4000	-0.0560	7.14514E-05	293.9895	0.00051	829.9223	0.009437703	0.015347	293.9895	0.01523	298.5014
89	34.8	0.0480	-0.0480	0.0000	0.0000	0.4000	-0.0560	7.14514E-05	293.9895	0.00051	829.9223	0.00964185	0.015679	293.9895	0.015557	298.5989
90	35.2	0.0480	-0.0480	0.0000	0.0000	0.3920	-0.0720	9.1866E-05	377.9865	0.0005	813.3239	0.009843955	0.016008	377.9865	0.015881	384.0372
91	35.6	0.0480	-0.0400	0.0000	0.0080	0.3920	-0.0720	9.1866E-05	377.9865	0.0005	813.3239	0.010044019	0.016333	377.9865	0.016201	384.1601
92	36	0.0480	-0.0400	0.0000	0.0080	0.4000	-0.0640	8.16587E-05	335.988	0.00051	829.9223	0.010246124	0.016662	335.988	0.016524	341.5861

Figure C.1 Derivations of equations (2.6) to (2.18) to obtain strain rate, true stress and true strain, $\sum\varepsilon = 1.82$ on x-axis, Continued

92	36	0.0480	-0.0400	0.0000	0.0080	0.4000	-0.0640	8.16587E-05	335.988	0.00051	829.9223	0.010246124	0.016662	335.988	0.016524	341.5861
93	36.4	0.0480	-0.0400	0.0000	0.0080	0.4000	-0.0640	8.16587E-05	335.988	0.00051	829.9223	0.010450271	0.016993	335.988	0.016851	341.6976
94	36.8	0.0480	-0.0400	0.0000	0.0080	0.4000	-0.0720	9.1866E-05	377.9865	0.00051	829.9223	0.010654418	0.017325	377.9865	0.017177	384.5353
95	37.2	0.0480	-0.0400	0.0000	0.0080	0.4000	-0.0720	9.1866E-05	377.9865	0.00051	829.9223	0.010858565	0.017657	377.9865	0.017503	384.6608
96	37.6	0.0480	-0.0400	0.0000	0.0080	0.4000	-0.0640	8.16587E-05	335.988	0.00051	829.9223	0.011062711	0.017989	335.988	0.01783	342.0322
97	38	0.0480	-0.0400	0.0000	0.0080	0.4000	-0.0640	8.16587E-05	335.988	0.00051	829.9223	0.011266858	0.018321	335.988	0.018156	342.1438
98	38.4	0.0480	-0.0400	0.0000	0.0080	0.4000	-0.0560	7.14514E-05	293.9895	0.00051	829.9223	0.011471005	0.018653	293.9895	0.018481	299.4734
99	38.8	0.0480	-0.0400	0.0000	0.0080	0.4000	-0.0560	7.14514E-05	293.9895	0.00051	829.9223	0.011675152	0.018985	293.9895	0.018807	299.571
100	39.2	0.0480	-0.0400	0.0000	0.0080	0.4000	-0.0640	8.16587E-05	335.988	0.00051	829.9223	0.011879298	0.019317	335.988	0.019133	342.4784
101	39.6	0.0480	-0.0400	0.0000	0.0080	0.4000	-0.0640	8.16587E-05	335.988	0.00051	829.9223	0.012083445	0.019649	335.988	0.019459	342.5899
102	40	0.0480	-0.0400	0.0000	0.0080	0.4080	-0.0720	9.1866E-05	377.9865	0.000521	846.5208	0.012289633	0.019985	377.9865	0.019787	385.5404
103	40.4	0.0480	-0.0400	0.0000	0.0080	0.4080	-0.0720	9.1866E-05	377.9865	0.000521	846.5208	0.012497863	0.020323	377.9865	0.020119	385.6684
104	40.8	0.0480	-0.0400	0.0000	0.0080	0.4240	-0.0560	7.14514E-05	293.9895	0.000541	879.7177	0.012710175	0.020668	293.9895	0.020458	300.0658
105	41.2	0.0480	-0.0400	0.0000	0.0080	0.4240	-0.0560	7.14514E-05	293.9895	0.000541	879.7177	0.012926571	0.02102	293.9895	0.020802	300.1693
106	41.6	0.0480	-0.0400	0.0000	0.0080	0.4320	-0.0640	8.16587E-05	335.988	0.000551	896.3161	0.013145008	0.021375	335.988	0.02115	343.1699
107	42	0.0480	-0.0400	0.0000	0.0080	0.4320	-0.0640	8.16587E-05	335.988	0.000551	896.3161	0.013365486	0.021734	335.988	0.021501	343.2904
108	42.4	0.0480	-0.0400	0.0000	0.0080	0.4400	-0.0720	9.1866E-05	377.9865	0.000561	912.9145	0.013588006	0.022096	377.9865	0.021855	386.3385
109	42.8	0.0480	-0.0400	0.0000	0.0080	0.4400	-0.0720	9.1866E-05	377.9865	0.000561	912.9145	0.013812568	0.022461	377.9865	0.022212	386.4765
110	43.2	0.0480	-0.0400	0.0000	0.0080	0.4480	-0.0720	9.1866E-05	377.9865	0.000572	929.513	0.014039171	0.02283	377.9865	0.022573	386.6158
111	43.6	0.0480	-0.0480	0.0000	0.0000	0.4480	-0.0720	9.1866E-05	377.9865	0.000572	929.513	0.014267815	0.023201	377.9865	0.022936	386.7563
112	44	0.0480	-0.0480	0.0000	0.0000	0.4560	-0.0640	8.16587E-05	335.988	0.000582	946.1114	0.014498501	0.023576	335.988	0.023303	343.9094
113	44.4	0.0480	-0.0480	0.0000	0.0000	0.4560	-0.0640	8.16587E-05	335.988	0.000582	946.1114	0.014731228	0.023955	335.988	0.023672	344.0366
114	44.8	0.0480	-0.0480	0.0000	0.0000	0.4720	-0.0640	8.16587E-05	335.988	0.000602	979.3083	0.014968038	0.02434	335.988	0.024048	344.166
115	45.2	0.0480	-0.0480	0.0000	0.0000	0.4720	-0.0640	8.16587E-05	335.988	0.000602	979.3083	0.015208931	0.024732	335.988	0.024431	344.2976
116	45.6	0.0480	-0.0480	0.0000	0.0000	0.4640	-0.0800	0.000102073	419.985	0.000592	962.7099	0.015447783	0.02512	419.985	0.02481	430.5351
117	46	0.0480	-0.0400	0.0000	0.0080	0.4640	-0.0800	0.000102073	419.985	0.000592	962.7099	0.015684593	0.025505	419.985	0.025185	430.6968
118	46.4	0.0480	-0.0400	0.0000	0.0080	0.4800	-0.0800	0.000102073	419.985	0.000612	995.9068	0.015925486	0.025897	419.985	0.025567	430.8613
119	46.8	0.0480	-0.0480	0.0000	0.0000	0.4800	-0.0800	0.000102073	419.985	0.000612	995.9068	0.016170463	0.026295	419.985	0.025955	431.0286
120	47.2	0.0480	-0.0480	0.0000	0.0000	0.4800	-0.0800	0.000102073	419.985	0.000612	995.9068	0.016415439	0.026694	419.985	0.026344	431.1959
121	47.6	0.0480	-0.0400	0.0000	0.0080	0.4800	-0.0800	0.000102073	419.985	0.000612	995.9068	0.016660415	0.027092	419.985	0.026731	431.3633
122	48	0.0480	-0.0400	0.0000	0.0080	0.4800	-0.0720	9.1866E-05	377.9865	0.000612	995.9068	0.016905391	0.02749	377.9865	0.027119	388.3775
123	48.4	0.0480	-0.0400	0.0000	0.0080	0.4800	-0.0720	9.1866E-05	377.9865	0.000612	995.9068	0.017150367	0.027889	377.9865	0.027507	388.5281
124	48.8	0.0480	-0.0400	0.0000	0.0080	0.4800	-0.0800	0.000102073	419.985	0.000612	995.9068	0.017395343	0.028287	419.985	0.027894	431.8652
125	49.2	0.0480	-0.0400	0.0000	0.0080	0.4800	-0.0800	0.000102073	419.985	0.000612	995.9068	0.017640319	0.028685	419.985	0.028282	432.0325
126	49.6	0.0480	-0.0400	0.0000	0.0080	0.4880	-0.0800	0.000102073	419.985	0.000623	1012.505	0.017887337	0.029087	419.985	0.028672	432.2012
127	50	0.0480	-0.0480	0.0000	0.0000	0.4880	-0.0800	0.000102073	419.985	0.000623	1012.505	0.018136396	0.029492	419.985	0.029066	432.3713
128	50.4	0.0480	-0.0480	0.0000	0.0000	0.4880	-0.0720	9.1866E-05	377.9865	0.000623	1012.505	0.018385455	0.029897	377.9865	0.029459	389.2872
129	50.8	0.0480	-0.0480	0.0000	0.0000	0.4880	-0.0720	9.1866E-05	377.9865	0.000623	1012.505	0.018634514	0.030302	377.9865	0.029852	389.4403
130	51.2	0.0480	-0.0480	0.0000	0.0000	0.4960	-0.0640	8.16587E-05	335.988	0.000633	1029.104	0.018885614	0.03071	335.988	0.030248	346.3064
131	51.6	0.0480	-0.0400	0.0000	0.0080	0.4960	-0.0640	8.16587E-05	335.988	0.000633	1029.104	0.019138756	0.031122	335.988	0.030648	346.4447
132	52	0.0480	-0.0400	0.0000	0.0080	0.4960	-0.0720	9.1866E-05	377.9865	0.000633	1029.104	0.019391898	0.031534	377.9865	0.031047	389.9058
133	52.4	0.0480	-0.0480	0.0000	0.0000	0.4960	-0.0720	9.1866E-05	377.9865	0.000633	1029.104	0.01964504	0.031945	377.9865	0.031446	390.0614
134	52.8	0.0480	-0.0480	0.0000	0.0000	0.5040	-0.0720	9.1866E-05	377.9865	0.000643	1045.702	0.019900223	0.03236	377.9865	0.031848	390.2183
135	53.2	0.0480	-0.0400	0.0000	0.0080	0.5040	-0.0720	9.1866E-05	377.9865	0.000643	1045.702	0.020157448	0.032779	377.9865	0.032253	390.3764
136	53.6	0.0480	-0.0400	0.0000	0.0080	0.5120	-0.0720	9.1866E-05	377.9865	0.000653	1062.301	0.020416715	0.0332	377.9865	0.032661	390.5358
137	54	0.0480	-0.0480	0.0000	0.0000	0.5120	-0.0720	9.1866E-05	377.9865	0.000653	1062.301	0.020678022	0.033625	377.9865	0.033072	390.6964

Figure C.1 Derivations of equations (2.6) to (2.18) to obtain strain rate, true stress and true strain, $\sum\varepsilon = 1.82$ on x-axis, Continued

138	54.4	0.0480	-0.0480	0.0000	0.0000	0.5040	-0.0720	9.1866E-05	377.9865	0.000643	1045.702	0.020937289	0.034047	377.9865	0.03348	390.8557
139	54.8	0.0480	-0.0400	0.0000	0.0080	0.5040	-0.0720	9.1866E-05	377.9865	0.000643	1045.702	0.021194514	0.034465	377.9865	0.033884	391.0138
140	55.2	0.0480	-0.0400	0.0000	0.0080	0.5120	-0.0800	0.000102073	419.985	0.000653	1062.301	0.02145378	0.034887	419.985	0.034292	434.6369
141	55.6	0.0480	-0.0400	0.0000	0.0080	0.5120	-0.0800	0.000102073	419.985	0.000653	1062.301	0.021715088	0.035312	419.985	0.034702	434.8153
142	56	0.0480	-0.0400	0.0000	0.0080	0.5120	-0.0800	0.000102073	419.985	0.000653	1062.301	0.021976396	0.035736	419.985	0.035113	434.9938
143	56.4	0.0480	-0.0480	0.0000	0.0000	0.5120	-0.0800	0.000102073	419.985	0.000653	1062.301	0.022237703	0.036161	419.985	0.035523	435.1723
144	56.8	0.0480	-0.0480	0.0000	0.0000	0.5200	-0.0800	0.000102073	419.985	0.000663	1078.899	0.022501053	0.03659	419.985	0.035936	435.3521
145	57.2	0.0400	-0.0480	-0.0080	0.0000	0.5200	-0.0800	0.000102073	419.985	0.000663	1078.899	0.022766443	0.037021	419.985	0.036352	435.5334
146	57.6	0.0400	-0.0480	-0.0080	0.0000	0.5120	-0.0800	0.000102073	419.985	0.000653	1062.301	0.023029793	0.037449	419.985	0.036765	435.7132
147	58	0.0480	-0.0480	0.0000	0.0000	0.5120	-0.0800	0.000102073	419.985	0.000653	1062.301	0.0232911	0.037874	419.985	0.037175	435.8917
148	58.4	0.0480	-0.0480	0.0000	0.0000	0.5120	-0.0800	0.000102073	419.985	0.000653	1062.301	0.023552408	0.038299	419.985	0.037584	436.0701
149	58.8	0.0480	-0.0480	0.0000	0.0000	0.5120	-0.0800	0.000102073	419.985	0.000653	1062.301	0.023813716	0.038724	419.985	0.037993	436.2486
150	59.2	0.0480	-0.0480	0.0000	0.0000	0.5040	-0.0800	0.000102073	419.985	0.000643	1045.702	0.024072982	0.039146	419.985	0.038399	436.4257
151	59.6	0.0480	-0.0400	0.0000	0.0080	0.5040	-0.0800	0.000102073	419.985	0.000643	1045.702	0.024330207	0.039564	419.985	0.038801	436.6013
152	60	0.0480	-0.0400	0.0000	0.0080	0.5120	-0.0800	0.000102073	419.985	0.000653	1062.301	0.024589474	0.039986	419.985	0.039207	436.7784
153	60.4	0.0480	-0.0480	0.0000	0.0000	0.5120	-0.0800	0.000102073	419.985	0.000653	1062.301	0.024850781	0.040411	419.985	0.039615	436.9569
154	60.8	0.0480	-0.0480	0.0000	0.0000	0.5120	-0.0800	0.000102073	419.985	0.000653	1062.301	0.025112089	0.040835	419.985	0.040024	437.1353
155	61.2	0.0480	-0.0400	0.0000	0.0080	0.5120	-0.0800	0.000102073	419.985	0.000653	1062.301	0.025373397	0.04126	419.985	0.040432	437.3138
156	61.6	0.0480	-0.0400	0.0000	0.0080	0.5200	-0.0800	0.000102073	419.985	0.000663	1078.899	0.025636746	0.041689	419.985	0.040843	437.4936
157	62	0.0480	-0.0400	0.0000	0.0080	0.5200	-0.0800	0.000102073	419.985	0.000663	1078.899	0.025902137	0.04212	419.985	0.041257	437.6749
158	62.4	0.0480	-0.0400	0.0000	0.0080	0.5200	-0.0800	0.000102073	419.985	0.000663	1078.899	0.026167528	0.042552	419.985	0.041671	437.8561
159	62.8	0.0480	-0.0400	0.0000	0.0080	0.5200	-0.0800	0.000102073	419.985	0.000663	1078.899	0.026432919	0.042983	419.985	0.042085	438.0374
160	63.2	0.0480	-0.0400	0.0000	0.0080	0.5280	-0.0800	0.000102073	419.985	0.000674	1095.497	0.026700351	0.043418	419.985	0.042502	438.22
161	63.6	0.0480	-0.0480	0.0000	0.0000	0.5280	-0.0800	0.000102073	419.985	0.000674	1095.497	0.026969825	0.043856	419.985	0.042922	438.4041
162	64	0.0480	-0.0480	0.0000	0.0000	0.5360	-0.0800	0.000102073	419.985	0.000684	1112.096	0.02724134	0.044298	419.985	0.043345	438.5895
163	64.4	0.0480	-0.0400	0.0000	0.0080	0.5360	-0.0800	0.000102073	419.985	0.000684	1112.096	0.027514896	0.044743	419.985	0.043771	438.7763
164	64.8	0.0480	-0.0400	0.0000	0.0080	0.5440	-0.0800	0.000102073	419.985	0.000694	1128.694	0.027790494	0.045191	419.985	0.0442	438.9645
165	65.2	0.0480	-0.0480	0.0000	0.0000	0.5440	-0.0800	0.000102073	419.985	0.000694	1128.694	0.028068134	0.045642	419.985	0.044631	439.1542
166	65.6	0.0480	-0.0480	0.0000	0.0000	0.5520	-0.0800	0.000102073	419.985	0.000704	1145.293	0.028347815	0.046097	419.985	0.045066	439.3452
167	66	0.0480	-0.0400	0.0000	0.0080	0.5520	-0.0800	0.000102073	419.985	0.000704	1145.293	0.028629537	0.046555	419.985	0.045504	439.5376
168	66.4	0.0480	-0.0400	0.0000	0.0080	0.5520	-0.0800	0.000102073	419.985	0.000704	1145.293	0.02891126	0.047013	419.985	0.045942	439.73
169	66.8	0.0480	-0.0400	0.0000	0.0080	0.5520	-0.0800	0.000102073	419.985	0.000704	1145.293	0.029192982	0.047472	419.985	0.046379	439.9224
170	67.2	0.0480	-0.0400	0.0000	0.0080	0.5520	-0.0800	0.000102073	419.985	0.000704	1145.293	0.029474705	0.04793	419.985	0.046816	440.1148
171	67.6	0.0480	-0.0480	0.0000	0.0000	0.5520	-0.0800	0.000102073	419.985	0.000704	1145.293	0.029756427	0.048388	419.985	0.047254	440.3072
172	68	0.0480	-0.0480	0.0000	0.0000	0.5680	-0.0800	0.000102073	419.985	0.000725	1178.49	0.030042233	0.048853	419.985	0.047697	440.5024
173	68.4	0.0480	-0.0400	0.0000	0.0080	0.5680	-0.0800	0.000102073	419.985	0.000725	1178.49	0.030332121	0.049324	419.985	0.048146	440.7003
174	68.8	0.0480	-0.0400	0.0000	0.0080	0.5520	-0.0800	0.000102073	419.985	0.000704	1145.293	0.030617927	0.049789	419.985	0.048589	440.8955
175	69.2	0.0480	-0.0400	0.0000	0.0080	0.5520	-0.0800	0.000102073	419.985	0.000704	1145.293	0.030899649	0.050247	419.985	0.049025	441.0879
176	69.6	0.0480	-0.0400	0.0000	0.0080	0.5520	-0.0800	0.000102073	419.985	0.000704	1145.293	0.031181372	0.050705	419.985	0.049461	441.2803
177	70	0.0480	-0.0480	0.0000	0.0000	0.5520	-0.0800	0.000102073	419.985	0.000704	1145.293	0.031463094	0.051163	419.985	0.049897	441.4727
178	70.4	0.0480	-0.0480	0.0000	0.0000	0.5440	-0.0720	9.1866E-05	377.9865	0.000694	1128.694	0.031742775	0.051618	377.9865	0.05033	397.4974
179	70.8	0.0480	-0.0400	0.0000	0.0080	0.5440	-0.0720	9.1866E-05	377.9865	0.000694	1128.694	0.032020415	0.052069	377.9865	0.050759	397.668
180	71.2	0.0480	-0.0400	0.0000	0.0080	0.5280	-0.0720	9.1866E-05	377.9865	0.000674	1095.497	0.032293971	0.052514	377.9865	0.051182	397.8362
181	71.6	0.0560	-0.0480	0.0080	0.0000	0.5280	-0.0720	9.1866E-05	377.9865	0.000674	1095.497	0.032563445	0.052952	377.9865	0.051598	398.0018
182	72	0.0560	-0.0480	0.0080	0.0000	0.5200	-0.0800	0.000102073	419.985	0.000663	1078.899	0.032830877	0.053387	419.985	0.052011	442.4069

Figure C.1 Derivations of equations (2.6) to (2.18) to obtain strain rate, true stress and true strain, $\sum\varepsilon = 1.82$ on x-axis, Continued

183	72.4	0.0480	-0.0480	0.0000	0.0000	0.5200	-0.0800	0.000102073	419.985	0.000663	1078.899	0.033096268	0.053819	419.985	0.052421	442.5881
184	72.8	0.0480	-0.0480	0.0000	0.0000	0.4960	-0.0800	0.000102073	419.985	0.000633	1029.104	0.033355534	0.05424	419.985	0.052821	442.7652
185	73.2	0.0480	-0.0400	0.0000	0.0080	0.4960	-0.0800	0.000102073	419.985	0.000633	1029.104	0.033608676	0.054652	419.985	0.053211	442.9381
186	73.6	0.0480	-0.0400	0.0000	0.0080	0.4720	-0.0640	8.16587E-05	335.988	0.000602	979.3083	0.033855694	0.055054	335.988	0.053592	354.4854
187	74	0.0480	-0.0480	0.0000	0.0000	0.4720	-0.0640	8.16587E-05	335.988	0.000602	979.3083	0.034096587	0.055445	335.988	0.053963	354.617
188	74.4	0.0480	-0.0480	0.0000	0.0000	0.4240	-0.0720	9.1866E-05	377.9865	0.000541	879.7177	0.034325231	0.055817	377.9865	0.054315	399.0847
189	74.8	0.0480	-0.0400	0.0000	0.0080	0.4240	-0.0720	9.1866E-05	377.9865	0.000541	879.7177	0.034541627	0.056169	377.9865	0.054648	399.2177
190	75.2	0.0480	-0.0400	0.0000	0.0080	0.3920	-0.0640	8.16587E-05	335.988	0.0005	813.3239	0.034749856	0.056508	335.988	0.054969	354.9739
191	75.6	0.0480	-0.0480	0.0000	0.0000	0.3920	-0.0640	8.16587E-05	335.988	0.0005	813.3239	0.03494992	0.056833	335.988	0.055277	355.0833
192	76	0.0480	-0.0480	0.0000	0.0000	0.3600	-0.0720	9.1866E-05	377.9865	0.000459	746.9301	0.035141818	0.057145	377.9865	0.055572	399.5866
193	76.4	0.0480	-0.0400	0.0000	0.0080	0.3600	-0.0720	9.1866E-05	377.9865	0.000459	746.9301	0.03532555	0.057444	377.9865	0.055855	399.6995
194	76.8	0.0480	-0.0400	0.0000	0.0080	0.3280	-0.0640	8.16587E-05	335.988	0.000419	680.5363	0.035501116	0.057729	335.988	0.056125	355.3844
195	77.2	0.0480	-0.0400	0.0000	0.0080	0.3280	-0.0640	8.16587E-05	335.988	0.000419	680.5363	0.035668517	0.058002	335.988	0.056382	355.4759
196	77.6	0.0480	-0.0400	0.0000	0.0080	0.2800	-0.0560	7.14514E-05	293.9895	0.000357	580.9456	0.035823668	0.058254	293.9895	0.05662	311.1156
197	78	0.0480	-0.0400	0.0000	0.0080	0.2800	-0.0560	7.14514E-05	293.9895	0.000357	580.9456	0.035966571	0.058486	293.9895	0.05684	311.1839
198	78.4	0.0480	-0.0400	0.0000	0.0080	0.2480	-0.0560	7.14514E-05	293.9895	0.000316	514.5518	0.036101308	0.058705	293.9895	0.057047	311.2483
199	78.8	0.0480	-0.0400	0.0000	0.0080	0.2480	-0.0560	7.14514E-05	293.9895	0.000316	514.5518	0.036227879	0.058911	293.9895	0.057241	311.3088
200	79.2	0.0480	-0.0400	0.0000	0.0080	0.2240	-0.0560	7.14514E-05	293.9895	0.000286	464.7565	0.036348325	0.059107	293.9895	0.057426	311.3664
201	79.6	0.0480	-0.0400	0.0000	0.0080	0.2240	-0.0560	7.14514E-05	293.9895	0.000286	464.7565	0.036462648	0.059293	293.9895	0.057602	311.421
202	80	0.0480	-0.0400	0.0000	0.0080	0.2000	-0.0560	7.14514E-05	293.9895	0.000255	414.9612	0.036570845	0.059469	293.9895	0.057768	311.4728
203	80.4	0.0480	-0.0480	0.0000	0.0000	0.2000	-0.0560	7.14514E-05	293.9895	0.000255	414.9612	0.036672919	0.059635	293.9895	0.057924	311.5216
204	80.8	0.0480	-0.0480	0.0000	0.0000	0.2000	-0.0480	6.1244E-05	251.991	0.000255	414.9612	0.036774992	0.059801	251.991	0.058081	267.0603
205	81.2	0.0480	-0.0400	0.0000	0.0080	0.2000	-0.0480	6.1244E-05	251.991	0.000255	414.9612	0.036877065	0.059967	251.991	0.058238	267.1021
206	81.6	0.0480	-0.0400	0.0000	0.0080	0.1840	-0.0480	6.1244E-05	251.991	0.000235	381.7643	0.036975056	0.060126	251.991	0.058388	267.1423
207	82	0.0480	-0.0400	0.0000	0.0080	0.1840	-0.0480	6.1244E-05	251.991	0.000235	381.7643	0.037068963	0.060279	251.991	0.058532	267.1808
208	82.4	0.0480	-0.0400	0.0000	0.0080	0.1760	-0.0560	7.14514E-05	293.9895	0.000225	365.1658	0.037160829	0.060428	293.9895	0.058673	311.7548
209	82.8	0.0480	-0.0400	0.0000	0.0080	0.1760	-0.0560	7.14514E-05	293.9895	0.000225	365.1658	0.037250654	0.060574	293.9895	0.058811	311.7977
210	83.2	0.0480	-0.0400	0.0000	0.0080	0.1600	-0.0560	7.14514E-05	293.9895	0.000204	331.9689	0.037336396	0.060714	293.9895	0.058942	311.8387
211	83.6	0.0480	-0.0400	0.0000	0.0080	0.1600	-0.0560	7.14514E-05	293.9895	0.000204	331.9689	0.037418054	0.060847	293.9895	0.059067	311.8778
212	84	0.0480	-0.0400	0.0000	0.0080	0.1440	-0.0480	6.1244E-05	251.991	0.000184	298.772	0.03749563	0.060973	251.991	0.059186	267.3556
213	84.4	0.0480	-0.0400	0.0000	0.0080	0.1440	-0.0480	6.1244E-05	251.991	0.000184	298.772	0.037569123	0.061092	251.991	0.059299	267.3857
214	84.8	0.0480	-0.0400	0.0000	0.0080	0.1280	-0.0480	6.1244E-05	251.991	0.000163	265.5751	0.037638533	0.061205	251.991	0.059405	267.4142
215	85.2	0.0480	-0.0400	0.0000	0.0080	0.1280	-0.0480	6.1244E-05	251.991	0.000163	265.5751	0.03770386	0.061311	251.991	0.059505	267.4409
216	85.6	0.0480	-0.0400	0.0000	0.0080	0.1120	-0.0480	6.1244E-05	251.991	0.000143	232.3782	0.037765104	0.061411	251.991	0.059599	267.466
217	86	0.0480	-0.0400	0.0000	0.0080	0.1120	-0.0480	6.1244E-05	251.991	0.000143	232.3782	0.037822265	0.061504	251.991	0.059687	267.4894
218	86.4	0.0480	-0.0400	0.0000	0.0080	0.1040	-0.0480	6.1244E-05	251.991	0.000133	215.7798	0.037877384	0.061594	251.991	0.059771	267.512
219	86.8	0.0480	-0.0480	0.0000	0.0000	0.1040	-0.0480	6.1244E-05	251.991	0.000133	215.7798	0.037930463	0.06168	251.991	0.059852	267.5338
220	87.2	0.0480	-0.0480	0.0000	0.0000	0.0960	-0.0400	5.10367E-05	209.9925	0.000122	199.1814	0.037981499	0.061763	209.9925	0.059931	222.9622
221	87.6	0.0480	-0.0400	0.0000	0.0080	0.0960	-0.0400	5.10367E-05	209.9925	0.000122	199.1814	0.038030494	0.061842	209.9925	0.060006	222.979
222	88	0.0480	-0.0400	0.0000	0.0080	0.0960	-0.0400	5.10367E-05	209.9925	0.000122	199.1814	0.03807949	0.061922	209.9925	0.060081	222.9957
223	88.4	0.0480	-0.0400	0.0000	0.0080	0.0960	-0.0400	5.10367E-05	209.9925	0.000122	199.1814	0.038128485	0.062002	209.9925	0.060156	223.0124
224	88.8	0.0480	-0.0400	0.0000	0.0080	0.0800	-0.0400	5.10367E-05	209.9925	0.000102	165.9845	0.038173397	0.062075	209.9925	0.060224	223.0278
225	89.2	0.0480	-0.0480	0.0000	0.0000	0.0800	-0.0400	5.10367E-05	209.9925	0.000102	165.9845	0.038214226	0.062141	209.9925	0.060287	223.0417
226	89.6	0.0480	-0.0480	0.0000	0.0000	0.0800	-0.0400	5.10367E-05	209.9925	0.000102	165.9845	0.038255056	0.062208	209.9925	0.060349	223.0557
227	90	0.0480	-0.0400	0.0000	0.0080	0.0800	-0.0400	5.10367E-05	209.9925	0.000102	165.9845	0.038295885	0.062274	209.9925	0.060412	223.0696

Figure C.1 Derivations of equations (2.6) to (2.18) to obtain strain rate, true stress and true strain, $\sum\varepsilon = 1.82$ on x-axis, Continued

228	90.4	0.0480	-0.0400	0.0000	0.0080	0.0640	-0.0320	4.08293E-05	167.994	8.17E-05	132.7876	0.038332632	0.062334	167.994	0.060468	178.4657
229	90.8	0.0480	-0.0400	0.0000	0.0080	0.0640	-0.0320	4.08293E-05	167.994	8.17E-05	132.7876	0.038365295	0.062387	167.994	0.060518	178.4746
230	91.2	0.0480	-0.0400	0.0000	0.0080	0.0640	-0.0400	5.10367E-05	209.9925	8.17E-05	132.7876	0.038397959	0.06244	209.9925	0.060568	223.1045
231	91.6	0.0480	-0.0400	0.0000	0.0080	0.0640	-0.0400	5.10367E-05	209.9925	8.17E-05	132.7876	0.038430622	0.062493	209.9925	0.060618	223.1156
232	92	0.0480	-0.0400	0.0000	0.0080	0.0480	-0.0400	5.10367E-05	209.9925	6.12E-05	99.59068	0.038459203	0.06254	209.9925	0.060662	223.1254
233	92.4	0.0480	-0.0400	0.0000	0.0080	0.0480	-0.0400	5.10367E-05	209.9925	6.12E-05	99.59068	0.0384837	0.062579	209.9925	0.060699	223.1337
234	92.8	0.0480	-0.0400	0.0000	0.0080	0.0400	-0.0320	4.08293E-05	167.994	5.1E-05	82.99223	0.038506156	0.062616	167.994	0.060734	178.5131
235	93.2	0.0480	-0.0400	0.0000	0.0080	0.0400	-0.0320	4.08293E-05	167.994	5.1E-05	82.99223	0.038526571	0.062649	167.994	0.060765	178.5187
236	93.6	0.0480	-0.0400	0.0000	0.0080	0.0480	-0.0320	4.08293E-05	167.994	6.12E-05	99.59068	0.038549027	0.062686	167.994	0.060799	178.5248
237	94	0.0480	-0.0480	0.0000	0.0000	0.0480	-0.0320	4.08293E-05	167.994	6.12E-05	99.59068	0.038573525	0.062726	167.994	0.060837	178.5315
238	94.4	0.0480	-0.0480	0.0000	0.0000	0.0480	-0.0320	4.08293E-05	167.994	6.12E-05	99.59068	0.038598022	0.062765	167.994	0.060874	178.5382
239	94.8	0.0480	-0.0480	0.0000	0.0000	0.0480	-0.0320	4.08293E-05	167.994	6.12E-05	99.59068	0.03862252	0.062805	167.994	0.060912	178.5449
240	95.2	0.0480	-0.0480	0.0000	0.0000	0.0480	-0.0320	4.08293E-05	167.994	6.12E-05	99.59068	0.038647018	0.062845	167.994	0.060949	178.5516
241	95.6	0.0480	-0.0480	0.0000	0.0000	0.0480	-0.0320	4.08293E-05	167.994	6.12E-05	99.59068	0.038671515	0.062885	167.994	0.060987	178.5583
242	96	0.0480	-0.0480	0.0000	0.0000	0.0480	-0.0320	4.08293E-05	167.994	6.12E-05	99.59068	0.038696013	0.062925	167.994	0.061024	178.565
243	96.4	0.0480	-0.0400	0.0000	0.0080	0.0480	-0.0320	4.08293E-05	167.994	6.12E-05	99.59068	0.03872051	0.062965	167.994	0.061062	178.5717
244	96.8	0.0480	-0.0400	0.0000	0.0080	0.0400	-0.0320	4.08293E-05	167.994	5.1E-05	82.99223	0.038742967	0.063001	167.994	0.061096	178.5778
245	97.2	0.0480	-0.0480	0.0000	0.0000	0.0400	-0.0320	4.08293E-05	167.994	5.1E-05	82.99223	0.038763381	0.063034	167.994	0.061127	178.5834
246	97.6	0.0480	-0.0480	0.0000	0.0000	0.0400	-0.0320	4.08293E-05	167.994	5.1E-05	82.99223	0.038783796	0.063067	167.994	0.061159	178.589
247	98	0.0480	-0.0400	0.0000	0.0080	0.0400	-0.0320	4.08293E-05	167.994	5.1E-05	82.99223	0.038804211	0.063101	167.994	0.06119	178.5945
248	98.4	0.0480	-0.0400	0.0000	0.0080	0.0400	-0.0320	4.08293E-05	167.994	5.1E-05	82.99223	0.038824625	0.063134	167.994	0.061221	178.6001
249	98.8	0.0480	-0.0400	0.0000	0.0080	0.0400	-0.0320	4.08293E-05	167.994	5.1E-05	82.99223	0.03884504	0.063167	167.994	0.061252	178.6057
250	99.2	0.0480	-0.0400	0.0000	0.0080	0.0400	-0.0240	3.0622E-05	125.9955	5.1E-05	82.99223	0.038865455	0.0632	125.9955	0.061283	133.9585

Figure C.1 Derivations of equations (2.6) to (2.18) to obtain strain rate, true stress and true strain, $\sum\varepsilon = 1.82$ on x-axis, Continued

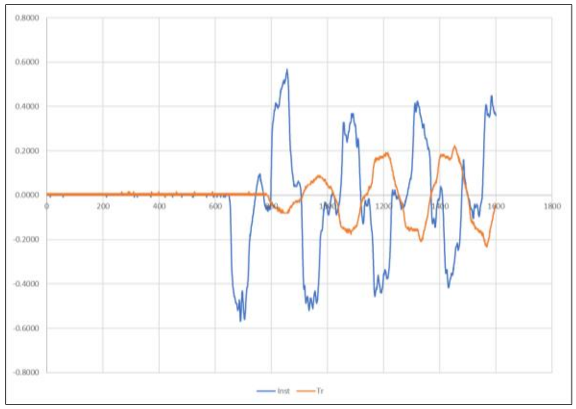

Figure C.2 Digital data from Hopkinson machine converted to numerical data showing the reflected and transmitted waves

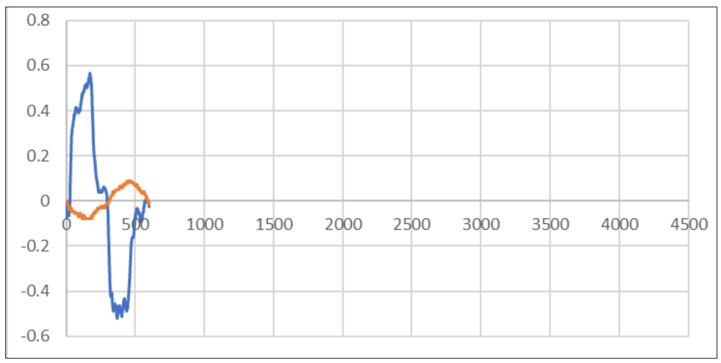

Figure C.3 Portion of the curves showed in C.2, showing one cycle of deformation

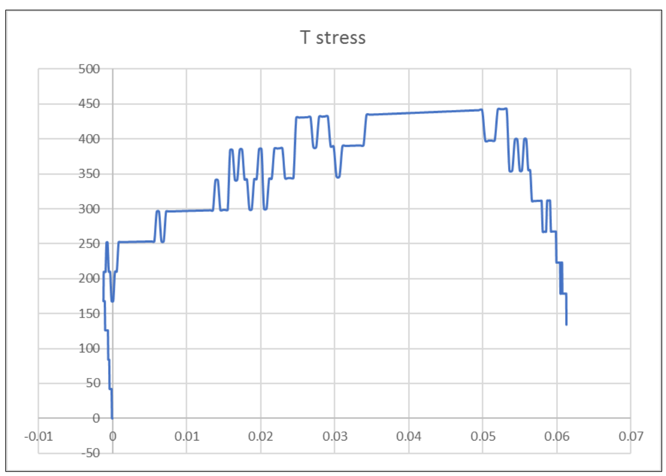

Figure C.4 Dynamic Compression Stress-strain before data smoothing

Appendix D

Grain Size Measurement

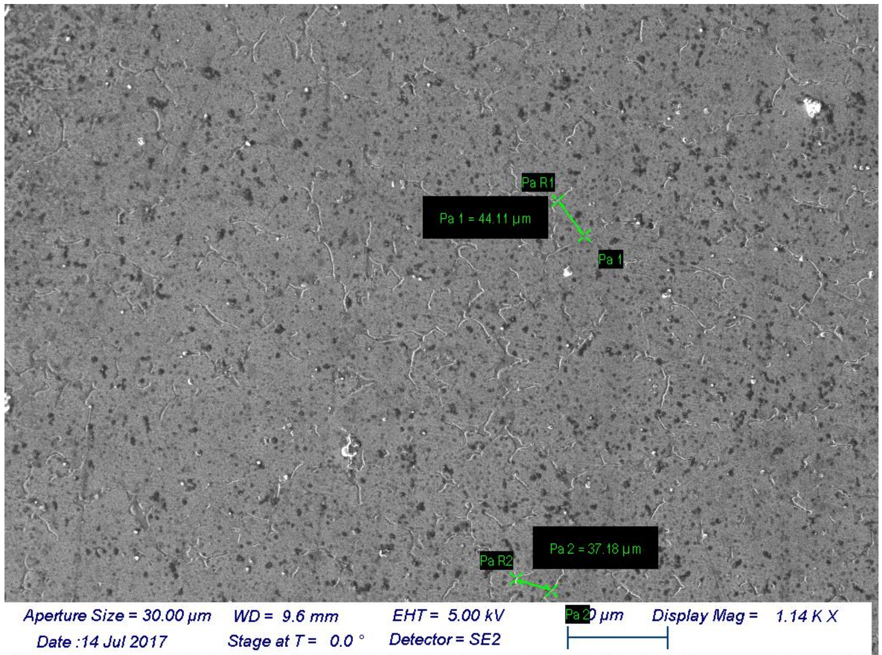

Figure D.1 SEM images of the grain size in magnitude of 1.14 kx of the initial state sample

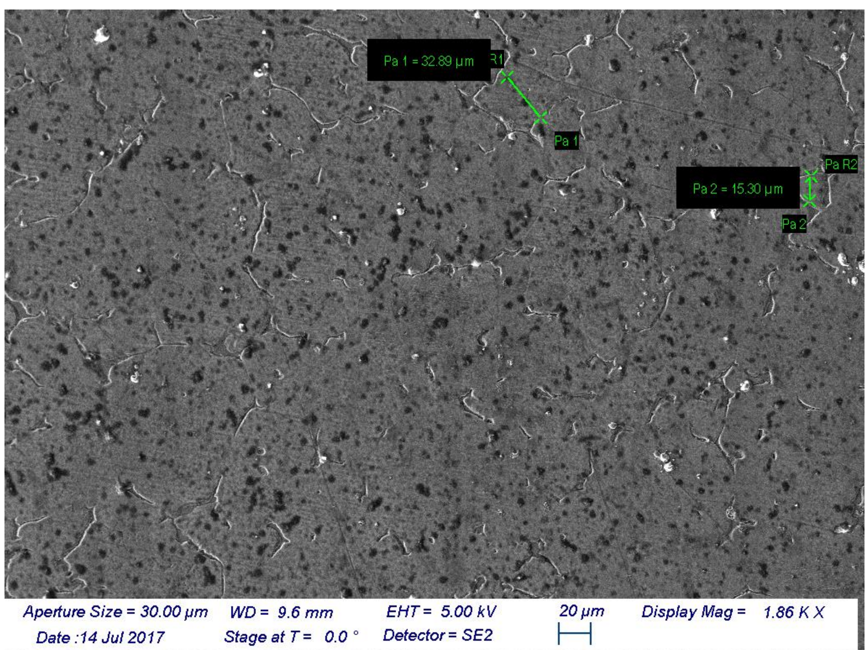

Figure D.2 SEM images of the grain size in magnitude of 1.86 kx of the initial state sample

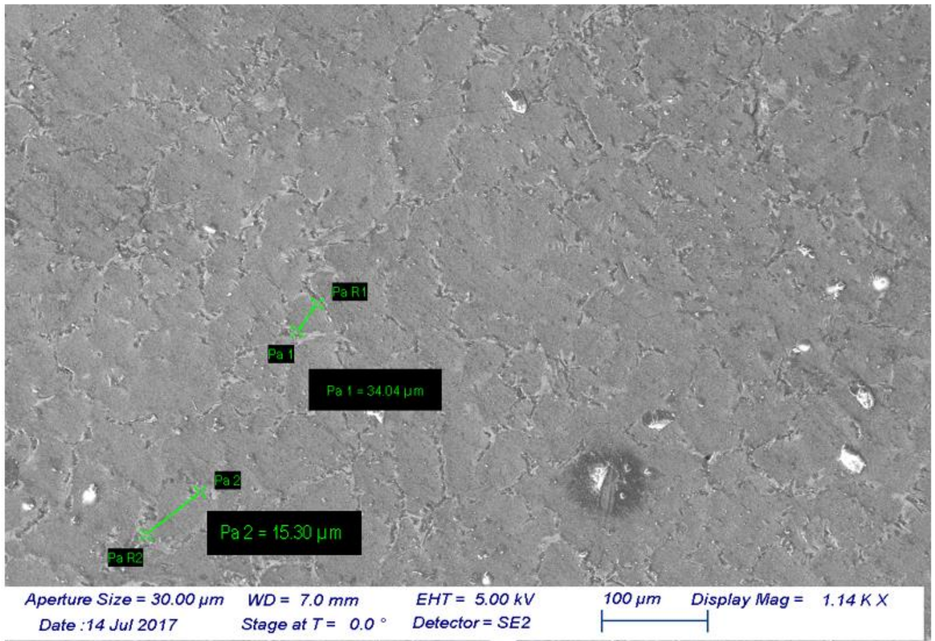

Figure D.3 SEM images of the grain size in magnitude of 1.14 kx of the MDF sample with $\sum\varepsilon = 2.77$

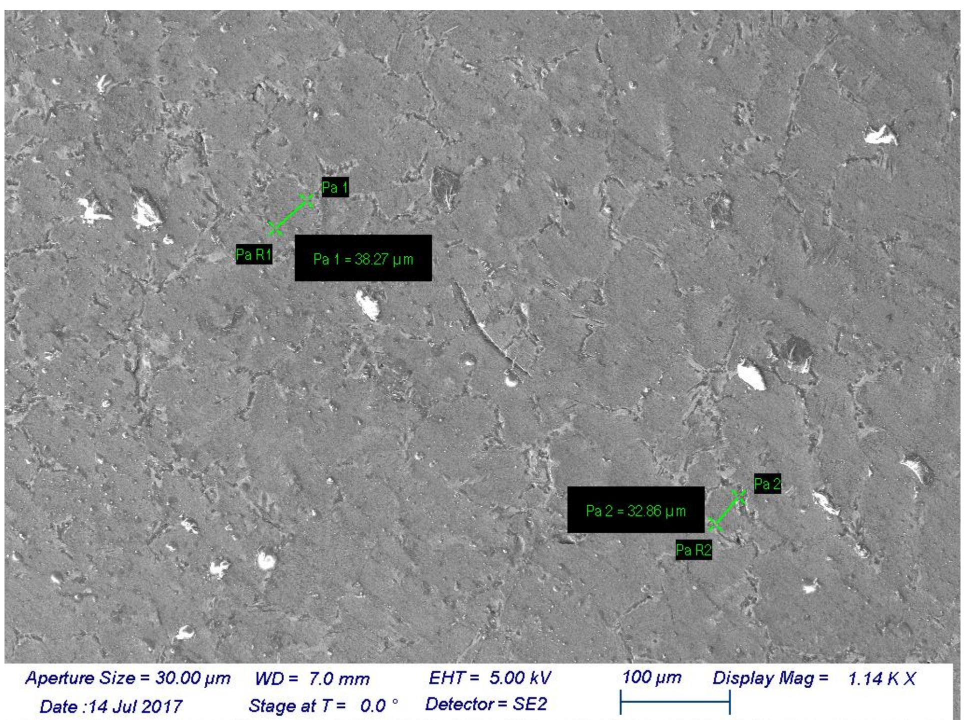

Figure D.4 SEM images of the grain size in magnitude of 1.14 kx of the MDF sample with $\sum\varepsilon = 2.77$

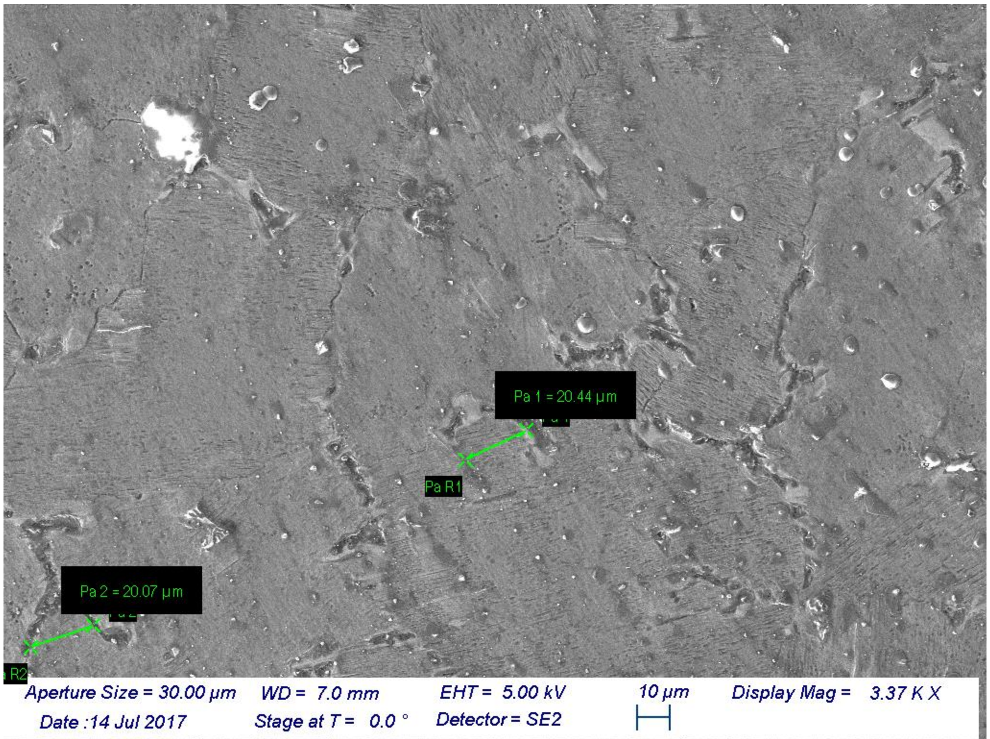

Figure D.5 SEM images of the grain size in magnitude of 1.14 kx of ECAP sample

Appendix E

SEM and Macro Images of Fracture Surfaces

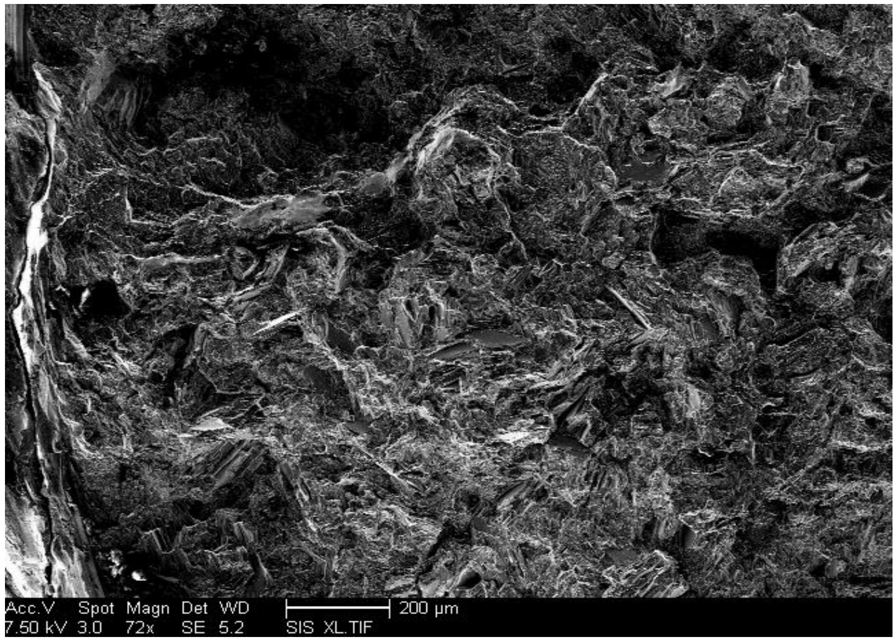

Figure E.1 SEM image of the fracture surface after tensile test of the initial state material

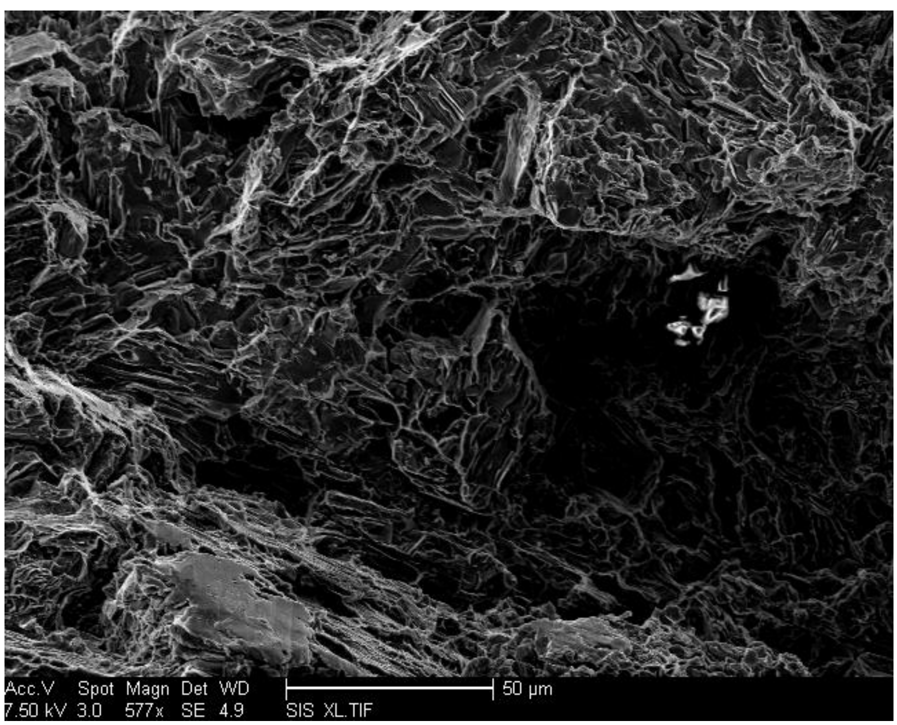

Figure E.2 SEM image of the fracture surface after tensile test of the initial state material

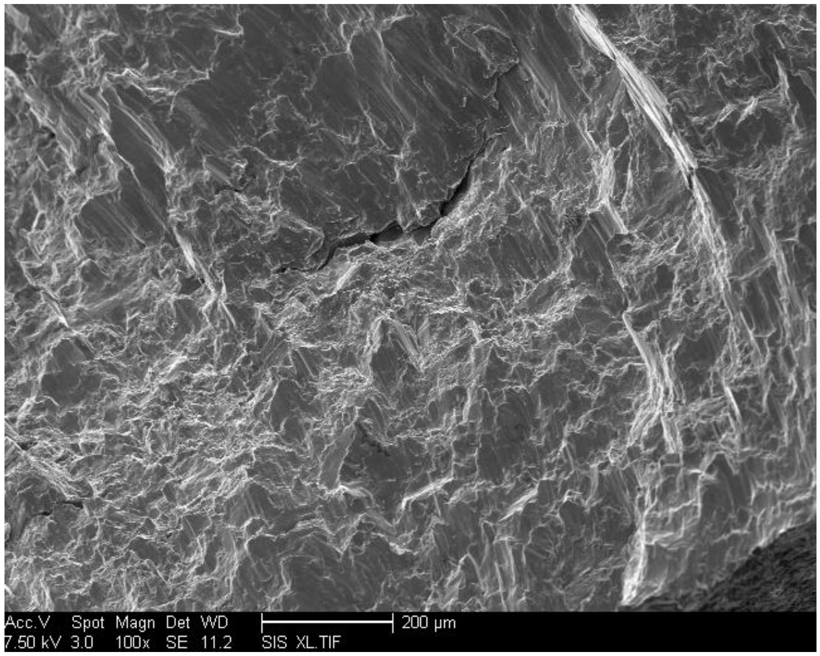

Figure E.3 SEM images of the fracture surface after quasi-static compression showing an internal crack that is probably caused during MDF, ∑ε = 2.15on y-axis

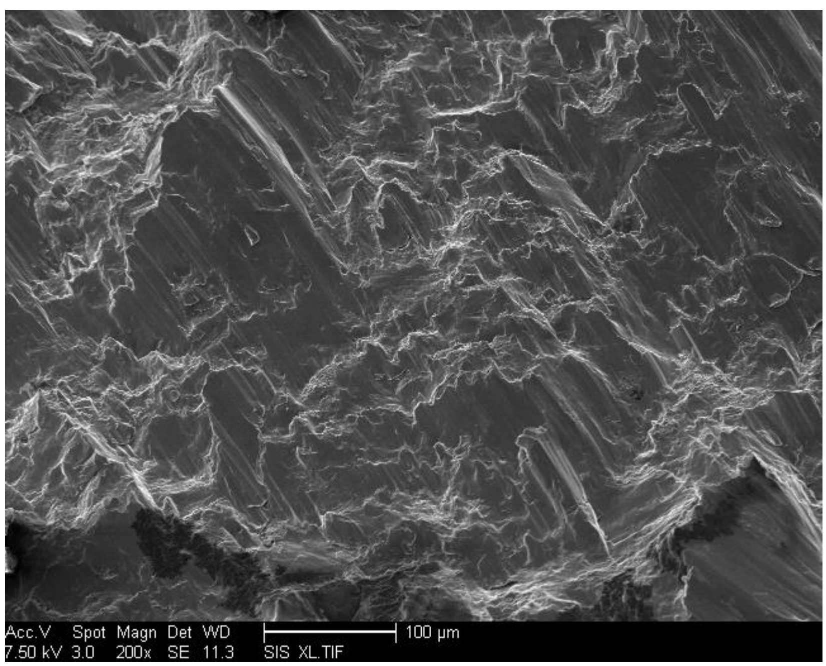

Figure E.4 SEM images of the fracture surface after quasi-static compression showing some ductile regions with predomint brittle regions, ∑ε = 2.15 on y-axis

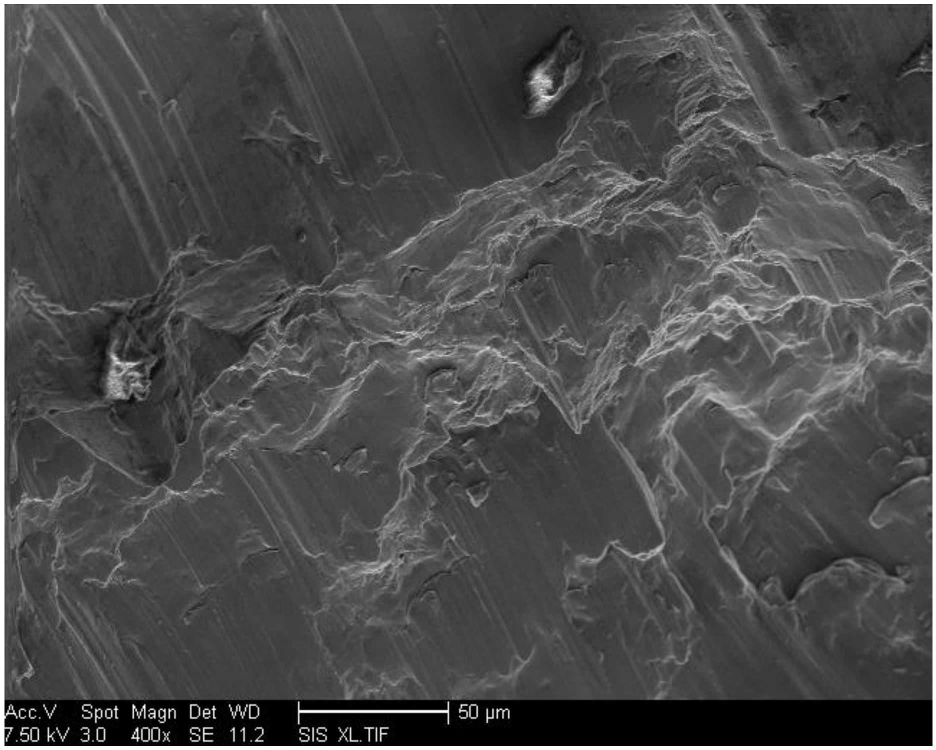

Figure E.5 SEM images of the fracture surface dynamic compression test ∑ε = 1.82 on z-axis

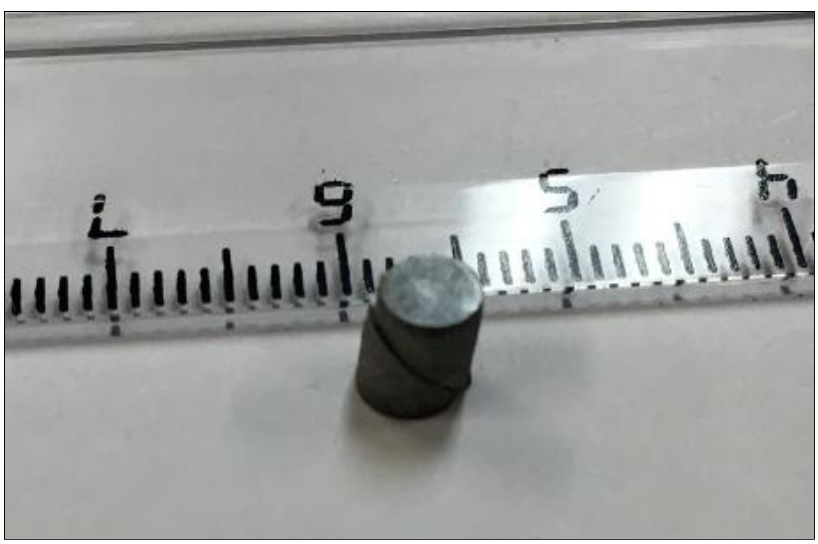

Figure E.6 Sample after quasi static compression test ∑ε = 2.15 on y-axis

Figure E.7 Fracture surface of quasi static compression test $\sum\varepsilon = 2.15$ on y-axis

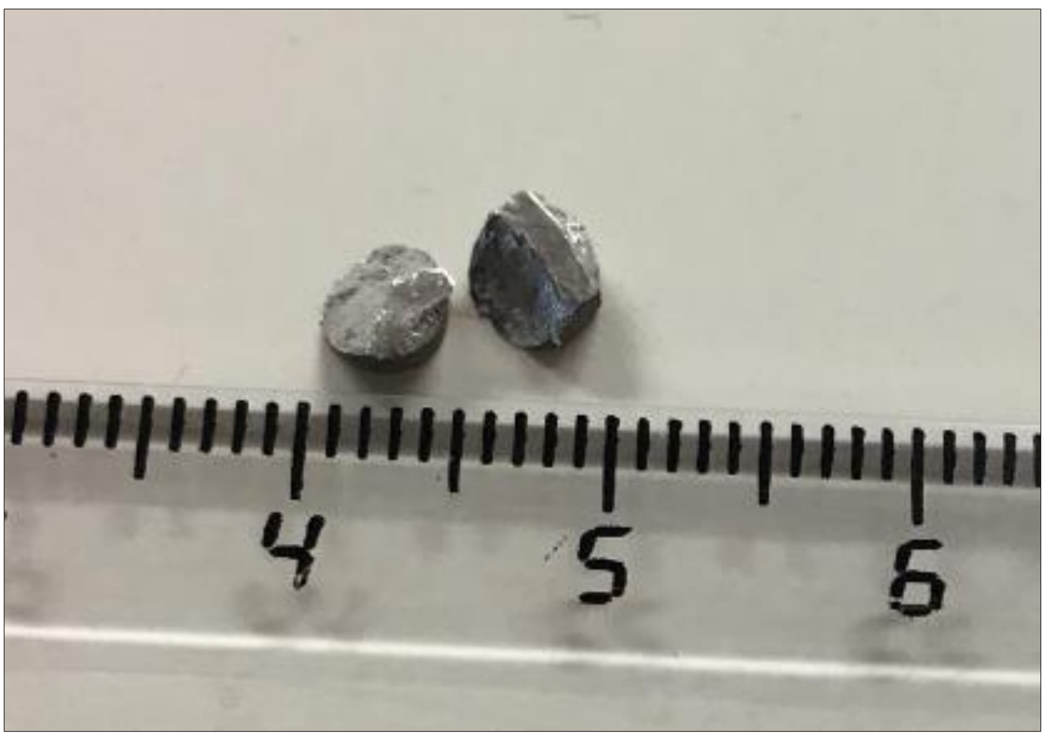

Figure E.8 Fracture surface of dynamic compression test $\sum\varepsilon = 1.82$ on y-axis

References

1. B. L. Mordike, T. Ebert, magnesium Properties - Applications – Potential, Material Science and Engineering A, 302 (2001) 37-45.

2. P. F Bernath, J. H Black, and J. W. Brault, The spectrum of magnesium hydride, The Astrophysical Journal, 298 (1985) 375-381.

3. R. Ash, The Top 10 of Everything 2006: The Ultimate Book of Lists, DK Publishing, (2005). Available at: http://plymouthlibrary.org/faqelements.htm. Accessed April 15, 2017.

4. G. J. Kipouros, D. R. Sadoway, A thermochemical analysis of the production of anhydrous $MgCl_2$, Journal of Light Metals, S1471 – 5317 (2001) 4-9.

5. C. E. Holloway, M. Melnik, magnesium compounds: classification and analysis of crystallographic and structural data, J. Organometallic Chemistry, 465 (1994) l-63.

6. International magnesium Association, magnesium Square Publishing, magnesium for lightweight applications, 2010. Available at http://magnesiumsquare.com/. Accessed April 15, 2017.

7. E. L. Dreizin, C. H. Berman, E.P. Vicenzi, Condensed-phase modifications in magnesium particle combustion in air. Scripta Materialia, 122 (2000) 30–42.

8. https://en.wikipedia.org/wiki/Dolomite

9. https://en.wikipedia.org/wiki/magnesium

10. http://www.elementsales.com/props.ht

11. The Element magnesium, The Periodic Table, 2011. Available at http://periodic-Table.org.uk/element-magnesium.htm. Accessed April 17, 2017.

12. http://www.myinterestingfacts.com/magnesium-facts/

13. S. Fleming, An Overview of magnesium based Alloys for Aerospace and Automotive Applications, (2012). Master's thesis. Available at http://ewp.rpi.edu/hartford/~ernesto/SPR.html. Accessed April 20, 201.

14. ASTM B80-15, Standard Specification for magnesium-Alloy Sand Castings, ASTM International, West Conshohocken, PA, 2015, Available at https://doi.org/10.1520/B0080-15.

15. E.P. Silva, L.F. Batista, B, Callegari, I. Feierabend, R.H Buzolin, R. S. Coelho, F. Warchomicka, G. C Requena, and H. Pinto, Casting in the semi-solid state of ZK60 magnesium alloy modified with rare earth addition, Advanced Materials Research 922 (2014) 694-699.

16. K. M. Asl, Improving the Properties of magnesium Alloys for High Temperature Applications – Design, Processing and Properties, Frank Czerwinski (Ed.), (2011), 265-280. Available at: http://intechopen.com/books/magnesium-alloys-design-processingand-properties/improving-the-properties-of-magnesium-alloys-for-high-temperature-applications

17. I. Polmear, D. StJonh, J. Nie, and M. Qian, Light alloys: metallurgy of light metals, Lon-don: Edward Arnold, 3rd ed. (1995).

18. W. Gan, Texture and Microstructure Development of the Silicon Containing magnesium Alloys after Equal Channel Angular Pressing, (2008), Doctoral dissertation. Available at: http://citeseerx.ist.psu.edu/index

19. S. Iikubo, K. Matsuda, and H. Ohtani, Phase stability of long-period stacking structures in Mg-Y-Zn: A first-principles study, American Physical Society, 86 (2012) 054105.

20. http://www.hti.edu.eg/academic-files/Arabic/2329.pdf

21. J. Meija, T. B. Coplen, M. Berglund, W. A. Brand, P. De Bièvre, M. Gröning, N. E. Holden, J. Irrgeher, R. D. Loss, T. Walczyk, and T. Prohaska, Atomic weights of the elements 2013 (IUPAC Technical Report), Pure Appl. Chem., 88(3) (2016) 265–291.

22. https://en.wikipedia.org/wiki/magnesium

23. http://www.knowledgedoor.com/2/elements_handbook/magnesium.html

24. http://bilbo.chm.uri.edu/PeriodicTable/magnesium.htm

25. https://en.wikipedia.org/wiki/Periodic_Table_(crystal_structure)

26. http://bilbo.chm.uri.edu/PeriodicTable/magnesium.htm

27. A. Matin, F. F. Saniee, H.R, Microstructure and mechanical properties of Mg/SiC and AZ80/SiC nano-composites fabricated through stir casting method, Materials Science and Engineering: A, 625 (2015) 81–88.

28. D. Hull, D. J. Bacon, Introduction to Dislocations, 4th ed., (2001) ISBN 0-7506-4681-0.

29. G. Caglioti, An approach to the plasticity of hcp metallic crystals in terms of their structure dynamics, Metallurgical Science and Technology, 16 (1998) 20-44.

30. J. W. Christian, S. Mahajan, Deformation twinning, Progress in Materials Science 39, (1995) 1–157.

31. L. Staroselsky, A. Anand, A constitutive model for hcp materials deforming by slip and twinning: application to magnesium alloy AZ31B, International Journal of Plasticity 19 (2003) 1843-1864.

32. P.G. Partridge. The crystallography and deformation modes of hexagonal close packed metals, Int. Metall. Rev., 12 (1969) 170-194.

33. G. S. Kim, Small Volume Investigation of Slip and Twinning in magnesium Single Crystals (2011), Doctoral dissertation.
Available at http://www.numodis.fr/download/2011-These_GyuSeok_KIM.pdf

34. E. Lilleodden, Microcompression study if Mg (0 0 0 1) single crystal, Scripta Materialia, 62 (2010) 532-535.

35. Q. Yu, L. Qi, K. Chen, R. K. Mishra, J. Li, and A. M. Minor, The nanostructured origin of deformation twinning, American Chemical Society, 12 (2012) 887-892.

36. Z. Zhang, H. Sheng, Z. Wang, B. Gludovatz, Z. Zhang, E. P. George, Q. Yu, S. X. Mao, and R. O. Ritchie, Dislocation Mechanisms and 3D twin architectures generate exceptional strength-ductility-toughness combination in CrCoNi medium-entropy alloy, Nature Communications, 8 (2017) 14390.

37. G. Chin, W. Mammel, Competition among basal, prism, and pyramidal slip modes in hcp metals. Metallurgical Transactions Metallurgical and Materials Transactions B, 1 (1970) 357–361.

38. L. Long, M. Zhang, Y. Li, J. Zhao, L. Qin, Y. Lai, Corrosion and biocompatibility improvement of magnesium-based alloys as bone implant materials: a re-view, Regenerative Biomaterials, 4 (2017) 129-137.

39. J. Reifenrath, N. Angrisani, N. Erdmann, A. Lucas, H. Waizy, J. M. Seitz, A. Bondarenko, A. M. Lindenberg, Degrading magnesium screws ZEK100: biome-chanical testing, degradation analysis and soft-tissue biocompatibility in a rabbit model, Biomedical Materials, 8 (2013) 045012.

40. R. Valiev, Nanostructuring of metals by severe plastic deformation for advanced properties, Nature Materials, 3 (2004) 511-516.

41. Magnesium Elektron WE43 Alloy (UNS M18430), Available at http://www.azom.com/article.aspx?ArticleID=9279. Accessed July 19, 2016.

42. P. Zartner, R. Cesnjevar, H. Singer, M. Weyand, First successful implantation of a biodegradable metal stent into the left pulmonary artery of a preterm baby Catheter-ization and Cardiovascular Interventions, 66 (2005) 590-594.

43. R. J. Hussey, J. Wilson, “Light Alloys: Directory and Databook”, ISBN 978-0-412-80410-6 (2013) 302-304.

44. ASTM B954-15, Standard Test Method for Analysis of magnesium and magnesium Alloys by Atomic Emission Spectrometry, ASTM International, West Conshohock-en, PA, (2015).

45. R. J. Gest, A. R. Troiano, Stress Corrosion and Hydrogen Embrittlement in an Aluminum Alloy, Corrosion Journal, 30 (1974) 274-279.

46. http://www.afsinc.org/files/images/magnes.pdf

47. M. Ascencio, M. Pekguleryuz, S. Omanovic, An investigation of the corrosion mechanisms of WE43 Mg alloy in a modified simulated body fluid solution:the effect of electrolyte renewal, Corros. Sci. 91 (2015) 297–310.

48. D. X. Liu, X. Pang, D. L. Li, C. G. Guo, J Wongsa-Ngam, T. G. Langdon, and M.A Meyers, Microstructural Evolution and Properties of a Hot Extruded and HPT-Processed Resorbable magnesium WE43 Alloy, Adv. Eng. Mater., 19 (2017) 1600698.

49. F. Witte, V. Kaese, H. Haferkamp, E. Switzer, A. Meyer-Lindenberg, C.J. Wirth, H. Windhagen, In vivo corrosion of four magnesium alloys and the associated bone response, Biomaterials 26 (2005) 3557–3563.

50. R. A. Causey, D. F. Cowgill, and R. H. Nilson, Review of the Oxidation Rate of Zirconium Alloys, Sandia National Laboratories, 22161 (2005) 2005-6006.

51. Magnesium Alloys, Smiths Metal Centers Limited, (2005), Available at https://www.smithmetal.com/magnesium-alloys.htm. Accessed August 2016.

52. L. Wong, “magnesium is called the Metal of the Future for a Reason”, CD International Enterprises, Inc. Blog. Available at https://cdiichinadirect.wordpress.com/2012/04/04/magnesium-is-called-the-etal-of-the-future-for-a-reason-lillian-wong/. Accessed July 2016

53. R. O. Hussein, D. O. Northwood, Improving performance of magnesium Alloys for automotive applications, Wit Transactions on The Built Environment, 137 (2014) 531-544.

54. M. Dhahri, J. E. Masse, J. F. Mathieu, G. Barreau, M. Auteric, Laser welding of AZ91 and WE43 magnesium alloys for automotive and aerospace industries, Adv Eng Mater 2001;7:504-7.

55. N. Afrin, D.L. Chen, X. Cao, M. Jahazi, Microstructure and tensile properties of friction stir welded AZ31B magnesium alloy, Materials Science and Engineering A, 472 (2008) 179.

56. M. A. Meyers, P. Chen, Biological Materials Science: Biological Materials, Bioin-spired Materials, and Biomaterials, (2014), Cambridge: Cambridge University Press.

57. S. W. Wise, Microarchitecture and deposition of gastropod nacre, Science 167 (1970) 1486-1488.

58. H. Wang, Y. Estrin, and Z. Zuberova, Bio-corrosion of a magnesium alloy with different processing histories, Mater. Lett. 62 (2008) 2476–2479.

59. F. Wiitte, V. Kaese, H. Haferkamp, E. Switzer, A. Meyer–Lindenberg, C. J. Wirth, and H. Windhagen, In vivo corrosion of four magnesium alloys and the associated bone response, Biomaterials, 280 (2005) 15-25.

60. K. V. Kutniy, I.I Papirov, M. A. Tikhonovsky, A. I. Pikalov, S. V. Sivtzov, L. A. Pirozhenko, V. S. Shokurov, and V. A. Shkuropatenko, Influence of grain size on mechanical and corrosion properties of magnesium alloy for medical implants, Mat.-wiss.u. Werkstofftech, 40 (2009) 242–246.

61. http://www.ancient-minerals.com/magnesium-sources/dietary/

62. http://www.medicalnewstoday.com/articles/286839.php

63. http://www.webmd.com/vitamins-supplements/ingredientmono-998-magnesium.aspx?activeingredientid=998

64. https://draxe.com/magnesium-deficient-top-10-magnesium-rich-foods-must-eating/

65. https://www.healthaliciousness.com/articles/foods-high-in-magnesium.php

66. Q. Wei, S. Cheng, K. T. Ramesh, E. Ma, Effect of monocrystalline and ultrafine grain sizes on the strain rate sensitivity and activation volume: fcc versus bcc metals, Materials Science and Engineering, A.381 (2008) 71–79.

67. Z. Horita, Nanomaterials by severe plastic deformation, Proceedings of NanoSPD3, Fukuoka, (2005).

68. T.G. Langdon, M. Furukawa, M. Nemoto, and Z. Horita, Using equal-channel angular pressing for refining grain size, JOM, 52 (2000) 30.

69. Y. Yamashi, Z. Horita, T. G. Langdon, Improving the mechanical properties of magnesium and a magnesium alloy through severe plastic deformation, Materials Science and Engineering A. 300 (2001) 142–147.

70. K. Nakashima, Z. Horita, M. Nemoto, T.G. Langdon, Development of a multi-pass facility for equal-channel angular pressing to high strains, Mater. Sci. Eng. A, 281 (2000) 82.

71. P. C. Sharath, K. R. Udupa ,and G. V. P. Kumar, Effect of Multi Directional Forging on the Microstructure and Mechanical Properties of Zn-24 wt% Al-2 wt% Cu Alloy, Trans Indian Inst. Met. 70 (2017) 89-96.

72. E. O. Hall, The Deformation and Ageing of Mild Steel: III. Discussion of Results, Proc. Phys. Soc. Lond. B 64, (1951) 747–753.

73. M. A. Meyers, K.K. Chawla, Mechanical Behavior of Materials, Cambridge University Press, (2009).

74. N. J. Petch, The Cleavage Strength of Polycrystals, J. Iron Steel Inst 174 (1953) 25-28.

75. V.M. Segal, Equal channel angular extrusion: from macromechanics to structure formation, Materials Science and Engineering: A, (1999) 322–333.

76. R.E. Reed-Hill, W.D. Robertson. The crystallographic characteristic fracture in magnesium single crystal, Acta Metall. 5 (1957) 717-728.

77. L. Olejnik, W. Chrominski, A. Rosochowski, M. Lipinska, M. Lewandowska, Incremental ECAP as a novel tool for producing ultrafine grained aluminum plates, IOP Conf. Ser. Mater. Sci. Eng. 63 (2014) 012004.

78. M. Furukawa, Y. Iwahashi, Z. Horita, M. Nemoto, T.G. Langdon, The shearing characteristics associated with equal-channel angular pressing, Mater Sci Eng A. 257 (1998) 328-332.

79. Y. Iwahashi, J.T. Wang, Z. Horita, M. Nemoto, T.G. Langdon. Principle of equal channel angular pressing for the processing of ultra-fine grained materials, Scripta Mater. 35 (1996) 143-146.

80. Y. Iwahashi, Z. Horita, M. Nemoto and T. G. Langdon, An investigation of micro-structural evolution during equal-channel angular pressing, Acta materialia 45 (1997) 4733–4741.

81. M. Richert, Q. Liu, N. Hansen, Microstructural evolution over a large strain range in aluminum deformed by cyclic-extrusion–compression, Mater. Sci. & Eng. A260 (1999) 275-283.

82. A. Mishra, B.K. Kad , F. Gregori, M.A. Meyers, Microstructural evolution in copper subjected to severe plastic deformation: Experiments and analysis, Acta Materialia, 55 (2007) 13-28.

83. P.B. Berbon, M. Furukawa, Z. Horita, M. Nemoto, T.G. Langdon, An Examination of the Deformation Process in Equal-Channel Angular Pressing, Mat. Res. Soc. Symp. 601 (2000) 347-352.

84. M. Furukawa, Z. Horita, M. Nemoto, T.G. Langdon. Review-Processing of metals by equal-channel angular pressing, J. Mater. Sci. 36 (2001) 2835-2843.

85. R. B. Figueiredo and T. B. Langdon, Principles of grain refinement and superplastic flow in magnesium alloys processed by ECAP, Materials Science and Engineering A, 501 (2009) 105-114.

86. R.Z. Valiev, R.K. Islamgaliev, I.V. Alexandrov, Bulk nanostructured materials from severe plastic deformation, Prog. Mater. Sci. 45 (2000) 103–189.

87. X. Li, T. Jin, M. Lu, J. Zhan, Microstructure and Mechanical Properties of Ultrafine Lath-Shaped Low Carbon Steel, J. of Materi. Eng. and Perform. 21 (2012) 1496-1499.

88. T. Sakai, A. Belyakov, R. Kaibyshev, H. Miura, J. Jonas, Dynamic and post-dynamic recrystallization under hot, cold and severe plastic deformation conditions, J, Prog. Mater. Sci. 60 (2014) 130-206.

89. P. C. Sharath, K. R. Udupa, G. V. P. Kumar, Effect of Multi Directional Forging on the Microstructure and Mechanical Properties of Zn-24 wt% Al-2 wt% Cu Alloy, Transactions of the Indian Institute of Metals, (2016).

90. J. Xing, X. Yang, H. Miura, T. Sakai, Superplasticity of Fine-Grained magnesium Alloy AZ31 Processed by Multi-Directional Forging, Materials Transactions, 48 (2007) 1406-1411.

91. A. Takara, Y. Nishikawa, H. Watanabe, H. Somekawa, T. Mukai, K. Higashi, New Forming Process of Three-Dimensionally Shaped magnesium Parts Utilizing High-Strain-Rate Superplasticity, Materials Transactions, 45 (2004) 2531-253.

92. O. Sitdikov, T. Sakai, A. Goloborodko, H. Miura, R. Kaibyshev, Effect of Pass Strain on Grain Refinement in 7475 Al Alloy during Hot Multidirectional Forging, Materials Transactions, 45 (2004) 2232-2238.

93. Y. Takigaw, M. Honda, T. Uesugi, K. Higashi, Effect of Initial Grain Size on Dynamically Recrystallized Grain Size in AZ31 magnesium Alloy, Materials Transactions, 49 (2008) 1979-1982.

94. J. Xing, H. Soda, X. Yang, H. Miura, T. Sakai, Ultra-fine grain development in an AZ31 magnesium alloy during multi-directional forging under decreasing temperature conditions, Materials Transactions, 46 (2005) 1646–1650.

95. J.H. Sung, J.H. Kim, R.H. Wagoner, A plastic constitutive Equation incorporating strain, strain-rate, and temperature, Int. J. Plast. 26 (2010) 1746–1771.

96. B. Hopkinson, A Method of Measuring the Pressure Produced in the Detonation of High Explosives or by the Impact of Bullets, Philos. Trans. R. Soc. (London) A, 213 (1914) 437-456.

97. A. B. Shemirani, R. Naghdabadi, M. Ashrafi, Experimental and numerical study on choosing proper pulse shapers for testing concrete specimens by split Hopkinson pressure bar apparatus, Constr. Build. Mater. 125 (2016) 326–336.

98. G. T. Gray, Classic Split Hopkinson Pressure Bar Technique, ASM V8 Mechanical Testing, (1999) 17-20.

99. A. Gilat and Y.H. Pao, High-Rate Decremental-Strain-Rate Test, Exp. Mech. 28 (1988) 322–325.

100. S. Nemat-Nasser, J. B. Isaacs, J. E. Starrett, Hopkinson Techniques for Dynamic Recovery Experiments, Mathematical and Physical Sciences, 435 (1991) 371-391.

101. M.A. Meyers, Dynamic Fracture, in Dynamic Behavior of Materials, John Wiley & Sons, Inc., Hoboken, NJ, USA, (1994).

102. G. V. Voort, Metallography of magnesium and its Alloys, Buehler, Inc. Tech Notes, Volume 4, Issue 2.

103. http://nano3.calit2.net/equipment/machine.php?eid=58

104. E.J. Pavlina and C.J. Va, Tyne Correlation of Yield Strength and Tensile Strength with Hardness for Steels, Journal of Materials Engineering and Performance, 17 (2008) 888-893.

105. https://en.wikipedia.org/wiki/Vickers_hardness_test

106. http://www.gordonengland.co.uk/hardness/vickers.htm

107. STM E92-17 Standard Test Methods for Vickers Hardness and Knoop Hardness of Metallic Materials, ASTM International, West Conshohocken, PA, (2017).

108. Y. Zhanga and B. Tian, Dynamic recrystallization model of the Cu–Cr–Zr–Ag alloy under hot deformation, Journal of Materials Research, 31 (2016) 1275-1285.

109. M. Liu, H. J. Roven, T. Ungar, L. Balogh, M. Y. Murashkin, R. Valiev, Grain refinement in nanostructured Al–Mg alloys subjected to high pressure torsion, Mater. Sci. Forum, 528 (2008) 584–58.